Numerical Modeling of Particle Breakage in Dry Impact Pulverizer

Numerical Modeling of Particle Breakage in Dry Impact Pulverizer

Hirohisa TAKEUCHI

February 2013

Doctoral Thesis at Osaka Prefecture University

Acknowledgements

First of all, I would like to express my sincere gratitude to my supervisor, Professor Satoru Watano of the Department of Chemical Engineering, Osaka Prefecture University, for his continuing guidance, encouragement and support in all phases of this work.

I am very grateful to Professor Motoaki Adachi and Professor Masashi Iwata of the Department of Chemical Engineering, Osaka Prefecture University, for their valuable discussions and useful advices.

I wish to appreciate Assistant Professor Hideya Nakamura for his encouragement and a lot of useful discussion during the preparation of the manuscript.

I received generous encouragement and fruitful advice from Associate Professor Tomohiro Iwasaki.

I would like to thank all the faculty members in the Department of Chemical Engineering, Osaka Prefecture University, for their encouragement and useful suggestions.

My deep gratitude goes to President Hidefumi Kanazawa and Mr. Naochika Asai of Fuji Paudal Co., Ltd. for their warm encouragement and support. I also appreciate Mr. Takanobu Tsuji of Fuji Paudal Co., Ltd. for his technical assistance.

My appreciations also extend to my former and present colleagues in the Process Systems Engineering Laboratory of the Department of Chemical Engineering, Osaka Prefecture University.

Finally, I would like to thank my parents Kyutarou and Takako Takeuchi, and my sister and brother for their continuous support and encouragement.

Contents

Acknowledgements

Chapter I Introduction 1

I-1 General introduction 3

I-2 Review of previous works 7

1. Single particle breakage 7
2. Modeling of grinding process 10
3. Control of grinding process 14

I-3 Scope of this thesis 15

References 17

Chapter II Numerical simulation of fluid and particle behavior in dry impact pulverizer 25

II-1 Numerical analysis of fluid and particle behavior in dry impact pulverizer 27

1. Introduction 27
2. Dry impact pulverizer 28
3. Numerical modeling 30
4. Experimental 42
5. Results and discussion 44
6. Conclusions 59

Nomenclature 59

References 62

II-2 Numerical simulation for equipment design in dry impact pulverizer 63

1. Introduction 63
2. Numerical analysis 64
3. Experimental 66
4. Results and discussion 68
5. Conclusions 78
Nomenclature 78
References 79

Chapter III Development of simulation method of particle breakage in dry impact pulverizer 81

1. Introduction 83
2. Particle breakage model 84
3. Numerical simulation 89
4. Experimental 94
5. Results and discussion 97
6. Conclusions 115
Nomenclature 115
References 117

Chapter IV Development of a novel particle size control system for dry impact pulverizer 119

1. Introduction 121
2. Experimental 122
3. Design of fuzzy controller 126
4. Results and discussion 130
5. Conclusions 136
Nomenclature 136
References 137

Chapter V Overall Conclusions 139

List of papers related to this thesis 145

Chapter I

Introduction

I-1. General introduction

A grinding process has been used to reduce size of particulate materials since the Stone Age. Even in recent years, the grinding process is still widely used in many industries in order to utilize many advantages such as increase in reactivity, improvement of solubility and mixing homogeneity of solid materials. There are many types of grinding process because various particle sizes of final ground product are required depending on the applications. In all types of the grinding process, it is important to control the particle size of intermediate and final ground products, because quality and performance of the final products are significantly affected by the particle size. For example, pre-treatment of ball milling for a fuel cell electrocatalyst leads to the improvement of electrocatalyst ability due to the generation of large active sites [111]. In pharmaceutical industries, particle size of active pharmaceutical ingredients and excipients should be maintained their sizes accurately in order to secure the appropriate dissolution rate and solubility [16, 66]. The controlled particle size of mineral ore is helpful in improving efficiency of the ore concentration process, which concentrates metals from the ground mineral ores [19]. In waste disposal industries, insufficient dissolution of noble metals occurs in the separation process if the particle size of ground printed board is not controlled [31].

In recent years, grinding processes have been used not only for size reduction, but also for synthesis of advanced materials by utilizing the mechanical forces generated in the grinding processes. For example, carbon nanotube and carbon onion are prepared by enormous mechanical force using a planetary ball mill [73, 93]. Functional composites are also made through the mechanical alloying method using the mechanical force in many types of ball mill [32, 92]. In addition, tumbling ball mills are utilized as the mechanochemical reaction field in order to achieve environmentally friendly synthesis approach [48, 108].

Therefore, it is necessary to understand the grinding process in detail in order to control particle size distribution of the ground products and mechanical forces in the advanced synthesis. However, it is very difficult to clarify the grinding phenomena such as fluid and particle motions, mechanical force acting on particles and walls, and overall particle breakage in the grinding process because the grinding phenomena are extremely

fast and complex.

Recently, the grinding phenomena in a grinding process are understood by a numerical simulation approach. Many researchers have analyzed the grinding process using the numerical simulation and many valuable findings have been obtained for understanding of the grinding process. However, there are huge drawbacks in the numerical simulation of the grinding process. One of the most serious drawbacks is that particles in the numerical simulation cannot breaks and splits into smaller particles, namely fragments. Therefore, particle breakage phenomena in the grinding process have not been analyzed by the numerical simulation approach yet. A particle breakage mechanism in the grinding process and temporal changes in particle size distribution of the ground products are not understood in detail.

The reason why the numerical simulation cannot treat the particle breakage is because it is very difficult to decide whether the particle is broken or not in the numerical simulation. So far, a lot of studies on single particle breakage have been reported. According to the studies, relationship between external force acting on the particle and strength of the particle is very important for the particle breakage. In addition, it is somewhat revealed that how the particle splits into fragments after the particle breakage. However, knowledge of the single particle breakage has not been applied to the numerical simulation of overall particle breakage in the grinding process. In order to overcome the big drawback in the numerical simulation of the grinding process, it is necessary to model a fundamental breakage of single particle and expand the single particle breakage to the numerical simulation of overall grinding phenomena in the grinding process. Therefore, development of a novel method which can simultaneously simulate the single particle breakages and overall grinding phenomena in the grinding process is strongly expected.

Among many types of grinding processes, a dry impact pulverizer which is showed Fig. 1.1.1 has been well used in many industries as offering many advantages such as substantial reduction in particle size and relatively short processing time. The dry impact pulverizer mainly consists of a high-speed rotating rotor with hammers and concavo-convex-shaped stator in the grinding chamber. The starting materials are fed into the grinding chamber through a hopper. The particles are accelerated by fluid flow

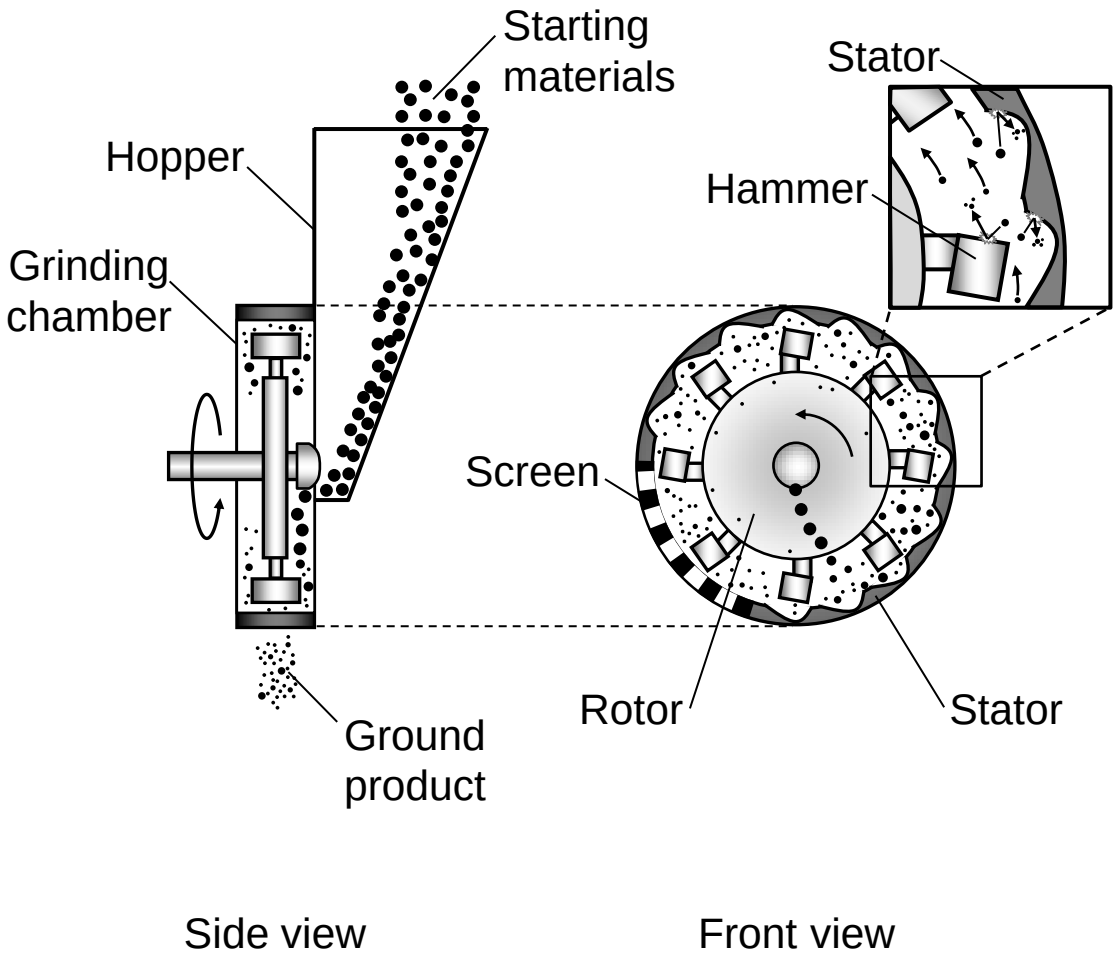

Fig. 1.1.1. Schematic diagram of dry impact pulverizer.

derived from high-speed rotation of the rotor and impact against walls of the static stator and the hammers. The impacted particles are broken and split into fragments. The fragments pass through a screen and are collected as the final ground product. However, control, optimization and design of the dry impact pulverizer are very difficult because there are complexities of fluid flow, particle behavior, and its breakage in the grinding chamber due to its fast motion through the complex geometries. In addition, the dynamic characteristics of the dry impact pulverizer vary depending on the characteristic of starting materials such as moisture content and electrostatic charge. Therefore, elucidation of the grinding mechanism and development of a practical system to ensure process controllability in the dry impact pulverizer are required.

This thesis is devoted to a numerical modeling of particle breakage in a dry impact pulverizer in order to understand both the fundamental particle breakage mechanism and the overall grinding mechanism in the dry impact pulverizer. A novel method which can simulate simultaneously single particle breakages and overall grinding phenomena in the dry impact pulverizer is proposed. This study is also dedicated to development of a practical system for automatic control of the ground product size in the dry impact pulverizer by using a fuzzy logic and on-line measurement technique.

I-2. Review of previous works

Grinding phenomena in the dry impact pulverizer are composed of enormous number of single particle breakages. First of all, fundamental studies on mechanism of single particle breakage by means of experimental and numerical methods are reviewed. Second, theoretical analysis of grinding phenomena using a population balance model and overall particle motion in many types of grinding processes using a numerical simulation method are reviewed. Then, numerical simulation methods coupled with a particle breakage model are reviewed. Finally, the studies on an automatic control system of grinding process for accurate size control of ground product are reviewed.

1. Single particle breakage

Numerous researchers have analyzed single particle breakage. A single particle is broken and splits into fragments when the particle receives an external force stronger than the particle strength. Therefore, the single particle breakage process can be generally described by particle strength, external force acting on the particle, and fragment size distribution after the particle breakage. The studies on the single particle breakage have been conducted by means of experimental and numerical approaches. The experimental approaches are reviewed in the first half of this section, followed by the review of the numerical approaches in the second half of this section.

The particle strength has been measured and analyzed experimentally by many researchers. The particle strength of brittle materials such as ceramics, glass, and alumina have been measured and described by Weibull distribution [24, 29, 49, 61, 63, 81, 88, 90]. The particle strength increases with a decrease in its particle size. This is because the large particle contains larger cracks than the small particle [49, 88].

Impact stress acting on a particle strongly depends on the vertical impact velocity [64, 109]. In 1881, the elastic contact between spherical particle and flat wall was firstly analyzed by Hertz [46]. Hunter [47] subsequently analyzed the stress acting on the particle during the dynamic contact. Knight et al. [57] conducted particle impact test under various impact velocities and analyzed the impact stress acting on the particle using a theoretical model based on Hertz's theory [47]. The relationship between the

impact stress and impact velocity of the particle was described. From these studies, it was found that the impact stress strongly depends on the impact velocity, Young's modulus, Poisson's ratio, particle size, and impact angle.

The fragment size distribution after a particle breakage was described by a breakage function [65, 85, 104]. The breakage function means volume ratio in each fragment size. Among them, a power-low function is widely used as the breakage function [71, 110] because the experimental results of the fragment size distribution well obeyed a power-low function [56, 59].

As studies on whole process of the single particle process, Kalman et al. analyzed a particle attrition process in a pneumatic conveying system [53, 54, 55] and a particle compression process in a compression tester [35, 39]. The particle compression tester can change maximum compression force acting on the particle and compression speed. In the studies, they proposed a fatigue model of particle strength [39] based on Griffith's theory [37]. They reported that it is important for particle breakage to reduce the particle strength due to the repeated impacts against a wall. In addition, the fragment size distribution after particle attrition through the pneumatic conveying was predicted [40] using DEM (Discrete Element Method), CFD (Computational Fluid dynamics), and the attrition model [74].

Peukert et al. [103, 104] proposed a particle breakage model based on Rumpf's theory [84]. They used material parameters, f_{Mat} and $W_{\mathrm{m,\,min}}$ for modeling of particle breakage. f_{Mat} and $W_{\mathrm{m,\,min}}$ indicate a particle breakage probability and threshold energy of particle breakage, respectively. The particle breakage model was in good agreement with experimental results of the particle breakage probability [101, 103, 104, 105] and the fragment size distribution after the particle breakage [65, 70, 101, 103].

From these experimental studies, many stochastic models are proposed for single particle breakage. And many relationships between impact velocity of a particle and fragment size distribution after the particle breakage were understood. However, how the particle is broken when the particle impacts against a wall and what is happen while the particle breakage are not understood from the experimental approaches. Here, numerical simulation approach becomes a strong analysis tool to clarify the mechanism of single particle breakage.

The particle breakage was analyzed using a DEM (Discrete Element Method) model by Cundall and Strack [28] and modified by Thornton et al. [100]. In this numerical method, the agglomerated particle is made of spherical elements bonded each other by adhesion force [99]. Ning et al. [72] used the agglomerated particle model in order to analyze its breakage behavior under various impact velocities and impact angles. The calculated results of the particle breakage were in good agreement with experimental results of particle breakage of an agglomerated lactose particle. The number of the broken bonds in the agglomerated particle increased with an increase in the impact velocity [11, 67, 72, 91, 97]. The agglomerated particle was also used to analyze the fragment size distribution after the particle breakage [11, 97]. The effect of surface energy [91] and particle configuration [62] on the particle breakage, the impact force acting on a wall when the particle impacts against the wall [97], and the breakage behavior of a crystalline agglomerate [52] were also analyzed. Thornton et al. [98] simulated the compression breakage process using the dense and loose agglomerated particles. They showed that there was some rearrangement of the spherical elements near the compression walls in case of the dense agglomerated.

Potapov et al. [79, 80] developed a simulation method of breakage behavior of a solid particle. In this method, the solid particle is made of tetrahedral elements bonded each other by linear springs. The liner spring is broken when the force larger than the von Mises plasticity criterion [45] acts on the spring. The particle was impacted against a wall to analyze its breakage behavior under various impact velocities and spring strengths [76]. The width of size distribution of fragments after the particle breakage increased with an increase in the impact velocity. This was because that at low impact velocity crack radially propagates from the impact point to whole particle, which is called as “Mechanism I crack”. On the other hand, at high impact velocity crack propagate not only from the impact point but also from the “Mechanism I crack”, which are called as “Mechanism II crack” [77, 78]. This result showed the same tendency as the experimental result [17]. Then, Herbst and Potapov [43] simulated the particle motion and its breakage in a tumbling mill using the simulation method of breakage behavior of a solid particle [79, 80]. Particle size distribution of ground products in the tumbling mill was predicted. The predicted size distribution was in agreement with the

experimental results except the size range of fine particle [43, 44]. This method could not have enough accuracy in order to analyze the grinding processes.

Additionally, Moreno et al. [68] investigated the effect of the impact angle on particle breakage using the agglomerated DEM particle model [100]. The normal impact velocity strongly affected to the number of fragments after the particle breakage. Tomas et al. [87] simulated a particle impact against a wall using a DEM, FEM (Finite Element Method), and experimental test. Wittel et al. [109] also used a DEM and FEM to analyze the stress acting on a particle. These results of stress distribution inside a particle calculated from DEM were similar to the results calculated from a FEM. The calculated results of fragment size distribution after the particle breakage were well described by a Weibull function with two parameters and showed good agreement with the experimental results [2, 24, 25, 86].

Therefore, experimental and numerical analyses of single particle breakage have been studied by many researchers. Impact velocity, impact angle, and mechanical properties of the particle strongly affect in particle breakage phenomena such as propagation of crack and fragment size distribution. However, using this knowledge, the particle breakage in whole grinding process has not been analyzed in detail yet.

2. Modeling of grinding process

2.1. Population balance model

A population balance model [3, 41, 42] has been used since 1970's to understand temporal changes in particle size distribution in grinding processes. The population balance model mainly consists of a probability function of particle breakage (selection function) and a size distribution function of fragments after particle breakage (breakage function). The selection function and breakage function are generally determined from experimental test in each grinding machine. There are two types of the population balance model: 1) linear time-invariant model [83], in which the grinding rate does not change as time progress, and 2) linear time-variant model [4, 5], in which the grinding rate linearly changes as time progress. The particle size distribution predicted from

these population balance models was well accorded with the experimental one in wet grinding process. However, in general experimental operation, the grinding rate rapidly decreases in later stage of the grinding operation because it is difficult to apply external force on a particle due to decrease in its particle size and increase in fluid viscosity around the particle in the later stage. The change of the grinding rate cause a difference between the population balance models and the experiment results in later stage of grinding operation [8]. Thus, Bilgili et al. proposed a nonlinear time-variant model and applied it to some types of grinding machine [7, 9, 15]. The nonlinear time-variant population balance model can analyze the temporal change in particle size distribution of grinding products in a grinding chamber in detail and predict the particle size distribution after the grinding operation accurately. However, fluid flow and individual particle motion in a grinding process cannot be understood from the population balance model. Moreover, parameter of selection and breakage functions must be determined from the grinding operation experiment.

2.2. Numerical simulation of particle behavior in grinding process

Recently, numerical simulation has been used as a powerful tool for the analysis of grinding processes because of the improvement of computer performance. Among them, DEM, CFD, and DEM-CFD coupling model [102] are major simulation methods to analyze the motion of fluid, particle, and media in a grinding process.

The fluid and particle motion in a grinding process are calculated using CFD if the particle size is small and the particle phase is dilute. Anagnostopoulos et al. [1] calculated the fluid and particle motion in a wheel mill with a classifier and analyzed impact area and velocity of particles. Many researchers [6, 89, 106, 107] investigated the fluid and particle behaviors in a coal pulverizer because the particle size of ground coal significantly influenced efficiency of the coal combustion. For a jet mill, CFD was used to investigate the effect of the grinding fluid pressure, material feed rate, and feed fluid pressure on the grinding performance [95]. Impact condition between particles and walls of the grinding chamber has an important role in grinding performance of the jet mill. A fluid flow and particle motion in a dry impact pulverizer was also analyzed [18]. The location of particle impact against walls of the grinding chamber was investigated.

However, in order to analyze not only particle-to-wall contacts but also particle-to-particle contacts, a DEM-CFD coupling model [102] should be used [94]. On the other hand, media mills have been investigated by only the DEM simulation because the media motion is not strongly influenced by the fluid motion. The media motion and contacts between the media in the media mill are very important for grinding mechanism of the mill. A stirred ball mill, which is one of the major media mills, was analyzed by many researchers. They simulated fluid and media motion in the mill [10] and compared the calculated results with the experimental analysis by PEPT (Positron Emission Particle Tracking) [96]. They also investigated impact energy between each media [51] and effects of media size [34], viscosity of slurry [50] on the motion of the media in a stirred ball mill. In addition, the DEM simulation was also used in analyses of the media motion and impact energy between media-to-media collisions in a tumbling ball mill [27], single ball mill [58] and wet grinding processes [38, 69].

However, they did not consider the particle breakage in these simulation methods. So far, grinding phenomena in grinding process have been understood from the impact velocity, impact frequency, and impact energy etc.

2.3. Numerical simulation of particle breakage in grinding process

In terms of a concept of numerical modeling of the particle breakage, the numerical simulation methods can be categorized into two approaches, i.e., an agglomerated particle model [43] and a fragmentable particle model [14, 26]. In the agglomerated particle model, individual particles are treated as an agglomerate which consists of many small elements. In the fragmentable particle model, individual particles in a grinding process are split into small fragments based on a probability distribution function, i.e., a breakage function, when the particle is broken. Herbst and Potapov [43] used the agglomerated particle model to simulate particle breakage in a tumbling ball mill. The particle strength was obtained from the numerical simulation of breakage of single agglomerated particle [79, 80]. However, the calculated particle size distribution of the ground products did not show good agreement with the experimental ones, especially, within the range of fine particle size [44, 60]. Djordjevic et al. also simulated a motion and breakage of single agglomerated particle in an impact pulverizer [30].

From these studies, it is difficult for the agglomerate particle model to calculate fine fragments after the particle breakage because the minimum size of the fragments should be determined in advance.

On the other hand, the fragmentable particle model can simulate fine particles more accurately than the agglomerated particle model, because the minimum size of the fragments can be determined based on the impact conditions such as the impact velocity and particle size. Cleary [26] first described a particle breakage in a grinding process by the fragmentable particle model. He simulated particle breakages in a simple rotating two-dimensional box. However, mass of the particle before and after the particle breakage was not conserved.

Peukert [75] reported that if we want to understand the effect of material properties on particle breakage in grinding process from the numerical simulations, we should fully understand each breakage phenomena at micro, meso, and macro scale. He also mentioned the breakage phenomena at micro, meso, and macro scale should be simulated by MD (Molecular Dynamics), FEM, and DEM, respectively. But there is the big problem in connecting these scales which have different length sizes more than double figures. To connect these length scales, Kalman and his co-workers [12, 13, 56] described the single particle breakage based on a probability distribution function, i.e., a selection function and breakage function. Although they used the probability distribution functions and DEM simulation in order to simulate individual particle motion and its breakage in pneumatic conveying system, simulation results did not show good agreement with the experimental one. Since then, the simulation method has not been applied to a grinding process [13, 56]. Bruchmüller et al. [14] also simulated the particle motion and its breakage in a tumbling ball mill using the fragmentable particle model. In the study, the particle strength and fragment size distribution after the particle breakage were calculated from a model proposed by Vogel and Peukert [103]. However, Bruchmüller et al. could not successfully simulate the grinding process because the particle strength was not estimated properly.

Therefore, direct numerical method which can simultaneously simulate particle motion and its breakage in grinding process has not been established yet.

3. Control of grinding process

Control of particle size distribution of final ground products in dry grinding processes is an important issue because quality and performance of the final products are significantly affected by particle size of the ground products. However, it is very difficult to control the particle size of ground products even if the starting materials are ground under the same operating conditions. This is because that dynamic characteristic of the dry grinding process varies depending on the starting material properties such as moisture content and electro static charge. When we control the particle size of the ground products, dynamic characteristic of the dry grinding process should be understood. In addition, a monitoring technique of the particle size distribution of the grinding products is also essential. Thus, many investigations have been carried out for modeling of the dynamic characteristic and establishing the monitoring technique in order to control the particle size of the ground products. The wet tumbling ball mill is used for grinding mineral ore and consumes large energy. Chen et al. used an expert control method [21, 22] and model predictive control method [20, 23] for modelling the dynamic characteristic of the tumbling ball mill. They used feed rate of starting materials and water flow rate into grinding chamber, and water flow rate into classifier as the operating variables in order to control the size of the ground products. Galan et al. [33] introduced both feedback and feedforward control methods in a closed wet ball mill. Ramasamy et al. [82] showed a model predictive control method can more accurately control the particle size of ground products in a closed wet ball mill than a PI control method. Gommeren et al. [36] conducted an on-line measurement of the particle size in a jet mill and developed dynamic model of the jet mill. However, most of the studies on control of grinding process focused on the modelling of the dynamic characteristic in a closed wet ball milling process. There are few studies on the development of practical system for controlling particle size in dry grinding process. This is because that monitoring of the particle size of fine powders in dry system and modeling of dynamic characteristics of the dry grinding process are very difficult. Therefore, the development of a practical system for controlling a particle size of ground products in the dry grinding process is strongly required.

I-3. Scope of this thesis

The purpose of this thesis is to develop a numerical model which can simulate simultaneously the particle motion and its breakage in a dry grinding process, clarify the fundamental grinding mechanism, and develop a practical system for controlling particle size of ground products in the dry grinding process. This thesis consists of five chapters and each content is listed below.

Chapter I describes general background of this thesis. In the first part of this chapter, the general introduction is presented. The second part provides a review related to this thesis. The review consists of experimental and theoretical studies on single particle breakage, modeling of grinding processes using population balance model and numerical simulation method, and controlling the ground particle size of grinding process. The third part of this chapter mentioned the main objective and contents of this thesis.

Chapter II is devoted to numerical analysis of a dry impact pulverizer. First, a discrete phase model and computational fluid dynamics coupling model (DPM-CFD coupling model) is proposed in order to understand fluid and particle motion in the dry impact pulverizer. Validity of the proposed model was confirmed by measured data of fluid pressure in the grinding chamber and actual particle motion recorded by a high-speed video camera. Velocity and frequency of particle impact against entire wall of the grinding chamber are analyzed. The effect of the speed and geometries of the rotor on the impact condition at various particle sizes was investigated. The impact energy is calculated from the impact condition, which is compared with the measured median diameter of final ground products.

Chapter III is concerned with a development of numerical simulation method of particle motion and its breakage in a dry impact pulverizer. In this simulation method, the DPM-CFD coupling model is combined with a proposed particle breakage model which consists of three processes, i.e., particle strength, impact stress acting on the particle, and fragment size distribution after the particle breakage. First, modeling of the

three processes is conducted using Griffith's theory, Hertz's theory, and breakage function. The parameters of the three functions are obtained from two simple experiments, i.e., a uniaxial compression test and impact breakage test. The particle strength is measured from the uniaxial compression test. The fragment size distribution after particle breakage is obtained from the impact breakage test. The three processes could be modeled by the three functions as a function of the impact velocity and particle size. The motion and impact velocity of the particle are calculated from the DPM-CFD coupling model. In this proposed method, when the particle impacts against a vessel wall, the impact stress is calculated from the Hertz's theory as a function of the impact velocity. At the same time, the particle strength as a function of particle size is calculated from the Griffith's theory. If the impact stress is larger than the particle strength, the particle is broken and replaced with the smaller fragments. The size distribution of fragments is obtained from the proposed breakage function. The motion of the fragments is calculated again in the DPM-CFD coupling model. By repeating the above calculations over the whole particles in the dry impact pulverizer, the grinding phenomena can be simulated.

Chapter IV is directed to the development of feedback control system based on a fuzzy logic for controlling particle size of ground products in a dry impact pulverizer. First, on-line measurement system for measuring particle size distribution of the ground products suspended in dry system is developed. Validity of accuracy of the on-line measurement system is investigated. A feedback control method based on fuzzy logic is then established with consideration of dynamic characteristic such as a correlation between the rotor speed in the dry impact pulverizer and particle size of ground products. Finally, performance of the feedback control system is evaluated under various desired values of the ground particle size, starting materials, and external disturbances.

Chapter V summarizes the conclusions of this thesis.

References

1 Anagnostopoulos J, Bergeles G. Numerical investigation of the grinding process in a beater wheel mill with classifier. J. Eng. Gas Turbines Power. 1997;119:723-733.

2 Antonyuk S, Khanal M, Tomas J, Heinrich S, Morl L. Impact breakage of spherical granules: experimental study and DEM simulation. Chem. Eng. Process. 2006;45:838-856.

3 Austin LG. A review - Introduction to the mathematical description of grinding as a rate process. Powder Technol. 1971;5:1-17.

4 Austin LG, Bagga P. An analysis of fine dry grinding in ball mills. Powder Technol. 1981;28:83-90.

5 Austin LG, Shah J, Wang J, Gallagher E, Luckie PT. An analysis of ball-and-race milling: Part I. The Hardgrove mill. Powder Technol. 1981;29:263-275.

6 Bhasker C. Numerical simulation of turbulent flow in complex geometries used in power plants. Adv. Eng. Software. 2002;33:71-83.

7 Bilgili E, Capece M. Quantitative analysis of multi-particle interactions during particle breakage: A discrete non-linear population balance framework. Powder Technol. 2011;213:162-173.

8 Bilgilit E, Scarlett B. Population balance modeling of non-linear effects in milling processes. Powder Technol. 2005;153:59-71.

9 Bilgili E, Yepes J, Scarlett B. Formulation of a non-linear framework for population balance modeling of batch grinding: Beyond first-order kinetics. Chem. Eng. Sci. 2006;61:33-44.

10 Blecher L, Schwedes J. Energy distribution and particle trajectories in a grinding chamber of a stirred ball mill. Int. J. Miner. Process. 1996;44-45:617-627.

11 Boerefijn R, Ning Z, Ghadiri M. Disintegration of weak lactose agglomerates for inhalation applications. Int. J. Pharm. 1998;172:199-209.

12 Brosh T, Kalman H, Levy A. DEM simulation of particle attrition in dilute-phase pneumatic conveying. Granular Matter. 2010;13:175-181.

13 Brosh T, Kalman H, Levy A. Fragments spawning and interaction models for DEM breakage simulation. Granular Matter. 2011;13:765-776.

14 Bruchmüller J, van Wachem BGM, Gu S, Luo KH. Modelling discrete fragmentation of brittle particles. Powder Technol. 2011;208:731-739.

15 Capece M, Bilgili E, Dave R. Identification of the breakage rate and distribution parameters in a non-linear population balance model for batch milling. Powder Technol. 2011;208:195-203.

16 Cerdeira AM, Mazzotti M, Gander B. Miconazole nanosuspensions: Influence of formulation variables on particle size reduction and physical stability. Int. J. Pharm. 2010;396:210-218.

17 Charles RJ. High velocity impact in comminution. Min. Eng. 1956;205:1028-1032.

18 Chatzilamprou IG, Youds MW, Tierney MJ, Armstrong B. Numerical investigation of a developmental pneumatically fed impact pulveriser. Appl. Math. Modell. 2006;30:1180-1195.

19 Chenjea TW, Simbib DJ, Navara E. Relationship between microstructure, hardness, impact toughness and wear performance of selected grinding media for mineral ore milling operations. Mater. Des. 2004;25:11-18.

20 Chen X, Li Q, Fei S. Constrained model predictive control in ball mill grinding process. Powder Technol. 2008;186:31-39.

21 Chen X, Li Q, Fei S. Supervisory expert control for ball mill grinding circuits. Expert Syst. Appl. 2008;34:1877-1885.

22 Chen X, Li S, Zhai J, Li Q. Expert system based adaptive dynamic matrix control for ball mill grinding circuit. Expert Syst. Appl. 2009;36:716-723.

23 Chen X, Zhai J, Li S, Li Q. Application of model predictive control in ball mill grinding circuit. Miner. Eng. 2007;20:1099-1108.

24 Cheong YS, Reynolds GK, Salman AD, Hounslow MJ. Modelling fragment size distribution using two-parameter Weibull equation. Int. J. Miner. Process. 2004;74:227-237.

25 Chunsheng L, Danzer R, Franz DF. Fracture statistics of brittle materials: Weibull or normal distribution. Phys. Rev. E. 2002;65:067102.

26 Cleary PW. Recent advances in DEM modelling of tumbling mills. Miner. Eng. 2001;14:1295-1319.

27 Cleary PW, Sinnott MD, Morrison RD. DEM prediction of particle flows in grinding processes. Int. J. Numer. Methods Fluids. 2008;58:319-353.

28 Cundall PA, Strack ODL. Discrete numerical model for granular assemblies. Geotechnique. 1979;29:47-65.

29 Davies IJ. Best estimate of Weibull modulus obtained using linear least squares analysis: An improved empirical correction factor. J. Mater. Sci. 2004;39:1441-1444.

30 Djordjevic N, Shi FN, Morrison RD. Applying discrete element modeling to vertical and horizontal shaft impact crushers. Miner. Eng. 2003;16:983-991.

31 Duan C, Wen X, Shi C, Zhao Y, Wen B, He Y. Recovery of metals from waste printed circuit boards by a mechanical method using a water medium. J. Hazard. Mater. 2009;166:478-482.

32 Fogagnolo JB, Velasco F, Robert MH, Torralba JM. Effect of mechanical alloying on the morphology, microstructure and properties of aluminium matrix composite powders. Mater. Sci. Eng., A. 2003;342:131-143.

33 Galan O, Barton GW, Romagnoli JA. Robust control of a SAG mill. Powder Technol. 2002;124:264-271.

34 Gers R, Climent E, Legendre D, Anne-Archard D, Frances C. Numerical modelling of grinding in a stirred media mill: Hydrodynamics and collision characteristics. Chem. Eng. Sci. 2010;65:2052-2064.

35 Goder D, Kalman H, Ullmann A. Fatigue characteristics of granular materials. Powder Technol. 2002;122:19-25.

36 Gommeren HJC, Heitzmann DA, Moolenaar JAC, Scarlett B. Modelling and control of a jet mill plant. Powder Technol. 2000;108:147-154.

37 Griffith AA. The theory of rupture. In: 1st International Congress of Applied Mechanics; 1924; Delft, Nederland. p. 55-63.

38 Gudin D, Turczyn R, Mio H, Kano J, Saito F. Simulation of the movement of beads by the DEM with respect to the wet grinding process. AlChE J. 2006;52:3421-3426.

39 Han T, Kalman H, Levy A. Theoretical and experimental study of multi-compression particle breakage. Adv. Powder Technol. 2003;14:605-620.

40 Han T, Levy A, Kalman H. DEM simulation for attrition of salt during dilute-phase pneumatic conveying. Powder Technol. 2003;129:92-100.

41 Herbst JA, Grandy GA, Mika TS. On the development and use of lumped parameter models for continuous open- and closed-circuit grinding systems. Trans. Inst. Min. Metall., Sect. C. 1971;80:193-198.

42 Herbst JA, Mika TS. Mathematical simulation of tumbling mill grinding: an improved method. Rudy. 1970;18:70-75.

43 Herbst J, Potapov AV. Making a discrete grain breakage model practical for comminution equipment performance simulation. Powder Technol. 2004;143-144:144-150.

44 Herbst J, Potapov AV, Hambidge G, Rademan J. Modeling of diamond liberation and damage for debswana kimberlitic ores. Miner. Eng. 2008;21:766-769.

45 Herrmann HJ. Statistical models for the fracture of disordered media. Amsterdam: North-Holland; 1990.

46 Hertz H. Uber die Berechnung fester elastischer korper. J. Math. (Crelle's J.). 1881;92:174-196.

47 Hunter SC. Energy absorbed by elastic waves during impact. J. Mech. Phys. Solids. 1957;5:162-171.

48 Iwasaki T, Kosaka K, Mizutani N, Watano S, Yanagida T, Tanaka H, Kawai T. Mechanochemical preparation of magnetite nanoparticles by coprecipitation. Mater. Lett. 2008;62:4155-4157.

49 Jansen U, Stoyan D. On the validity of the Weibull failure model for brittle particles. Granular Matter. 2000;2:165-170.

50 Jayasundara CT, Yang RY, Guo BY, Yu AB, Rubenstein J. Effect of slurryproperties on particle motion in IsaMills. Miner. Eng. 2009;22:886-892.

51 Jayasundara CT, Yang RY, Yu AB, Curry D. Discrete particle simulation of particle flow in the IsaMill process. Ind. Eng. Chem. Res. 2006;45:6349-6359.

52 Kafui KD, Thornton C. Numerical simulations of impact breakage of a spherical crystalline agglomerate. Powder Technol. 2000;109:113-132.

53 Kalman H. Attrition control by pneumatic conveying. Powder Technol. 1999;104:214-220.

54 Kalman H. Attrition of powders and granules at various bends during pneumatic conveying. Powder Technol. 2000;112:244-250.

55 Kalman H, Goder D. Design criteria for particle attrition. Adv. Powder Technol. 1998;9:153-167.

56 Kalman H, Rodnianski V, Haim M. A new method to implement comminution functions into DEM simulation of a size reduction system due to particle-wall collisions. Granular Matter. 2009;11:253-266.

57 Knight CG, Swain MV, Chaudhri MM. Impact of small steel spheres on glass surfaces. J. Mater. Sci. 1977;12:1573-1586.

58 Kwan CC, Mio H, Chen YQ, Ding YL, Saito F, Papadopoulos DG, Bentham AC, Ghadiri M. Analysis of the milling rate of pharmaceutical powders using the Distinct Element Method (DEM). Chem. Eng. Sci. 2005;60:1441-1448.

59 Lee H, Cho H, Kwon J. Using the discrete element method to analyze the breakage rate in a centrifugal/vibration. Powder Technol. 2010;198:364-372.

60 Lichter J, Lim K, Potapov A, Kaja D. New developments in cone crusher performance optimization. Miner. Eng. 2009;22:613-617.

61 Lim WL, McDowell GR, Collop AC. The application of Weibull statistics to the strength of railway ballast. Granular Matter. 2004;6:229-237.

62 Liu L, Kafui KD, Thornton C. Impact breakage of spherical, cuboidal and cylindrical agglomerates. Powder Technol. 2010;199:189-196.

63 Madjoubi MA, Bousbaa C, Hamidouche M, Bouaouadja N. Weibull statistical analysis of the mechanical strength of a glass eroded by sand blasting. J. Eur. Ceram. Soc. 1999;19:2957-2962.

64 Maxim RE, Salman AD, Pickles M, Hounslow MJ. Theoretical impact failure distribution of granules. Adv. Powder Technol. 2003;14:393-400.

65 Meier M, John E, Wieckhusen D, Wirth W, Peukert W. Generally applicable breakage functions derived from single particle comminution data. Powder Technol. 2009;194:33-41.

66 Merisko-Liversidge E, Liversidge GG. Nanosizing for oral and parenteral drug delivery: A perspective on formulating poorly-water soluble compounds using wet media milling technology. Adv. Drug Delivery Rev. 2011;63:427-440.

67 Mishra BK, Thornton C. Impact breakage of particle agglomerates. Int. J. Miner. Process. 2001;61:225-239.

68 Moreno R, Ghadiri M, Antony SJ. Effect of the impact angle on the breakage of agglomerates: a numerical study using DEM. Powder Technol. 2003;130:132-137.

69 Mori H, Mio H, Kano J, Saito F. Ball mill simulation in wet grinding using a tumbling mill and its correlation to grinding rate. Powder Technol. 2004;143-144:230-239.

70 Morrison RD, Shi F, Whyte R. Modelling of incremental rock breakage by impact–For use in DEM models. Miner. Eng. 2007;20:303-309.

71 Nikolov S. A performance model for impact crushers. Miner. Eng. 2002;15:715-721.

72 Ning Z, Boerefijn R, Ghadiri M, Thornton C. Distinct element simulation of impact breakage of lactose agglomerates. Adv. Powder Technol. 1997;8:15-37.

73 Ohara S, Tan Z, Noma J, Hanaichi T, Sato K, Abe H. Collision synthesis of unique carbon nanomaterials inspired by the Allende meteorite. Solid State Commun. 2010;150:196-200.

74 Papadopulos DG, Teo CS, Ghadiri M. Attrition of common salt. 3rd World Congress on Particle Technology. 1998 156.

75 Peukert W. Material properties in fine grinding. Int. J. Miner. Process. 2002;74:S3-S17.

76 Potapov AV, Campbell CS. Computer simulation of impact-induced particle breakage. Powder Technol. 1994;81:207–216.

77 Potapov AV, Campbell CS. Parametric dependence of particle breakage mechanisms. Powder Technol. 2001;120:164-174.

78 Potapov AV, Campbell CS. The two mechanisms of particle impact breakage and the velocity effect. Powder Technol. 1997;93:13-21.

79 Potapov AV, Campbell CS, Hopkins MA. A two-dimensional dynamic simulation of solid fracture part II: examples. Int. J. Mod. Phys. C. 1995;6:399-425.

80 Potapov AV, M.A. H, Campbell CS. A two-dimensional dynamic simulation of solid fracture part I: description of the model. Int. J. Mod. Phys. C. 1995;6:371-398.

81 Prater WL. Comparison of ceramic material effects on the flexural Weibull statistics and fracture of high volume fraction particle reinforced aluminum. Mater. Sci. Eng., A. 2006;420:187-198.

82 Ramasamy M, Narayanan SS, Rao CDP. Control of ball mill grinding circuit using model predictive control scheme. J. Process Control. 2005;15:273-283.

83 Reid KJ. A solution to the batch grinding equation. Chem. Eng. Sci. 1965;20:953-963.

84 Rumpf H. Physical aspects of comminution and new formulation of a law of comminution. Powder Technol. 1973;7:145-159.

85 Sahoo R. Review: An investigation of single particle breakage tests for coal handling system of the gladstone port. Powder Technol. 2006;161:158-167.

86 Salman AD, Biggs CA, Fu J, Angyal I, Szabo M, Hounslow MJ. An experimental investigation of particle fragmentation using single particle impact studies. Powder Technol. 2002;128:36-46.

87 Schubert W, Khanal M, Tomas J. Impact crushing of particle-particle compounds-experiment and simulation. Int. J. Miner. Process. 2005;75:41-52.

88 Sebastian LG, Vallejo LE. Application of Weibull statistics to the tensile strength of rock aggregates. J. Geotech. Geoenviron. Eng. 2006;132:786-790.

89 Shah KV, Vuthaluru R, Vuthaluru HB. CFD based investigations into optimization of coal pulveriser performance: Effect of classifier vane settings. Fuel Process. Technol. 2009;90:1135-1141.

90 Subero-Couroyer C, Ghadiri M, Brunard N, Kolenda F. Weibull analysis of quasi-static crushing strength of catalyst particles. Chem. Eng. Res. Des. 2003;81:953-962.

91 Subero J, Ning Z, Ghadiri M, Thornton C. Effect of interface energy on the impact strength of agglomerates. Powder Technol. 1999;105:66-73.

92 Suryanarayana C. Mechanical alloying and milling. Prog. Mater Sci. 2001;46:1-184.

93 Tan Z, Chihara H, Koike C, Abe H, Kaneko K, Sato K, Ohara S. Interstellar analogs from defective carbon nanostructures account for interstellar extinction. The Astronomical J. 2010;140:1456-1461.

94 Teng S, Wang P, Zhanga Q, Gogos C. Analysis of fluid energy mill by gas-solid two-phase flow simulation. Powder Technol. 2011;208:684-693.

95 Teng S, Wang P, Zhu L, Young MW, Gogos CG. Experimental and numerical analysis of a lab-scale fluid energy mill. Powder Technol. 2009;195:31-39.

96 Theuerkauf J, Schwedes J. Theoretical and experimental investigation on particle and fluid motion in stirred media mills. Powder Technol. 1999;105:406-412.

97 Thornton C, Ciomocos MT, Adams MJ. Numerical simulations of agglomerate impact breakage. Powder Technol. 1999;105:74-82.

98 Thornton C, Ciomocos MT, Adams MJ. Numerical simulations of diametrical compression tests on agglomerates. Powder Technol. 2004;140:258-267.

99 Thornton C, Yin KK. Impact of elastic spheres with and without adhesion. Powder Technol. 1991;65:153-166.

100 Thornton C, Yin KK, Adams MJ. Numerical simulation of the impact fracture and fragmentation of agglomerates. J. Phys. D: Appl. Phys. 1996;29:424-435.

101 Toneva P, Peukert W. A general approach for the characterization of fragmentation problems. Adv. Powder Technol. 2007;18:39-51.

102 Tsuji Y, Kawaguchi T, Tanaka T. Discrete particle simulation of two-dimensional fluidization bed. Powder Technol. 1993;77:79-87.

103 Vogel L, Peukert W. Breakage behaviour of different materials—construction of a mastercurve for the breakage probability. Powder Technol. 2003;129:101-110.

104 Vogel L, Peukert W. Characterisation of grinding-relevant particle properties by inverting a population balance model. Part. Part. Syst. Charact. 2002;19:149-157.

105 Vogel L, Peukert W. Determination of material properties relevant to grinding by practicable labscale milling tests. Int. J. Miner. Process. 2004;74S:S329-S338.

106 Vuthaluru R, Kruger O, Abhishek M, Pareek VK, Vuthaluru HB. Investigation of wear pattern in a complex coal pulveriser using CFD modelling. Fuel Process. Technol. 2006;87:687-694.

107 Vuthaluru HB, Pareek VK, Vuthaluru R. Multiphase flow simulation of a simplified coal pulveriser. Fuel Process. Technol. 2005;86:1195-1205.

108 Wang J, Yin S, Komatsu M, Zhang Q, Saito F, Sato T. Photo-oxidation properties of nitrogen doped SrTiO3 made by mechanical activation. Appl. Catal., B. 2004;52:11-21.

109 Wittel FK, Carmona HA, Kun F, Herrmann HJ. Mechanisms in impact fragmentation. Int. J. Fract. 2008;154:105-117.

110 Wu SZ, Chaua KT, Yu TX. Crushing and fragmentation of brittle spheres under double impact test. Powder Technol. 2004;143-144:41-55.

111 Wu Z, Fang B, Bonakdarpour A, Sun A, Wilkinson DP, Wang D. WS_2 nanosheets as a highly efficient electrocatalyst for hydrogen evolution reaction. Appl. Catal., B. 2012;125:59-66.

Chapter II

Numerical simulation of fluid and particle behavior in dry impact pulverizer

II-1. Numerical analysis of fluid and particle behavior in dry impact pulverizer

1. Introduction

Grinding phenomena in a dry impact pulverizer which consists of high speed rotating rotor and a static concavo-convex stator is very complex because of high-speed air and particle flows in a gap between the complicated geometries inside the grinding chamber. The particles are mainly broken due to the impact against a wall of the rotor and stator. Therefore, it is very important to understand the fluid and particle motion in the dry impact pulverizer. However, it is difficult to experimentally analyze the complex fluid and particle motion in the dry impact pulverizer.

Recently, numerical simulations have become powerful tools for the analysis of complex fluid flow and individual particle motion in many particulate processes. A coupling model of a computational fluid dynamics with a discrete phase model (CFD-DPM coupling model) is often used in gas-solid two-phase systems if the particle size is small and the particle phase is dilute. However, analysis of fluid and particle motion in the dry impact pulverizer has not been reported anywhere.

In this chapter, the fluid flow and individual particle motion were numerically analyzed using the CFD-DPM coupling model to investigate mechanism of the particle impact in the dry impact pulverizer. In order to confirm validity of the proposed numerical model, calculated result of the fluid pressure was compared with the experimental one. Pressure and velocity of the fluid in the impact pulverizer were then analyzed. The particle motion was numerically calculated and compared with the actual particle motion recorded by a high-speed video camera. Velocities and frequencies of the particle-to-wall impacts were then analyzed at various rotor speeds and particle diameters, and then the grinding mechanism in the impact pulverizer was discussed.

2. Dry impact pulverizer

Fig. 2.1.1 shows a schematic diagram of dry impact pulverizer (LM-05, Fuji Paudal Co., Ltd.) used in this study. The impact pulverizer consists of a high-speed rotating rotor having eight hammers with dimensions of 15 mm in width, 8 mm in height, and 8 mm in depth, a grinding chamber with a diameter of 119 mm and a depth of 30 mm, a concavo-convex-shaped stator in the grinding chamber, a classification screen with opening size of 0.7 mm in diameter, and a collection pot of ground products. The stator which is a static part of internal grinding chamber surrounds the rotating rotor. A clearance between the hammer tip and the stator protuberance is 0.5 mm. The maximum rotating speed of the rotor is 267 rps, which is equivalent to the tip speed of 105.7 m/s. The classification screen is installed between the grinding chamber and the collection pot. A starting particulate material is continuously fed into the center of the grinding chamber and ground between the high-speed rotating rotor and the static stator. The ground particles which pass through the screen are collected in the pot as the final ground products.

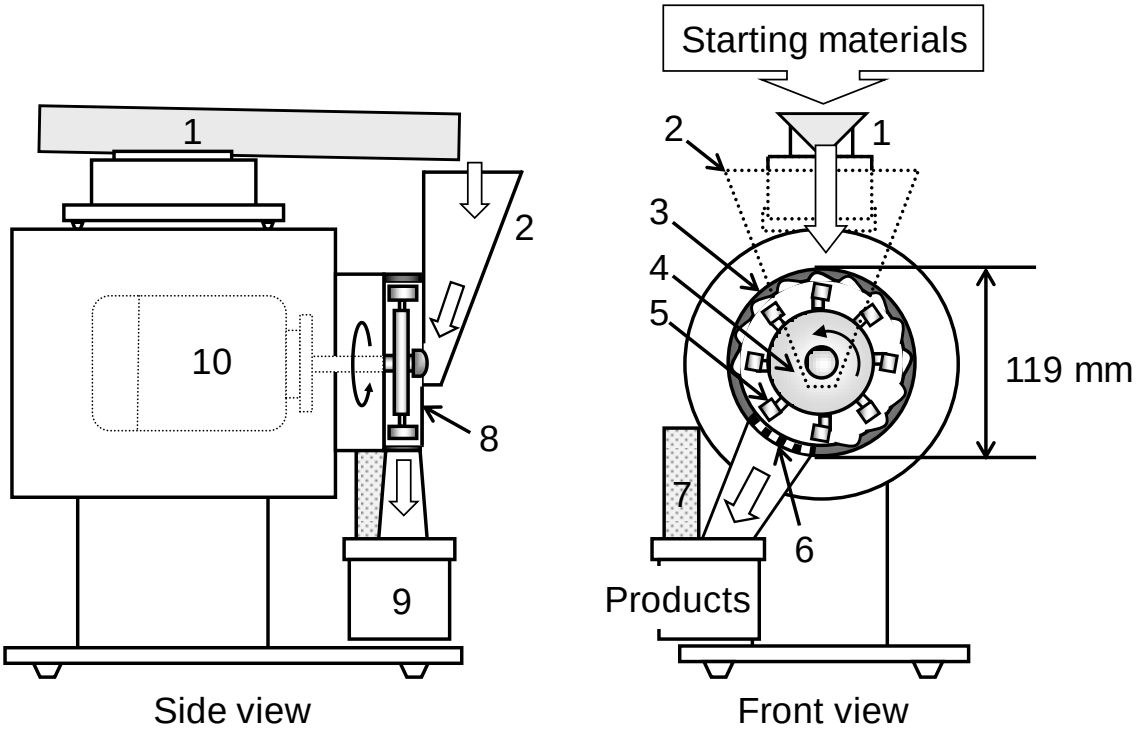

1. Feeder
2. Front cover
3. Stator
4. Rotor
5. Hammer
6. Classification screen
7. Bag filter
8. Grinding chamber
9. Collection pot
10. Motor

Fig. 2.1.1. Schematic diagram of dry impact pulverizer used in this study.

3. Numerical modeling

3.1. Modeling of fluid flow

The fluid flow and individual particle motion in the impact pulverizer were simulated using a CFD-DPM coupling model. The fluid flow was calculated using the CFD. The fluid flow in the impact pulverizer is extremely high-speed turbulent flow caused by the high-speed rotating rotor with hammers. Therefore, in this CFD simulation, the fluid was assumed to be a viscous and compressible fluid, and the fluid flow was considered as turbulence and unsteady flow. The effect of the turbulent flow was described by a governing equation of fluid flow by Reynolds averaging. In the Reynolds averaging, the fluid velocity $\boldsymbol{u}$ is described by the averaged velocity $\bar{\boldsymbol{u}}$ and fluctuating velocity $\boldsymbol{u}'$ as shown in the following equation:

$$\boldsymbol{u} = \bar{\boldsymbol{u}} + \boldsymbol{u}' \tag{2.1.1}$$

Scholar variables φ such as fluid pressure and temperature are also described by the averaged scholar variable $\bar{\varphi}$ and fluctuating scholar variable φ' as shown in the following equation:

$$\varphi = \bar{\varphi} + \varphi' \tag{2.1.2}$$

Fluid flow was calculated by solving the equation of continuity, the Reynolds-averaged Navier-Stokes (RANS) equation, and the equation of energy. The governing equations are as follows:

Equation of continuity

$$\frac{\partial}{\partial t}\rho + \nabla \cdot \left(\rho \bar{\boldsymbol{u}}\right) = 0 \tag{2.1.3}$$

Equation of motion (RANS equation)

$$\frac{\partial}{\partial t}(\rho\bar{\boldsymbol{u}})+\nabla\cdot(\rho\bar{\boldsymbol{u}}\bar{\boldsymbol{u}})=-\nabla\bar{p}-\nabla\cdot\left[-\mu(\nabla\bar{\boldsymbol{u}})+\rho\overline{\boldsymbol{u}'\boldsymbol{u}'}\right]+\rho\boldsymbol{g} \tag{2.1.4}$$

Equation of energy

$$\frac{\partial}{\partial t}(\rho C_p\bar{T})+\nabla\cdot(\rho C_p\bar{T}\bar{\boldsymbol{u}})=-\nabla\cdot\left[-k_{therm}\nabla\bar{T}+\rho C_p\overline{T'\boldsymbol{u}'}\right] \tag{2.1.5}$$

where ρ, $\bar{p}$, μ, and $\boldsymbol{g}$ are fluid density, averaging fluid pressure, fluid viscosity, and gravity, respectively. C_p, $\bar{T}$, and k_{therm} are constant pressure specific heat, averaged fluid temperature, and effective heat conductivity of fluid, respectively. The fluid density is calculated by the following equation, which indicated state of an ideal gas:

$$\rho=\frac{p_0+p}{(R_\mathrm{m}/M_\mathrm{w})T} \tag{2.1.6}$$

where p_0, R_m, and M_w are standard pressure, molar gas constant, and molar mass of the fluid, respectively. In this study, modified k-ε turbulent model [12] was used as a turbulent model. The Boussinesq approximation [6] was applied to solve the Reynolds' stress term $\rho\overline{\boldsymbol{u}'\boldsymbol{u}'}$ in Eq. (2.1.4) and the temperature transfer term $\rho C_p\overline{T'\boldsymbol{u}'}$ in Eq. (2.1.5). The Reynolds' stress term was calculated by the following equation:

$$\rho\overline{\boldsymbol{u}'\boldsymbol{u}'}=-\mu_\mathrm{t}\left(\nabla\bar{\boldsymbol{u}}+(\nabla\bar{\boldsymbol{u}})^\mathrm{T}-\frac{2}{3}(\nabla\cdot\bar{\boldsymbol{u}})\boldsymbol{\delta}\right)+\frac{2}{3}\rho k\boldsymbol{\delta} \tag{2.1.7}$$

where k and $\boldsymbol{\delta}$ indicate the turbulent kinetic energy and unit tensor. μ_t is the eddy viscosity coefficient, which is expressed by the following equation:

$$\mu_\mathrm{t}=\rho C_\mu\frac{k^2}{\varepsilon} \tag{2.1.8}$$

where ε is turbulent kinetic dissipation rate. C_μ indicates coefficient of eddy viscosity.

Because C_μ was calculated at each computational fluid cell in each time step in the modified k-ε turbulent model, the modified k-ε turbulent model could simulate a swirling flow more accurately than a standard k-ε turbulent model [7]. On the other hand, the temperature transfer term $\rho C_p \overline{T'\boldsymbol{u}'}$ in Eq. (2.1.5) was calculated from the following equations:

$$\rho C_p \overline{T'\boldsymbol{u}'} = -\frac{C_p \mu_t}{\mathrm{Pr_t}} \left(\nabla \overline{T}\right) \tag{2.1.9}$$

where $\mathrm{Pr_t}$ is Prandtl number of turbulence.

The turbulent kinetic energy k and turbulent kinetic dissipation rate ε were calculated from the following equations.

Transport equation of turbulent kinetic energy

$$\frac{\partial}{\partial t}(\rho k) + \nabla \cdot (\rho k \overline{\boldsymbol{u}}) = \nabla \cdot \left[\left(\mu + \frac{\mu_t}{\sigma_k} \right) \nabla k \right] + G_k + G_b - \rho \varepsilon - Y_M \tag{2.1.10}$$

Transport equation of turbulent energy dissipation rate

$$\frac{\partial}{\partial t}(\rho \varepsilon) + \nabla \cdot (\rho \varepsilon \overline{\boldsymbol{u}}) = \nabla \cdot \left[\left(\mu + \frac{\mu_t}{\sigma_\varepsilon} \right) \nabla \varepsilon \right] + \rho C_1 S \varepsilon + \rho C_2 \frac{\varepsilon^2}{k + \sqrt{\nu \varepsilon}} \tag{2.1.11}$$

where, G_k, G_b, and Y_M are terms of generation of turbulent kinetic energy due to the mean velocity gradients, generation of turbulent kinetic energy due to buoyancy, and contribution of the fluctuating dilatation in compressible turbulence to the overall dissipation rate, respectively. σ_k and σ_ε are turbulent Prandtl numbers for k and ε, respectively. C_1 and C_2 are the coefficients [12] of generation term of ε and dissipation ratio of ε. S and ν are modulus of mean rate of strain tensor and fluid kinematic viscosity. C_1 and S are calculated from the following equations:

$$C_1 = \max\left(0.43,\ \frac{\eta}{\eta+5}\right) \tag{2.1.12}$$

$$\eta = S\frac{k}{\varepsilon} \tag{2.1.13}$$

$$S = \sqrt{2S_{ij}S_{ji}} \tag{2.1.14}$$

$$S_{ij} = \frac{1}{2}\left(\frac{\partial u_j}{\partial x_i} + \frac{\partial u_i}{\partial x_j}\right) \tag{2.1.15}$$

At the wall boundary, the fluid velocity gradients are high, requiring excessive fluid cell refinements to calculate the turbulent kinetic energy dissipation rate ε in Eq. (2.1.11) and the generation term of turbulent kinetic energy due to average fluid velocity gradient G_k in Eq. (2.1.10) at the boundary. In order to alleviate such excessive fluid cell refinements, the Launder-Spalding wall function [8] was used at both rotating and stationary wall boundaries in this study. In this function, the dimensionless fluid velocity U^* at a node P of the fluid cell adjacent to a wall and the dimensionless distance y^* between the wall and the node P were used. U^* and y^* are given by the following equations:

$$U^* \equiv \frac{U_P\left(C_\mu{}^{0.5}k_P\right)^{0.5}}{\tau_w/\rho} \tag{2.1.16}$$

$$y^* \equiv \frac{\rho\left(C_\mu{}^{0.5}k_P\right)^{0.5}y_P}{\mu} \tag{2.1.17}$$

where U_P, k_P, and y_P are the average fluid velocity at the node P, the turbulent kinetic energy at the node P, and the distance between the wall and the node P, respectively.

τ_w is the wall shear stress. If $y^* \geq 11.225$ [8], the relation between U^* and y^* was described by the following equation:

$$U^* = \frac{1}{\kappa}\ln\left(a_w y^*\right) \tag{2.1.18}$$

where κ and a_w are the von Karman constant (= 0.4187) and the empirical parameter (= 9.793) [8], respectively. On the other hand, if $y^* < 11.225$, the relation between U^* and y^* was described by the following equation:

$$U^* = y^* \tag{2.1.19}$$

By using these relations between U^* and y^*, τ_w in Eq. (2.1.16) was calculated. Therefore, ε and G_k at the boundary were calculated from the following equations:

$$\varepsilon = \tau_w \frac{C_\mu^{0.75} k_P^{1.5}}{\kappa y_P} \tag{2.1.20}$$

$$G_k \approx \tau_w \frac{\partial U}{\partial y} = \tau_w \frac{\tau_w}{\kappa \rho k_P^{0.5} y_P} \tag{2.1.21}$$

The fluid pressure and fluid velocity were solved by a SIMPLE algorithm [11]. The convection term and diffusion term in Eq. (2.1.4) were discretized using a 1st-order upwind difference scheme and a 2nd-order central-difference scheme, respectively. The fluid pressure and velocity were calculated by the discretized equations. Then, the fluid pressure and velocity was corrected by the discretized equation of continuity. A fluid relaxation coefficient (= 0.3), and momentum relaxation coefficient (= 0.7) were used for the calculation of the correction amount. By using the corrected fluid pressure and velocity, equation of energy and equations of turbulent kinematic energy and turbulent dispersion ratio which were discretized using a 1st-order upwind difference scheme

were calculated. If the calculated fluid pressure, velocity, turbulent kinematic energy, turbulent dispersion ratio, and fluid energy met convergence conditions, the time step was advanced. If not, the calculation procedure as shown in above was calculated again. The time-derivative terms in the governing equations were discretized using a 1st order full-implicit method.

3.2. Modeling of particle motion

The individual particle motion was calculated using the DPM. In the DPM, the particles are treated as point mass, and the particle-to-particle impacts are not taken into account. The particle phase in the dry impact pulverizer can be considered as a dilute phase, because particle volume fraction in the pulverizer is generally less than 10 vol% of air volume. The individual particle motion was calculated by solving the equation of motion as follows:

$$\frac{\mathrm{d}\boldsymbol{u}_\mathrm{p}}{\mathrm{d}t} = \boldsymbol{F}_d + \frac{\boldsymbol{g}\left(\rho_\mathrm{p} - \rho\right)}{\rho_\mathrm{p}} \tag{2.1.22}$$

where $\boldsymbol{u}_\mathrm{p}$ and ρ_p are particle velocity and particle density, respectively. The fluid drag force, $\boldsymbol{F}_d$ is written as

$$\boldsymbol{F}_d = \frac{18\mu}{\rho_\mathrm{p} {d_\mathrm{p}}^2} \frac{C_d \mathrm{Re}_\mathrm{p}}{24} \left(\boldsymbol{u} - \boldsymbol{u}_\mathrm{p}\right) \tag{2.1.23}$$

$$\mathrm{Re}_\mathrm{p} = \frac{\rho d_\mathrm{p} \left| u_\mathrm{p} - u \right|}{\mu} \tag{2.1.24}$$

$$C_d = \frac{K_1}{\mathrm{Re}_\mathrm{p}} + \frac{K_2}{\mathrm{Re}_\mathrm{p}^2} + K_3 \tag{2.1.25}$$

where d_p and Re_p are particle diameter, and particle Reynolds number, respectively. The coefficient of fluid drag C_d was obtained from the empirical correlation of Haider and Levenspiel [5]. K_1, K_2, and K_3 were determined from Re_p [10]. The particle velocity ${\boldsymbol{u}_\mathrm{p}}^{n+1}$ at the new time-step n+1 was calculated from the particle velocity ${\boldsymbol{u}_\mathrm{p}}^{n}$ at the old time-step n:

$$\boldsymbol{u}_{\mathrm{p}}^{\,n+1} = \boldsymbol{u}_{\mathrm{p}}^{\,n} + \frac{\frac{\Delta t}{\tau_{\mathrm{p}}}\left(\boldsymbol{u}^{n} + \frac{1}{2}\Delta t \boldsymbol{u}_{\mathrm{p}}^{\,n} \cdot \nabla \boldsymbol{u}^{n}\right) + \Delta t \frac{\boldsymbol{g}\left(\rho_{\mathrm{p}} - \rho\right)}{\rho_{\mathrm{p}}}}{1 + \frac{1}{2}\frac{\Delta t}{\tau_{\mathrm{p}}}} \tag{2.1.26}$$

where Δt and τ_{p} are time-step and particle relaxation time. τ_{p} was calculated according to the following equation:

$$\tau_{\mathrm{p}} = \frac{1}{F_d} = \frac{\rho_{\mathrm{p}} d_{\mathrm{p}}^{\,2}}{18\mu} \frac{24}{C_d \, Re_{\mathrm{p}}} \tag{2.1.27}$$

In the dry impact pulverizer, volume ratio of the particle phase to the air fluid phase is very low. In addition, the size of the particle is relatively small. Therefore, a one-way coupling model was used for the coupling between DPM and CFD. In the one-way coupling model, the effect of the fluid motion on the particle motion was only considered, while effect of the particle motion on the fluid motion was not considered.

The particles were rebound against the wall. The interaction between the particle and wall was defined by the normal and tangential restitution coefficients, which were calculated by following equations:

$$e_n = \frac{u_{n,reb}}{u_{n,imp}}, \quad e_t = \frac{u_{t,reb}}{u_{t,imp}} \tag{2.1.28}$$

where u_{imp} and u_{reb} are impact velocity of particle to wall and rebound velocity of particle from wall, respectively. The restitution coefficients were set as e_n = 0.3 and e_t = 1 [13]. The size distribution of the particles was treated as mono-disperse. The breakage and size reduction of the particles were not considered in the numerical simulation.

3.3. Modeling of geometry of dry impact pulverizer

Three-dimensional geometry for the numerical simulation was created from the CAD data of the dry impact pulverizer using the GAMBIT (Ver. 2.4.6, Fluent Inc.). The actual appearance and simulated geometry of the pulverizer are shown in Fig. 2.1.2a and 2.1.2b. Actual appearance and computational fluid cells of the grinding chamber are also indicated in Fig. 2.1.2c and 2.1.2d. A cross section of the computational fluid cells of the grinding chamber is shown in Fig. 2.1.2e. The computational fluid cells mostly consisted of hexahedral elements in order to improve the calculation speed and stability. The total number of the cells was 490,436. The computational fluid cells were composed of three regions: (1) front cover with the inlet boundary of fluid, (2) grinding chamber with the rotating rotor, and (3) stator and collecting pot with the outlet boundary of fluid. The computational fluid cells in the region (2) were rotated with the motion of the rotor, although the computational fluid cells in the region (1) and (3) were stationary. The interface between the rotating cells and the stationary cells was treated using a sliding mesh model [9].

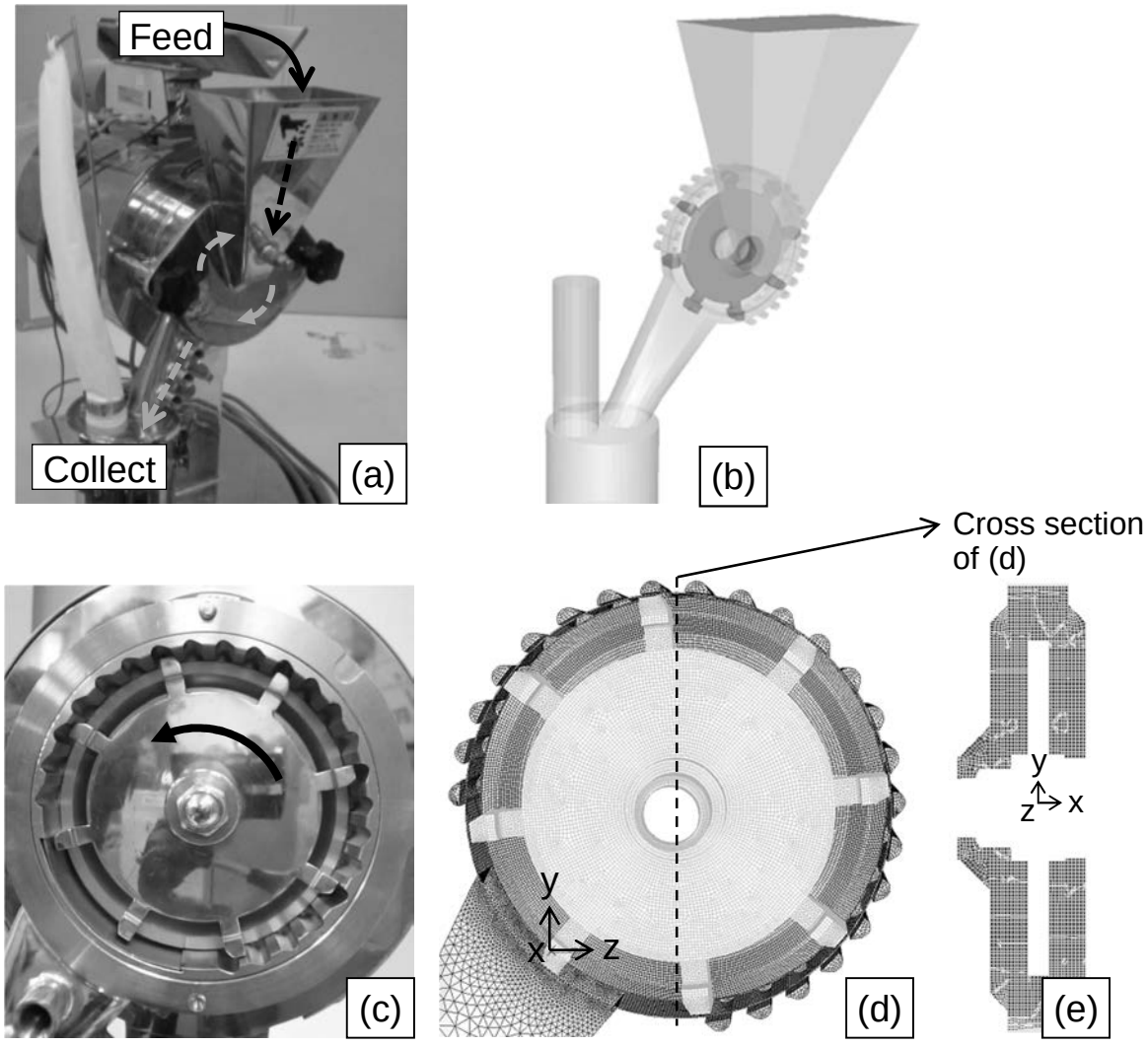

Fig. 2.1.2. Actual appearance and simulated geometry of impact pulverizer. (a) Actual overall view of pulverizer. (b) Simulated geometry of pulverizer. (c) Actual view of grinding chamber. (d) Computational fluid cells of grinding chamber. (e) Cross section of computational fluid cells.

3.4. Calculation conditions

Calculation conditions used in this simulation are listed in Table 2.2.1. In order to reduce the total calculation time and to improve the calculation stability, the fluid motion in the dry impact pulverizer was calculated in order of incompressible steady calculation, incompressible unsteady calculation, and compressible unsteady calculation. After converging the calculation of the fluid motion, 12 particles were continuously fed into the grinding chamber per 1-timestep (8.33 μs). The starting particles had an initial velocity which was almost the same velocity as the actual grinding operation. Impact velocity and impact frequency were analyzed when the number of particle in the grinding chamber was almost constant. At this time, the number of the particles was almost 48,000. The rotating speed of the rotor was set at 267 rps.

Table 2.1.1 Calculation conditions

Fluid density (101.3 kPa, 288 K)	1.225	[kg/m^3]
Fluid viscosity (101.3 kPa, 288 K)	1.789×10^{-5}	[Pa·s]
Inlet pressure	101.3	[kPa]
Outlet pressure	101.3	[kPa]
Time step	8.33	[μs]
Particle density	1500	[kg/m^3]
Restitution coefficient		
Normal impact between particle-to-wall	0.3	[–]
Tangential impact between particle-to-wall	1.0	[–]
Number of fluid cells	490,436	[–]
Rotating speed of rotor	133, 200, 267	[rps]
Particle diameter	25, 50, 100, 250	[μm]
Initial velocity of starting particles		
x-direction	−1.6	[m/s]
y-direction	− 11.8	[m/s]
z-direction	0	[m/s]

4. Experimental

In order to validate our proposed numerical model, the fluid pressure and particle motion in the impact pulverizer were experimentally investigated. A schematic diagram of the experimental set-up is shown in Fig. 2.1.3. Geometry and size of the impact pulverizer used in this experiment were the same as that used in the numerical simulation. A pressure sensor (AP-12S, Keyence Corp.) was used for measurement of fluid pressure at the inside of the grinding chamber. A pressure tap was installed at the top of the grinding chamber. The front cover was made of a transparent acrylic plastic, which allowed to observe the particle motion. The particle motion was recorded using a high-speed video camera (Phantom V710, Vision Research Inc.). Recording speed of the high-speed video camera was set as 100,000 frames per second. Spherical particles made of sucrose and starch (Nonpareil-101, Freund Corp.) were used as the experimental model particles. The size range of the model particles was between 500 and 710 μm.

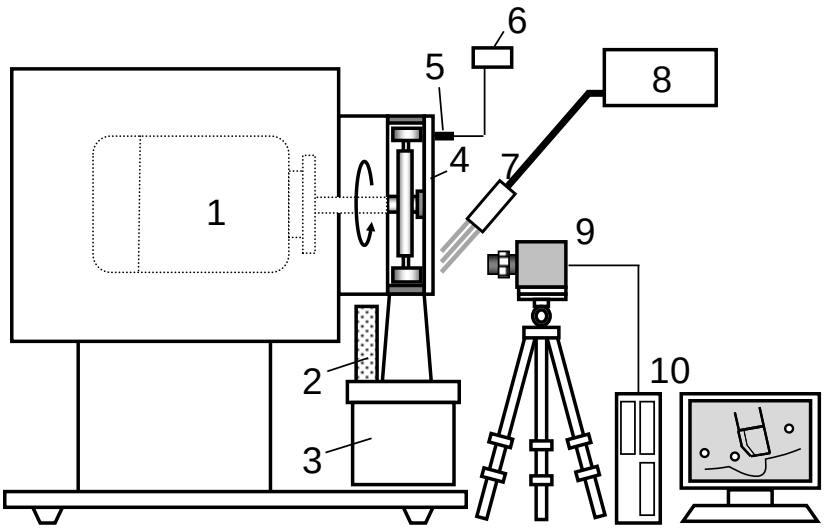

1. Motor
2. Bag filter
3. Collection pot
4. Front cover
5. Pressure tap
6. Pressure sensor
7. Illumination lamp
8. Light source
9. High speed video camera
10. Data analysis system

Fig. 2.1.3. Experimental set-up for measurement of fluid pressure and observation of particle motion.

5. Results and discussion

5.1. Validation of simulation model

In order to validate our proposed model, the calculated results were compared with the experimental ones. Previous researches [1, 2] validated their proposed simulation models by comparing the calculated fluid pressures in grinding processes with the experimental one. In this study, the calculated fluid pressure in the grinding chamber was compared with the experimentally measured one. The time averaged fluid pressure as a function of the rotating speed of the rotor is shown in Fig. 2.1.4. The location of measurement sensor of fluid pressure in the experiment was the same as that in the numerical simulation. Seen from Fig. 2.1.4, the calculated results showed good agreement with the experimental ones. This implies that validity of the simulation model was quantitatively confirmed. The fluid pressure slightly increased with an increase in the rotating speed, because the fluid was compressed by the high-speed moving hammers at circumference of the grinding chamber.

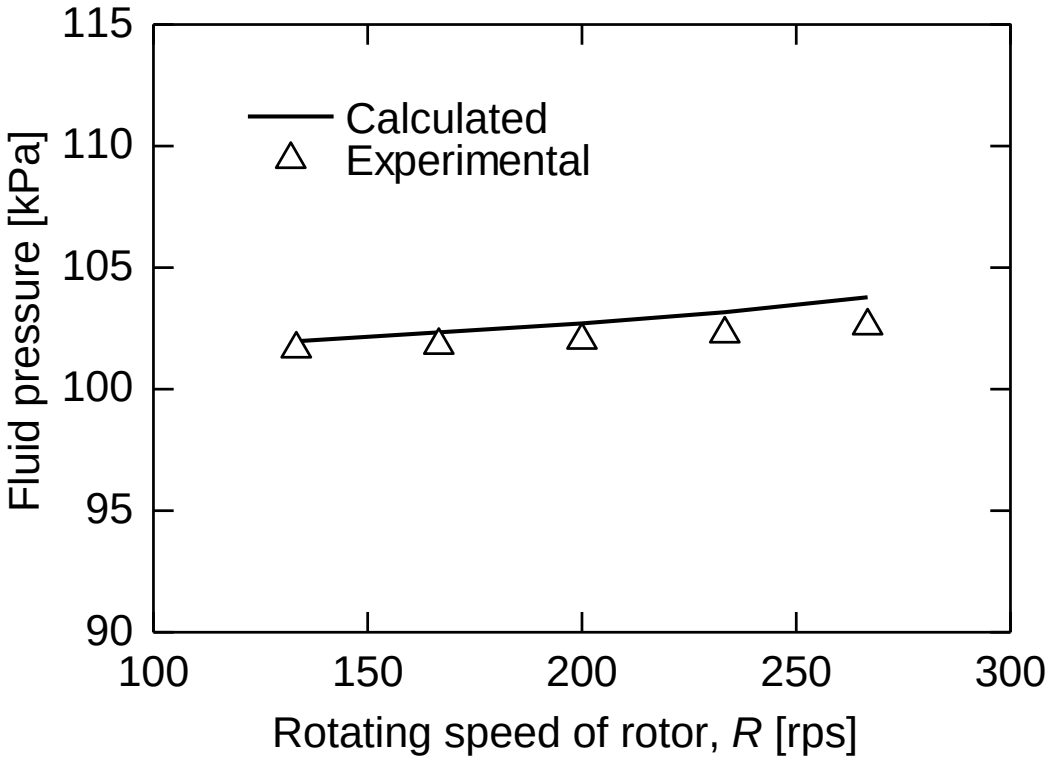

Fig. 2.1.4. Comparison of calculated fluid pressure and experimental fluid pressure in dry impact pulverizer.

5.2. Fluid pressure in grinding chamber

Fig. 2.1.5 shows calculated static fluid pressure distribution in the grinding chamber at a cross section of the rotational axis. The data was obtained after the outlet mass flow rate of the fluid from the exhaust reached almost constant. The fluid pressure at circumference of the grinding chamber was higher than in other areas. Especially, the fluid pressure in the concaves of the stator when the hammer tips approached to the concave were extremely high. This meant that the fluid in the concaves was strongly compressed by the hammers. By contrast, the fluid pressure near the center of the grinding chamber was lower than the standard atmospheric pressure (101.3 kPa). This negative pressure caused the intake flow into the grinding chamber. The radial gradient of fluid pressure from center to circumference of the grinding chamber was formed by centrifugal force generated by the fluid rotational motion. Fig. 2.1.6 indicates distributions of the static fluid pressure at the top of grinding chamber under various rotating speeds, R. At higher rotating speeds, the fluid was more compressed. Variation of the fluid pressure in the concaves generated when the hammer tips passed over the concave also increased with an increase in the rotating speed.

5.3. Fluid velocity in grinding chamber

Fig. 2.1.7 shows a calculated fluid velocity distribution in the grinding chamber at the rotating speed of 267 rps. The fluid in the grinding chamber mainly swirled around the rotational axis of the rotor. The fluid velocity at the circumference of the grinding chamber was higher than that in other areas. This was because that the fluid in front of the hammers was strongly compressed by high-speed motion of the hammers. The fluid velocity and flow pattern in concaves of the stator greatly differed from those in other area. In the concaves, the fluid velocity was much lower than the tip speed of the hammers. The swirling flows inside the concaves were generated by passing of the high-speed hammers over the concaves.

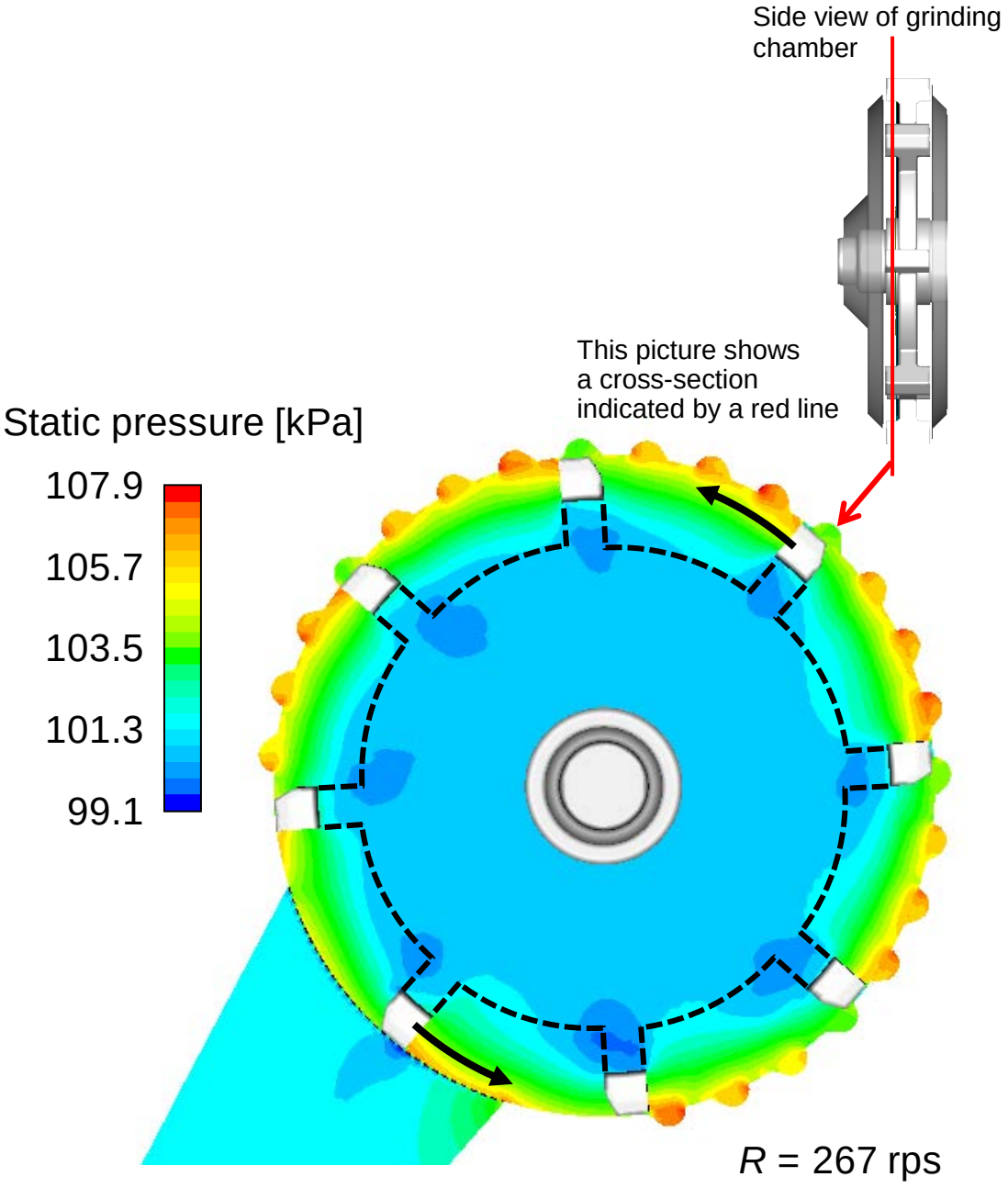

Fig. 2.1.5. Pressure distribution in grinding chamber.

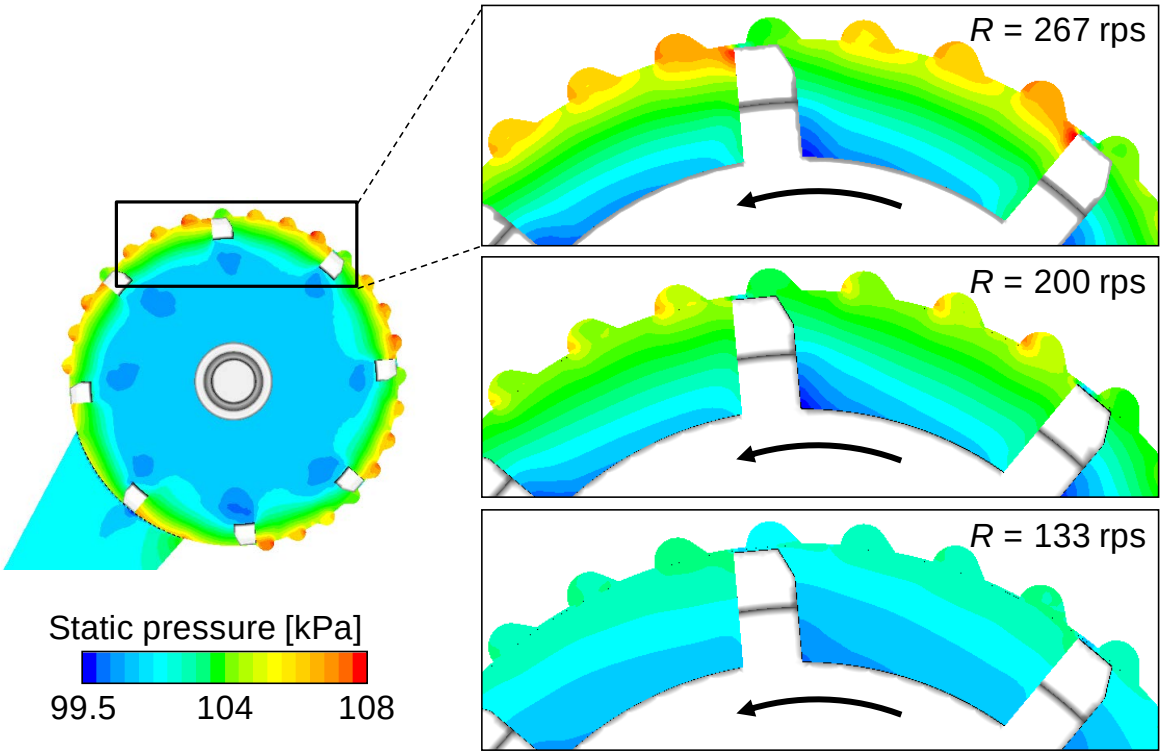

Fig. 2.1.6. Fluid pressure distributions at top of grinding chamber in various rotating speeds.

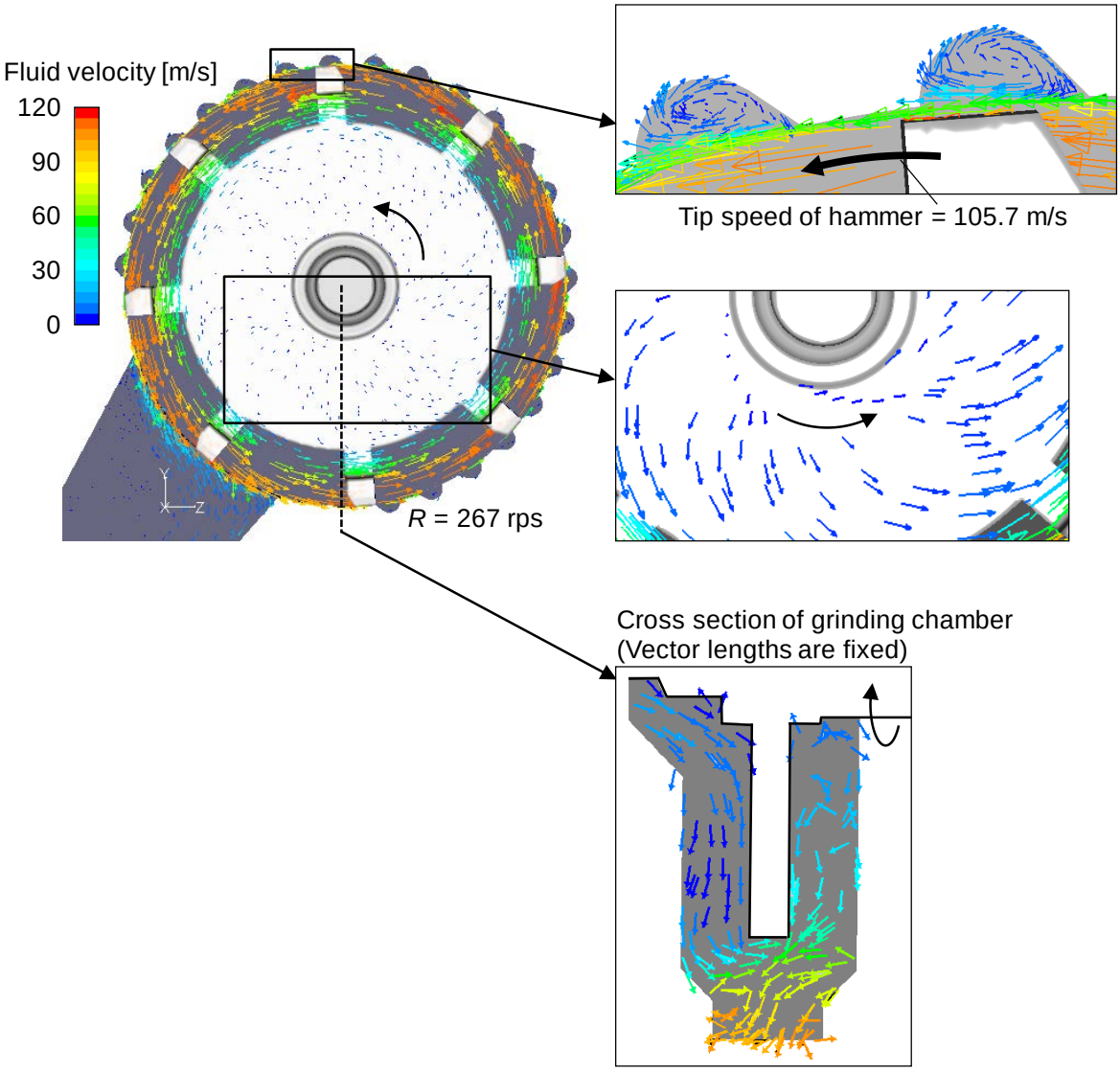

Fig. 2.1.7. Fluid velocity distribution in grinding chamber.

5.4. Particle behavior in grinding chamber

Fig. 2.1.8 indicates a calculated result of individual particle motion in the grinding chamber. Particles were continuously fed into the chamber with the rotor rotating. In the Fig. 2.1.8, particles are colored according to its velocity, and the size of the particle is enlarged by 3 times in order to clearly visualize. The particles were initially transported from center to circumference of the grinding chamber, and then accelerated by the fluid drag force, caused by the rotating hammers. The particles mostly existed at the circumference because of the centrifugal force acting on the particles. The residence time of the particles in the grinding chamber was about 0.03 s, calculated from the numerical simulation. The solid volume ratio, which was calculated from the particle phase volume divided by the continuous phase volume, was less than 3.4%. Therefore, it was reasonable that the solid flow was regarded as a dilute phase.

Fig. 2.1.9 describes a typical particle motion in a concave of the stator when a hammer passed over the concave. Distributions of the fluid pressure and fluid velocity are also indicated in the background. Time interval between snapshots was 33.3 μs. It should be noted that particles in front of the hammer were accelerated only by the fluid drag force but not by the impact with the hammer (Fig. 2.1.9a). The particles then moved into a concave of the stator with a velocity higher than the tip speed of hammers (Fig. 2.1.9b). The particles impacted with the inner wall of the concave (Fig. 2.1.9c), and then the particles rebounded (Fig. 2.1.9d). The fluid pressure in the vicinity of the impact location by the particles was remarkably compressed. Fig. 2.1.10 shows the actual particle motion in a concave recorded by the high-speed video camera. The time interval of the recording was 40 μs. The particle motion in the concave was similar to the calculated ones. The impact location of the recorded particle on the inner wall of the concave was very similar to the calculated results. And, the actual particle velocity obtained from the experimental results was 41.7 m/s at a rotating speed of the rotor, 133 rps. The particle velocity in the calculated results at the same rotating speed was from 40 to 70 m/s. This indicated that the particle velocity in the experimental results was in good agreement with the calculated one. From these results, it was found that the particles were accelerated only by the fluid drag force without the contact with the hammer and then particles impact with a wall of the stator.

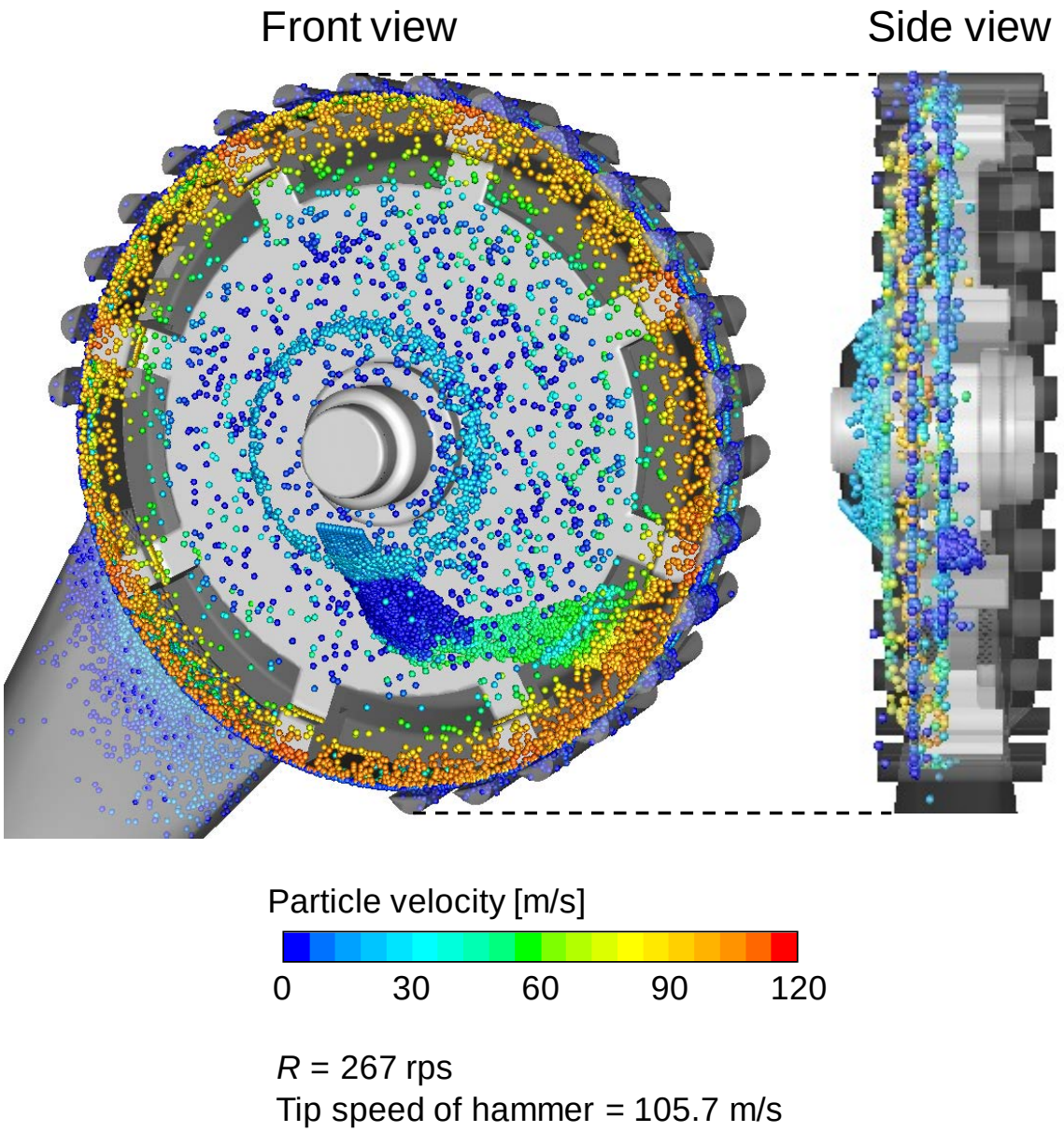

Fig. 2.1.8. Calculated result of particle behavior in grinding chamber (Size of the particles is enlarged by 3 times.).

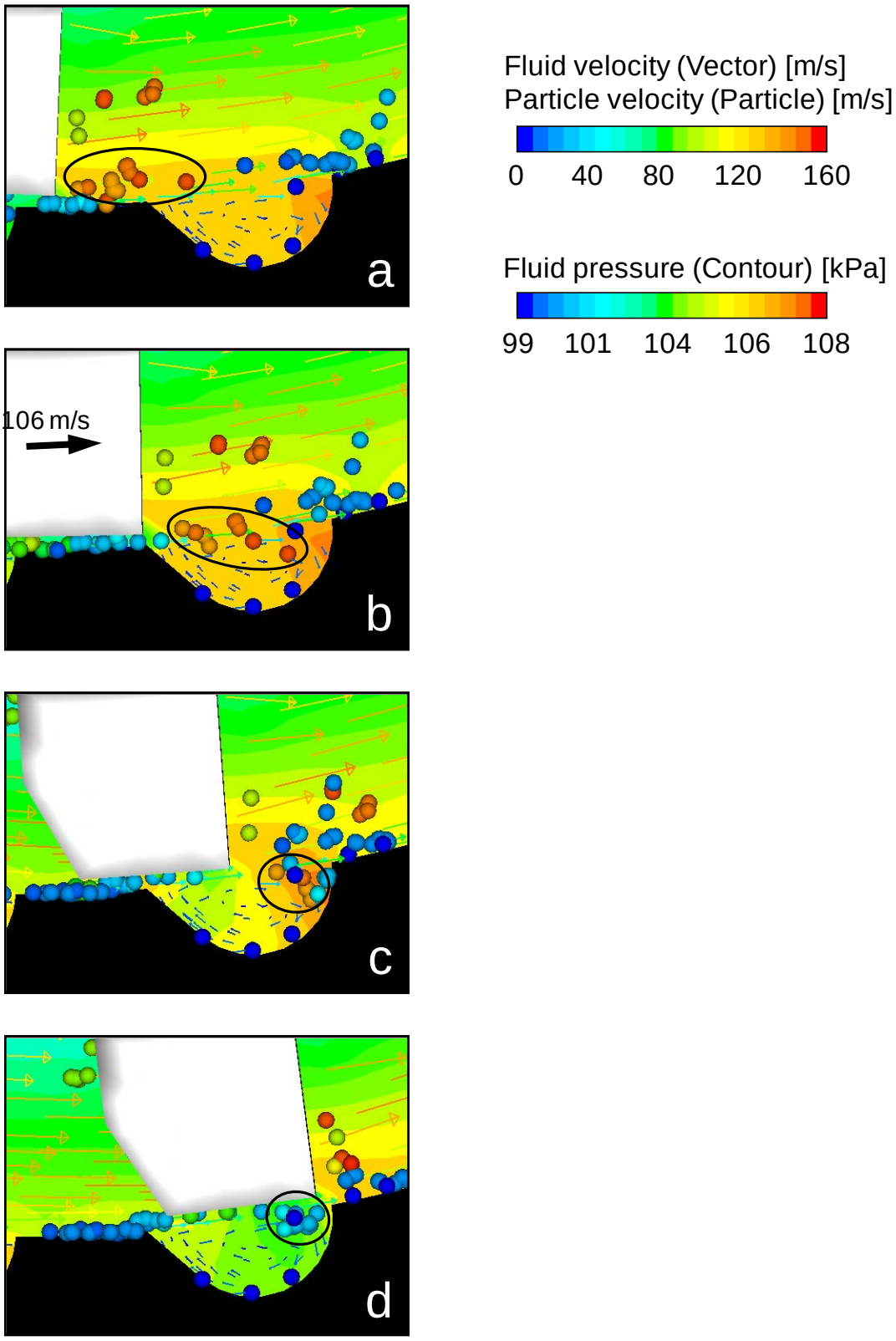

Fig. 2.1.9. Calculated results of particle behavior around hammer tip and concave of stator (R = 267 rps, Tip speed of hammer = 105.7 m/s, Size of the particles is enlarged by 3 times.).

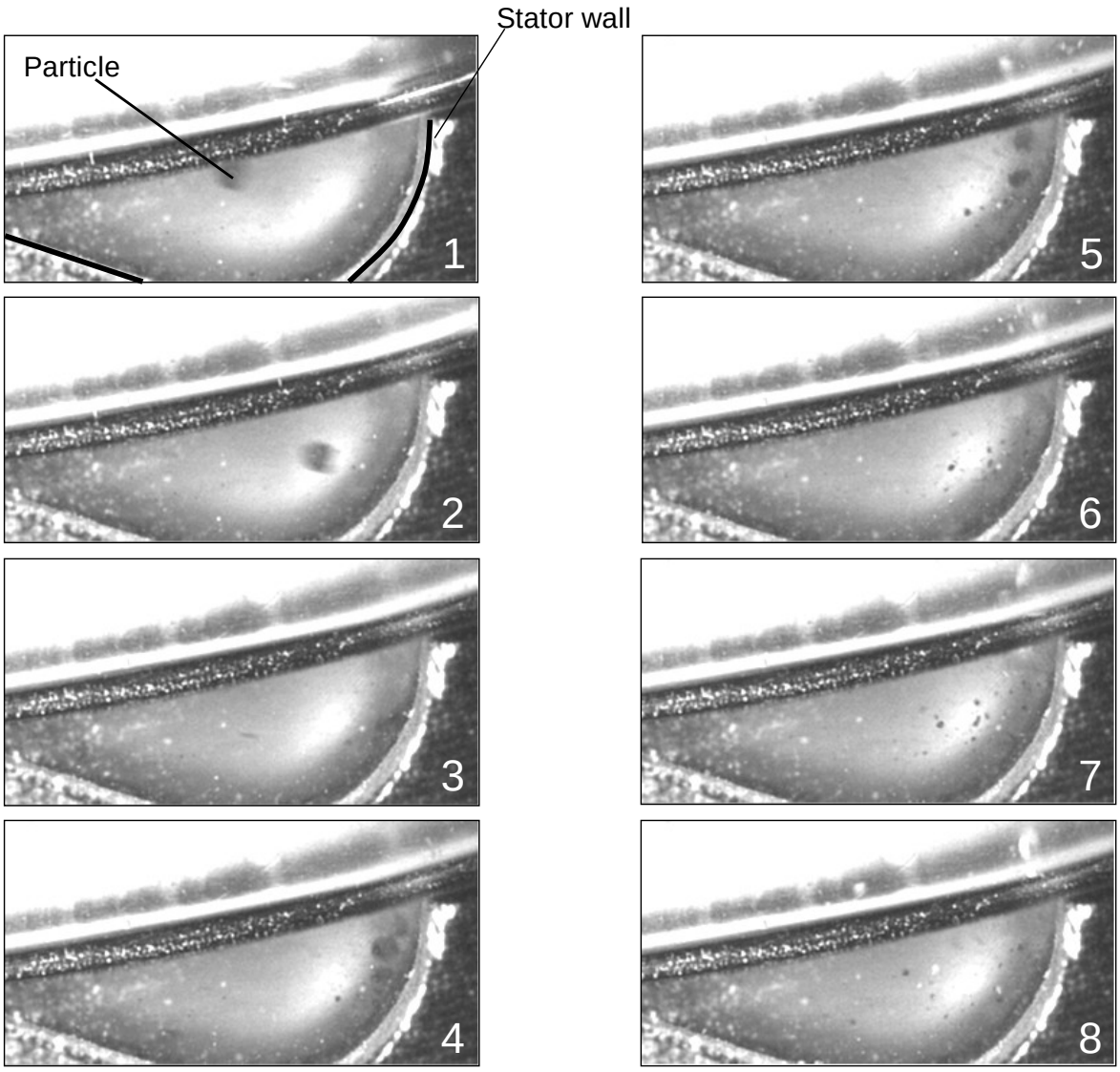

Fig. 2.1.10. Experimentally observed impact behavior of a particle (R = 133 rps).

5.5. Effects of operating parameters on velocity and frequency of particle impact

The rotating speed and the particle size of starting materials are the critical operating parameters in the impact pulverizers [3]. Thus, the velocities and frequencies of particle impact against the entire wall of the grinding chamber were numerically analyzed in detail at various rotating speeds and particle sizes. Especially, the particle impact against the two kinds of walls: (i) inner walls of concaves of the stator and (ii) front walls of hammers were investigated, as shown in Fig. 2.1.11. Number of the particles was set as 4000 in this investigation. In order to obtain the accurate calculation results, the data of the particle impact was sampled out after the calculation in the computing time longer than the particle residence time.

Fig. 2.1.11 shows velocity distributions of the particle impact against the entire walls, stator walls, and rotor walls at the different rotating speeds. The particle diameter was 250 μm. The vertical axis and horizontal axis indicates the number of particle-to-wall impacts per second and the impact velocity of particle-to-wall in the normal direction, respectively. The impact velocities less than 5 m/s were not shown in Fig. 2.1.11, because the impacts with such low impact velocity could not contribute to the grinding of particles. The results indicated that velocity distributions of the particle impact were bimodal at any rotor speeds. The maximum impact velocities of the particle in any rotor speeds were higher than the tip speed of hammers by 1.4 times. The maximum impact velocity and a width of the distribution increased with an increase in the rotor speed. Grand and Kalman [4] reported in their experimental results that the size of ground particles decreased and width of the particle size distribution of the ground particles became broader under higher rotor speeds. Therefore, the calculated results reflected characteristics of the experimental ground products. The bimodal velocity distributions of the particle impact in the impact pulverizer were classified into the two-types, i.e., high-speed impact and low-speed impact. In the region of high-speed impact, most of the particles were accelerated by the hammer and impacted against the stator. The number of particle impacts against the hammers was very small as compared to the one with the entire wall of the grinding chamber. Therefore, the particle impact at a velocity higher than the tip speed of hammers mainly occurred on the stator wall. This implied that the particles were mostly broken by the impact against the stator wall.

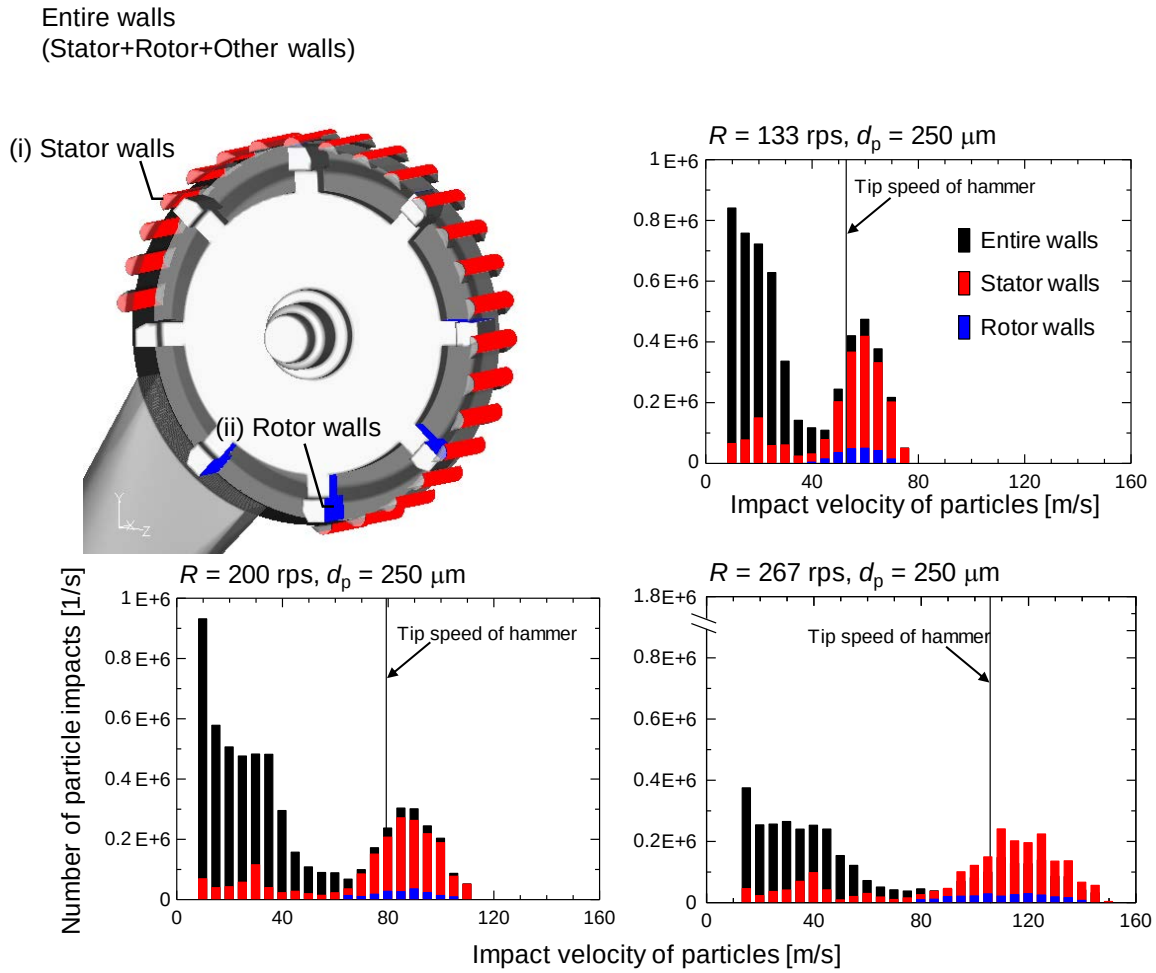

Fig. 2.1.11. Velocity distributions of particle impact against inner walls of grinding chamber.

Fig. 2.1.12 shows number fraction of particle-to-stator impacts in different particle sizes. The rotating speed of the rotor was 267 rps. The sizes of particles used were 25, 50, 100, and 250 μm. The ordinate axis indicates the number fraction of the particle-to-stator impact against all impacts with the entire wall. The fraction of low-speed impact (lower than 70 m/s) was almost the same regardless of the particle size. However, the fraction of particle-to-stator impact at a velocity faster than the tip speed of hammers (105.7 m/s) was decreased in smaller particle sizes. Generally, a smaller particle moving along with a streamline of fluid flow is more difficult to deviate from the streamline, because an inertial force of a particle decreases with a decrease in size of the particle. The calculated results showed that the number fraction of particles, which were deviated from the swirling main streamline in the grinding chamber and moved into the concaves, decreases when the particle size was smaller.

Fig. 2.1.13 shows temporal changes in particle velocity before the particle impact against the stator wall under various particle sizes. The particles in red circles of snapshots from I to IV correspond to I to IV in the below graph. The graph indicates the number averaged particle velocity before the particle impact against the stator wall at a velocity higher than 70 m/s. In the 250 μm, the particle velocity began to increase at 0.017 m, because the particles were accelerated by the fluid drag force when a hammer approached the particles. The particle velocity then began to slightly decrease from 0.007 m at which particles moved into a concave of the stator. This was because that the particles having high-speed velocities were subjected to the fluid resistance force in the concave in which the fluid velocity is very low. The fluid resistance force led to decrease of the particle velocity. The particle velocity in the concaves more decreased when the particle size was smaller. Generally, the fluid resistance force acting on a single sphere increases with the square of the particle size as indicated from Eq. (2.1.23). By constant, an inertia force of the particle is proportional to the particle mass, which is the cube of the particle size. Therefore, the velocity of particle impact against the stator wall decreased with a decrease in the particle size.

These calculated results showed that the frequency and velocity of the particle impacted against the stator wall decreased with a decrease in the size of the particles. This implied that the ground limitations existed because of the decrease of the

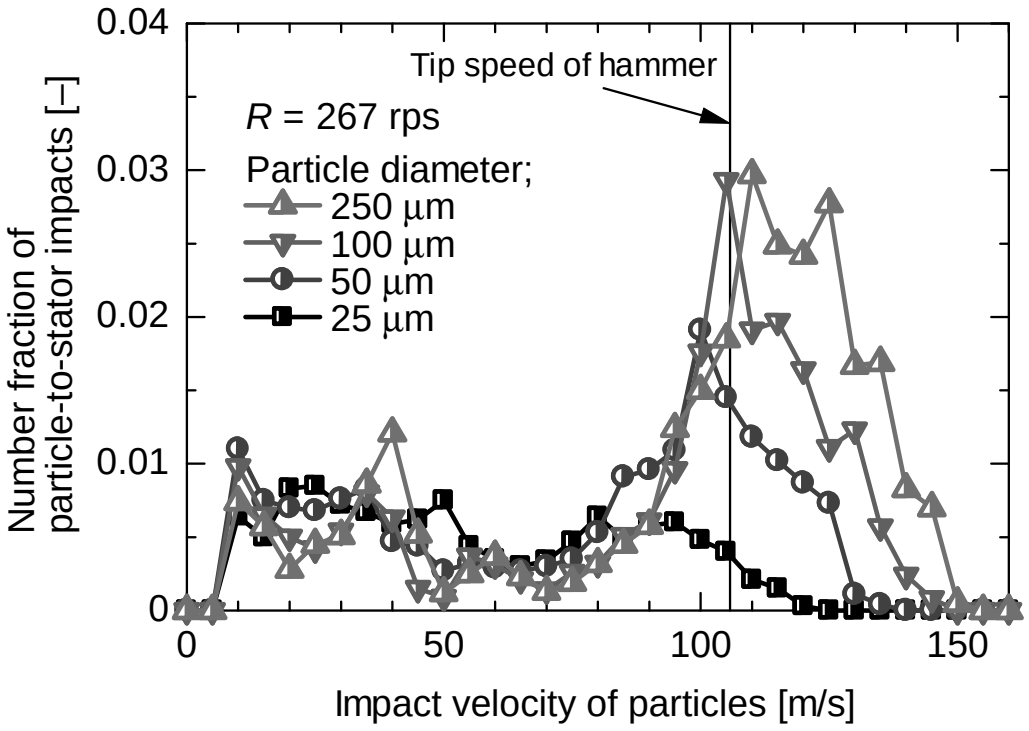

Fig. 2.1.12. Number fraction of particle-to-stator wall impacts in different particle diameter.

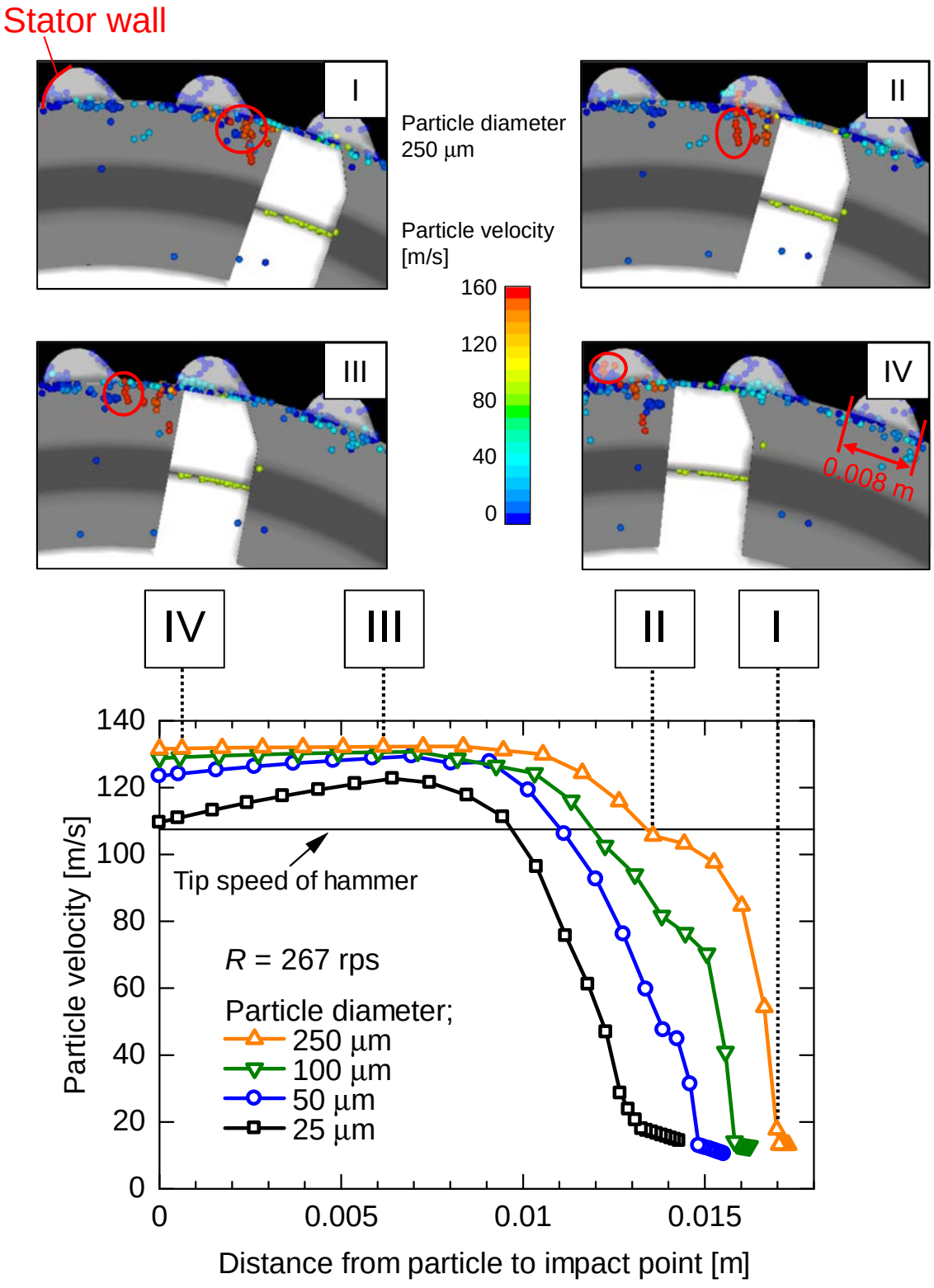

Fig. 2.1.13. Temporal changes in particle velocity before particle impact under various particle sizes. Particles in red circles of snapshots correspond to I to IV (Size of the particles is enlarged by 3 times).

frequency and velocity of particle impact when the particle size was smaller. It was concluded that the fluid flow was important factor for the velocity and frequency of particle impact, which determined performance of the impact pulverizers.

6. Conclusions

The fluid flow and individual particle motion in an impact pulverizer were numerically analyzed using a CFD-DPM coupling model. First of all, calculated fluid pressure and particle motion in the grinding chamber was compared with the experimental ones, and both results showed good agreement. It was found that the fluid in the grinding chamber mainly swirled in the direction of hammer rotation, and the fluid velocity in front of the hammers was higher than the tip speed of hammers. The velocities and frequencies of particle impact against the entire wall of the grinding chamber were also analyzed under various rotor speeds and particle sizes. It was shown that a maximum impact velocity of the particle increases, and a width of the impact velocity distributions become broader with an increase in the rotor speed. As the particle size was smaller, it was also found that the particle impacted against the stator wall was not likely to occur, and a decrease of the impact velocity was observed despite the same rotating speed of the rotor. The calculated results implied that the ground limitations existed because of the decrease of the frequency and velocity of particle impact when particle size was smaller. Consequently, the particle impact mechanism in an dry impact pulverizer was clarified via the numerical simulation using CFD-DPM coupling model.

Nomenclature

a_w	: Empirical parameter in Eq. (2.1.18)	[–]
C_1	: Coefficient of ε generation term in Eq. (2.1.11)	[–]
C_2	: Coefficient of ε dispersion term in Eq. (2.1.11)	[–]
C_d	: Coefficient of fluid drag	[–]
C_p	: Heat capacity at constant pressure	[J/(kg·K)]
C_μ	: Coefficient of eddy viscosity in Eq. (2.1.8)	[–]

d_p	: Particle diameter	[m]
e_n	: Reflection coefficient in normal direction	[–]
e_t	: Reflection coefficient in tangential direction	[–]
F_d	: Drag force coefficient	[1/s]
G_b	: Generation term of k due to buoyancy	[kg/(m·s^3)]
G_k	: Generation term of k due to average fluid velocity gradient	[kg/(m·s^3)]
$\boldsymbol{g}$	: Gravity acceleration	[m/s^2]
K_1	: Constant in Eq. (2.1.25)	[–]
K_2	: Constant in Eq. (2.1.25)	[–]
K_3	: Constant in Eq. (2.1.25)	[–]
k	: Turbulent kinetic energy	[m^2/s^2]
k_P	: Turbulent kinetic energy at node P	[m^2/s^2]
k_{therm}	: Thermal conductivity	[W/(m·K)]
M_w	: Molar mass of fluid	[kg/mol]
m_p	: Mass of particle	[kg]
$\mathrm{Pr_t}$	: Prandtl number of turbulent	[–]
p	: Fluid pressure	[Pa]
$\overline{p}$	: Average fluid pressure	[Pa]
p_0	: Standard fluid pressure	[Pa]
R	: Rotating speed of rotor	[rps]
R_m	: Molar gas constant	[J/(mol·K)]
$\mathrm{Re_p}$	: Reynolds number of particle	[–]
S	: Modulus of mean rate-of-strain tensor	[1/s]
T	: Fluid temperature	[K]
$\overline{T}$	: Average fluid temperature	[K]
T'	: Fluctuant fluid temperature	[K]
t	: Time	[s]
Δt	: Time step	[s]
U^*	: Dimensionless fluid velocity at node P	[–]
U_P	: Average fluid velocity at node P	[m/s]
$\boldsymbol{u}$	: Fluid velocity	[m/s]

$\overline{\boldsymbol{u}}$	: Averaged fluid velocity	[m/s]
$\boldsymbol{u}'$	: Fluctuant fluid velocity	[m/s]
u_{I}	: Velocity of particle impacts against stator wall	[m/s]
u_i	: Fluid velocity to direction of i ($i = x, y, z$)	[m/s]
u_{imp}	: Impact velocity of particle to wall	[m/s]
u_{reb}	: Rebound velocity of particle from wall	[m/s]
$\boldsymbol{u}_{\mathrm{p}}$	: Particle velocity	[m/s]
W_0	: Mass of particles in grinding chamber	[kg]
x_i	: Fluid length of direction of i ($i = x, y, z$)	[m]
Y_M	: Dilatation dissipation term	[kg/(m·s^3)]
y^*	: Dimensionless distance between wall and node P	[–]
y_P	: Distance between wall and node P	[–]

Greek letters

δ	: Unit tensor	[–]
ε	: Turbulent kinetic energy dissipation rate	[m^2/s^3]
φ	: Scholar variable	[–]
$\overline{\varphi}$	: Averaged scholar variable	[–]
φ'	: Fluctuant scholar variable	[–]
κ	: von Karman constant	[–]
μ	: Fluid viscosity	[Pa·s]
μ_{t}	: Eddy viscosity	[Pa·s]
ν	: Fluid kinematic viscosity	[m^2/s]
ρ	: Fluid density	[kg/m^3]
ρ_{p}	: Particle density	[kg/m^3]
σ_k	: Turbulent Prandtl numbers for k	[–]
σ_ε	: Turbulent Prandtl numbers for ε	[–]
τ_{p}	: Particle relaxation time	[s]
τ_w	: Wall shear stress	[N/m^2]

References

1 Akiyama S, Kozawa K, Yoshida H. Effect of the blade shape on the performance of a mechanical impact mill. Kagaku Kogaku Ronbunshu (In Japanese). 2003;29:607-613.

2 Chatzilamprou IG, Youds MW, Tierney MJ, Armstrong B. Numerical investigation of a developmental pneumatically fed impact pulveriser. Appl. Math. Modell. 2006;30:1180-1195.

3 Drijgemeier R, Leschonski K. Ultra fine grinding in a two stage rotor impact mill. Int. J. Miner. Process. 1996;44-45:485-495.

4 Grand E, Kalman H. Experimental analysis of the performance of an impact mill. Adv. Powder Technol. 2002;13:233-247.

5 Haider A, Levenspiel O. Drag coefficient and terminal velocity of spherical and nonspherical particle. Powder Technol. 1989;58:63-70.

6 Hinze JO. Turbulence. New York: McGraw Hill; 1975.

7 Launder BE, Spalding DB. Lectures in Mathematical Models of Turbulence. London: Academic Press; 1972.

8 Launder BE, Spalding DB. The numerical computation of turbulent flows. Comput. Meth. Appl. Mech. Eng. 1974;3:269-289.

9 Mathur SR, Murthy JY. A pressure-based method for unstructured meshes. Numer. Heat Transfer, Part B. 1997;31:195-215.

10 Morsi SA, Alexander AJ. An investigation of particle trajectories in two-phase flow systems. J. Fluid Mech. 1972;55:193-208.

11 Patankar SV. Numerical Heat Transfer and Fluid Flow. New York: Hemisphere; 1980. p.113-134.

12 Shih TH,.W. Liou WW,. Shabbir AYZ, Zhu J. A new k-ε eddy-viscosity model for high Reynolds number turbulent flows – Model development and validation. Comput. Fluids. 1995;24:227-238.

13 Stewart RL, Bridgwater J, Zhou YC, Yu AB. Simulated and measured flow of granules in a bladed mixer – a detailed comparison. Chem. Eng. Sci. 2001;56:5457-5471.

II-2. Numerical simulation for equipment design in dry impact pulverizer

1. Introduction

Equipment geometry in the dry impact pulverizer drastically changes the grinding performance. Thus, it is important to understand the effect of the equipment geometry on the grinding performance and to optimize the geometry in order to make the desired ground products and to operate the grinding process with low power consumption. However, the optimization of the geometry has been conducted by a try-and-error method or expert's knowledge. Austin [1] calculated a power consumption of a dry impact pulverizer from the rotor geometries. It is somewhat useful for the simple geometry, but it is difficult to analyze the complex geometries in impact pulverizers used in actual industries. Recently, numerical simulation is used to analyze the effect of the geometry on the grinding performance. The correlation between the geometry in grinding processes and the fluid flow and impact energy of particle are numerically investigated [3, 4, 5, 6]. However, there is no study which investigates the correlation between mean diameter of ground products and impact energy under various geometries in dry impact pulverizer.

In this study, effect of the rotor geometry on particle impacts against stator walls in a dry impact pulverizer was numerically investigated. Calculated results were compared with the experimental results. The effects of geometries such as the number of hammers and clearance between the rotor and stator were analyzed.

2. Numerical analysis

2.1. Numerical model

Fluid flow and particle motion in the dry impact pulverizer under various rotor geometries were numerically analyzed using the CFD-DPM coupling model. Numerical model and calculation conditions were most of the same as those used in the previous section (see II-1. 3.). A particle was fed into the grinding chamber per 8.33 μs continuously. Impact velocity and impact frequency were analyzed when the number of particle in the grinding chamber was almost constant. At this time, the number of particle was 4,000. The rotating speed of the rotor was set at 267 rps.

2.2. Geometric conditions

In order to investigate the effect of equipment geometry of the rotor in dry impact pulverizer on the grinding performance, various geometries of the rotor were used as shown in Fig. 2.2.1. In this study, the number of hammers installed on the rotor, clearance between the hammer tip and stator wall were changed. The effects of the geometric conditions on the frequency and velocity of particle impact against the wall in the dry impact pulverizer were numerically analyzed. Table 2.2.1 summarizes the combination of the number of hammers and clearance used in this study.

2.3. Particle impact energy against wall

The grinding performance can be investigated using impact energy. In the dry impact pulverizer, the particle breakage is mainly caused by the impact against the stator wall. The impact energy E_{I} of particles against the stator walls was calculated from the velocity and frequency of the particle impacts against the walls per unit time. The impact energy was obtained by the following equation:

$$E_{\mathrm{I}} = \frac{\sum_{i=1}^{n} \frac{1}{2} m_{\mathrm{p},i} u_{\mathrm{I},i}{}^{2}}{t_s W_0} \tag{2.2.1}$$

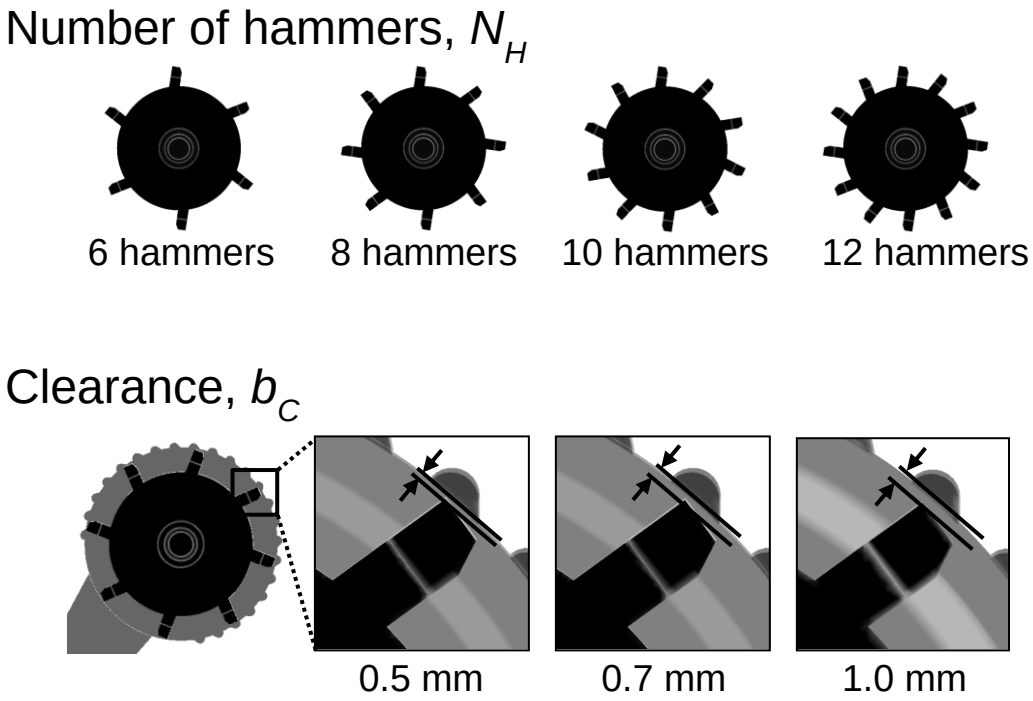

Fig. 2.2.1. Geometric conditions of simulation.

Table 2.2.1 Combination of number of hammers and clearance

Run No.	Number of hammers, N_H [–]	Clearance, b_C [mm]
1	8	0.5
2	8	0.7
3	8	1.0
4	8	0.5
5	8	0.5
7	6	0.5
8	10	0.5
9	12	0.5

where n, m_p, u_I, t_s, and W_0 are number of particle impacts against the stator walls, particle mass, velocity of particle impacting against the stator walls, simulation time, mass of the all particles in grinding chamber, respectively. E_I was calculated from the particle impacts for the time taken for one revolution of the rotor.

3. Experimental

Grinding operation was conducted using the dry impact pulverizer (see Fig. 2.1.1) in order to compare the calculated results with experimental ones. In the grinding operation, the effects of the number of hammers and clearance on the median diameter of ground products were experimentally analyzed. Geometry of the rotor used in this experiment is shown in Fig. 2.2.2. A lactose hydride powder (Pharmatose 80M, DMV International, d_{50} = 254 μm), which is a common pharmaceutical excipient, was used as starting material. The median diameter of the lactose was 254 μm. Grinding conditions were similar to the calculated ones. The feed rate of the starting material was 30 g/min. In this case, the particle residence time in the grinding chamber was less than a few second. The total operating time was 5 min. The median diameter of the ground products were measured by a laser diffraction particle size analyzer (SALD-2100, Shimadzu Co., Ltd.).

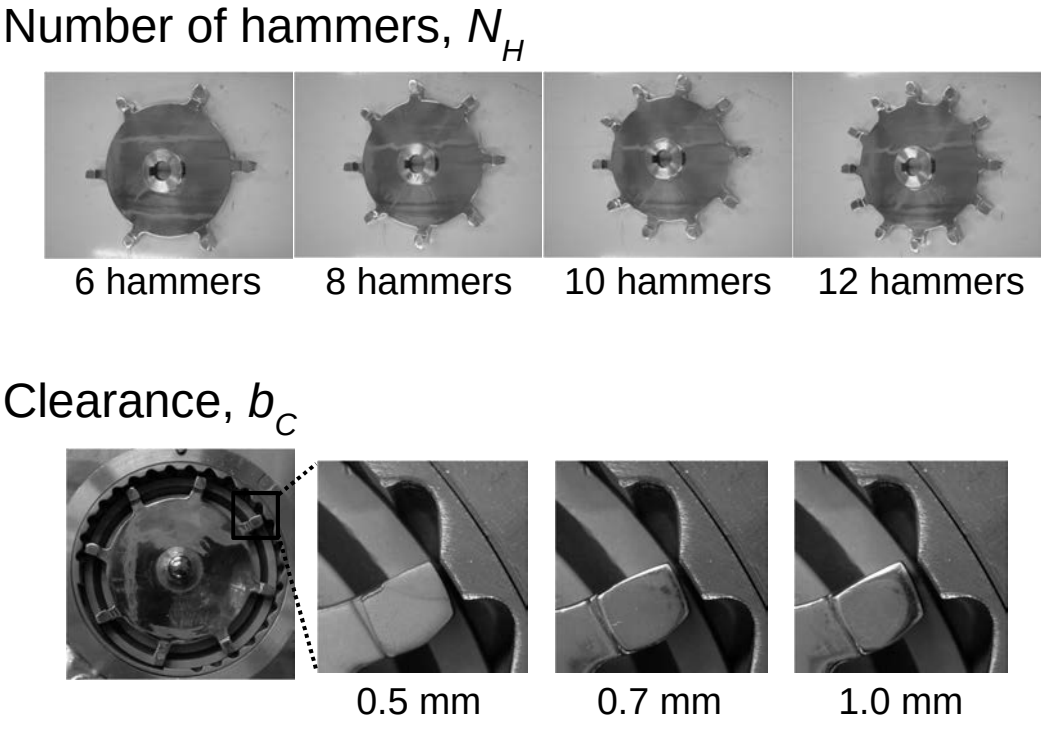

Fig. 2.2.2. Geometric conditions of experimant.

4. Results and discussion

4.1. Effect of number of hammers on grinding performance

Fig. 2.2.3 shows velocity distribution of fluid flow in the dry impact pulverizer under various numbers of hammers. The clearance was 0.5 mm. When the rotor with 6 hammers was used, the fluid only near the hammers in the circumference of the grinding chamber moved at a speed higher than 100 m/s. On the other hand, when the rotor with more than 8 hammers was used, the fluid uniformly moved in the circumference at a speed higher than 100 m/s. Fig. 2.2.4 indicates velocity distribution of particle impact against stator walls of grinding chamber under various numbers of hammers. The stator walls were shown in Fig. 2.1.11. The velocity distributions showed bimodal distributions. This was because the velocity more than 60 m/s indicated the impact of the particles took place at the concave of stator by high-speed moving hammer. On the other hand, the velocity less than 60 m/s showed the impact of the particles suspended inside the concave. With an increase in the number of hammers at a range from 6 to 12, impact frequency at a range of impact velocity from 120 to 150 m/s was increased because the fluid velocity in the circumference of the grinding chamber increased as shown in Fig. 2.2.3.

Fig. 2.2.5 describes number of particle impacts against the stator wall per unit time as a function of number of hammers. The number of particle impact significantly increased with an increase in the number of hammers from 6 to 8. When the number of hammers increased to more than 8, the number of particle impact gently increased. This was because that the fluid velocity in the circumferences of the grinding chamber increased with an increase in the number of hammers. Therefore, it was found that the fluid velocity distribution in the grinding chamber was determined by the number of hammer and strongly affected the particle impact conditions.

Fig. 2.2.6 shows correlation between the number of hammers and impact energy. The impact energy increased with an increase in the number of hammers from 6 to 8. This is because of the increase in the frequency and velocity of the particle impacts. The impact energy then increased again with an increase in the number of hammers from 10 to 12 because of the increase in the impact velocity.

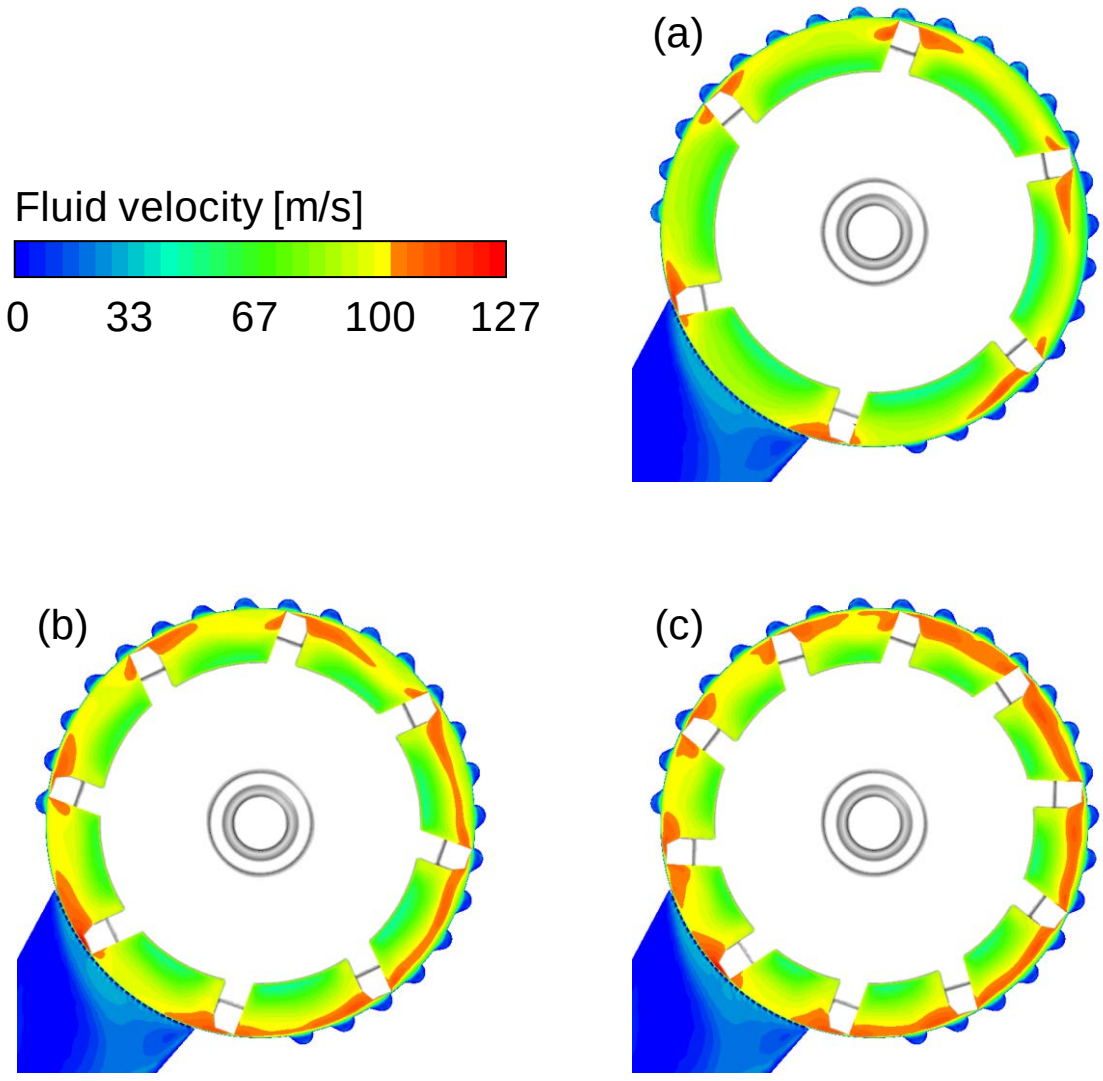

Fig. 2.2.3. Velocity distributions of fluid in impact pulverizer under various numbers of hammers; (a) 6 hammers, (b) 8 hammers, (c) 10 hammers.

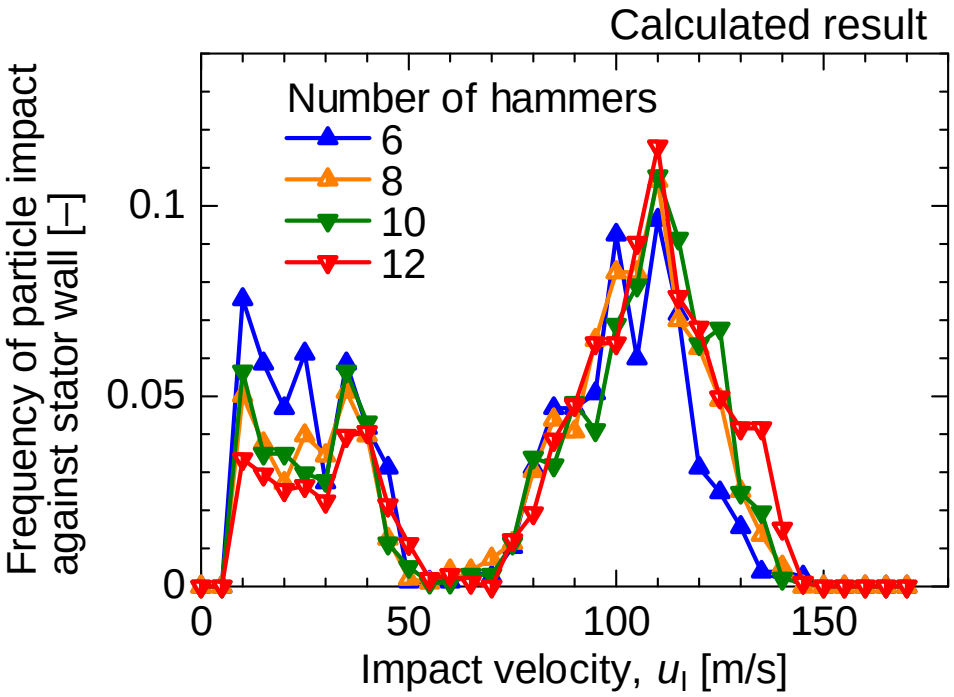

Fig. 2.2.4. Velocity distribution of particle impacts against stator walls of grinding chamber under various numbers of hammers.

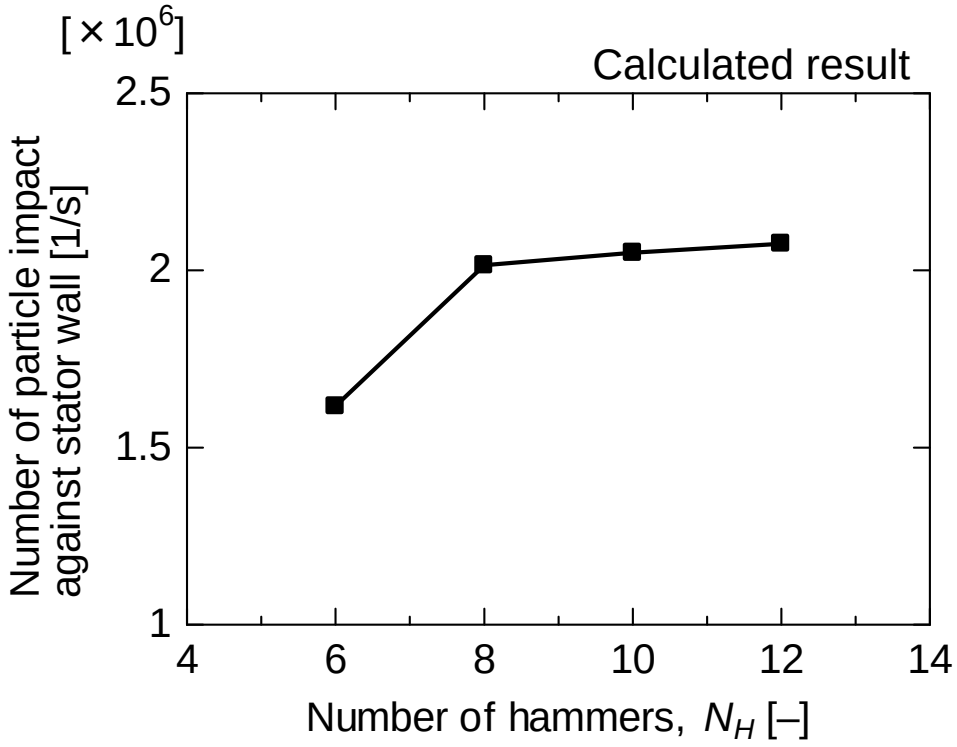

Fig. 2.2.5. Effect of number of hammers on number of particle impacts against stator wall.

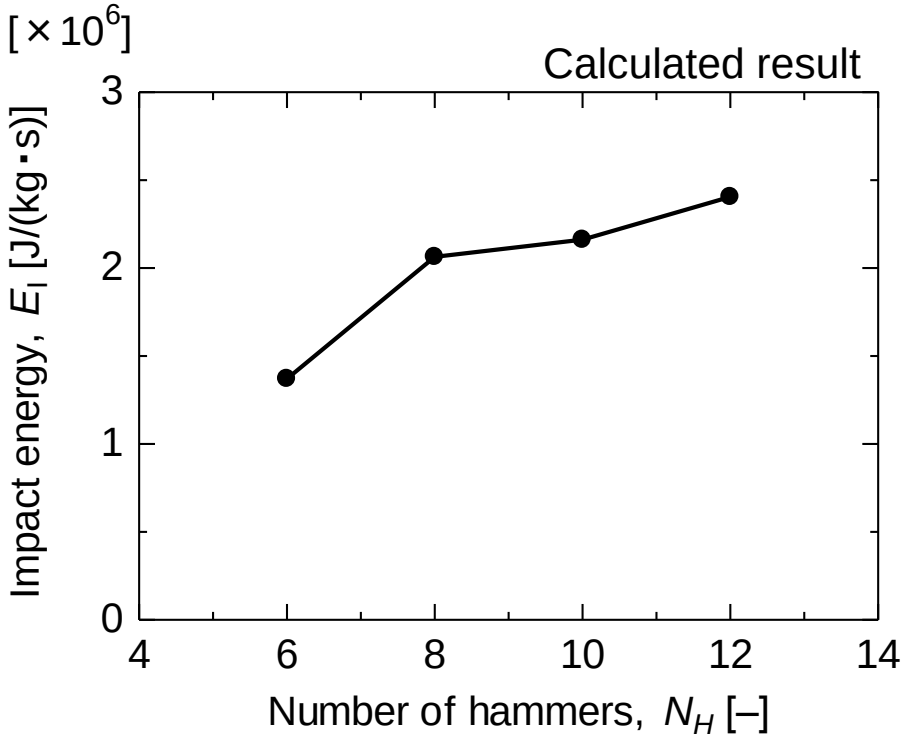

Fig. 2.2.6. Impact energy between particle and stator wall as a function of number of hammers.

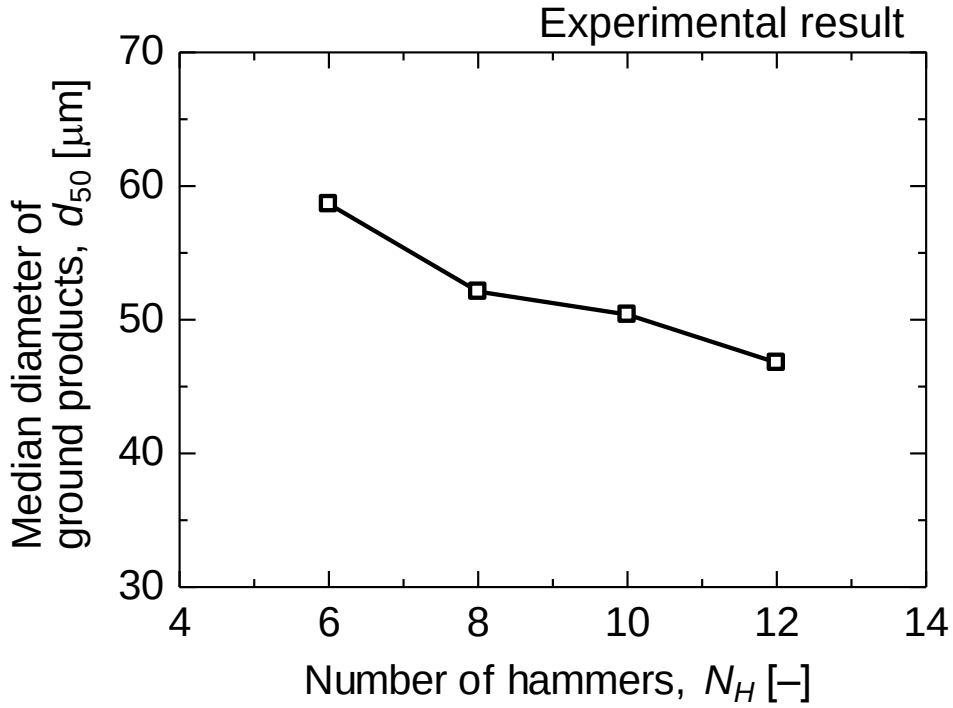

Fig. 2.2.7. Effect of number of hammers on median diameter of ground products.

Fig. 2.2.7 indicates correlation between the number of hammers and median diameter of ground products obtained from the experiment. The median diameter decreased with an increase in the number of hammers. This experimental result showed the same tendency as the calculated results of the impact energy.

4.2. Effect of clearance on grinding performance

Fig. 2.2.8 shows velocity distribution of fluid flow around a hammer under various clearances. The number of hammers was 8. The fluid velocity around a hammer slightly increased with a decrease in the clearance. This was because that the fluid was pressed into the stator wall and the transmission efficiency of the kinematic energy of the rotor from the rotor to the fluid was improved by decreasing the clearance. Fig. 2.2.9 indicates velocity distribution of particle impact against stator walls of grinding chamber under various clearances. With a decrease in the clearance at a range from 1.0 to 0.5 mm, impact frequency at a range of impact velocity from 120 to 150 m/s was slightly increased because the fluid velocity around the hammers increased.

Fig. 2.2.10 describes number of particle impact against the stator walls per unit time as a function of clearances. The number of particle impact increased with a decrease in the clearance. This is because that by using a rotor with smaller clearance the more particles in front of hammer could impact against the stator wall when a hammer pass over a concavo of the stator.

Fig. 2.2.11 shows a correlation between the clearance and impact energy. The impact energy increased with a decrease in the clearances. Especially, the impact energy drastically increased when the clearance changed from 0.7 to 0.5 mm.

Fig. 2.2.12 indicates correlation between the clearance and median diameter of ground products obtained experimentally. The median diameter decreased with a decrease in the clearances. This experimental result showed the same tendency as the impact energy.

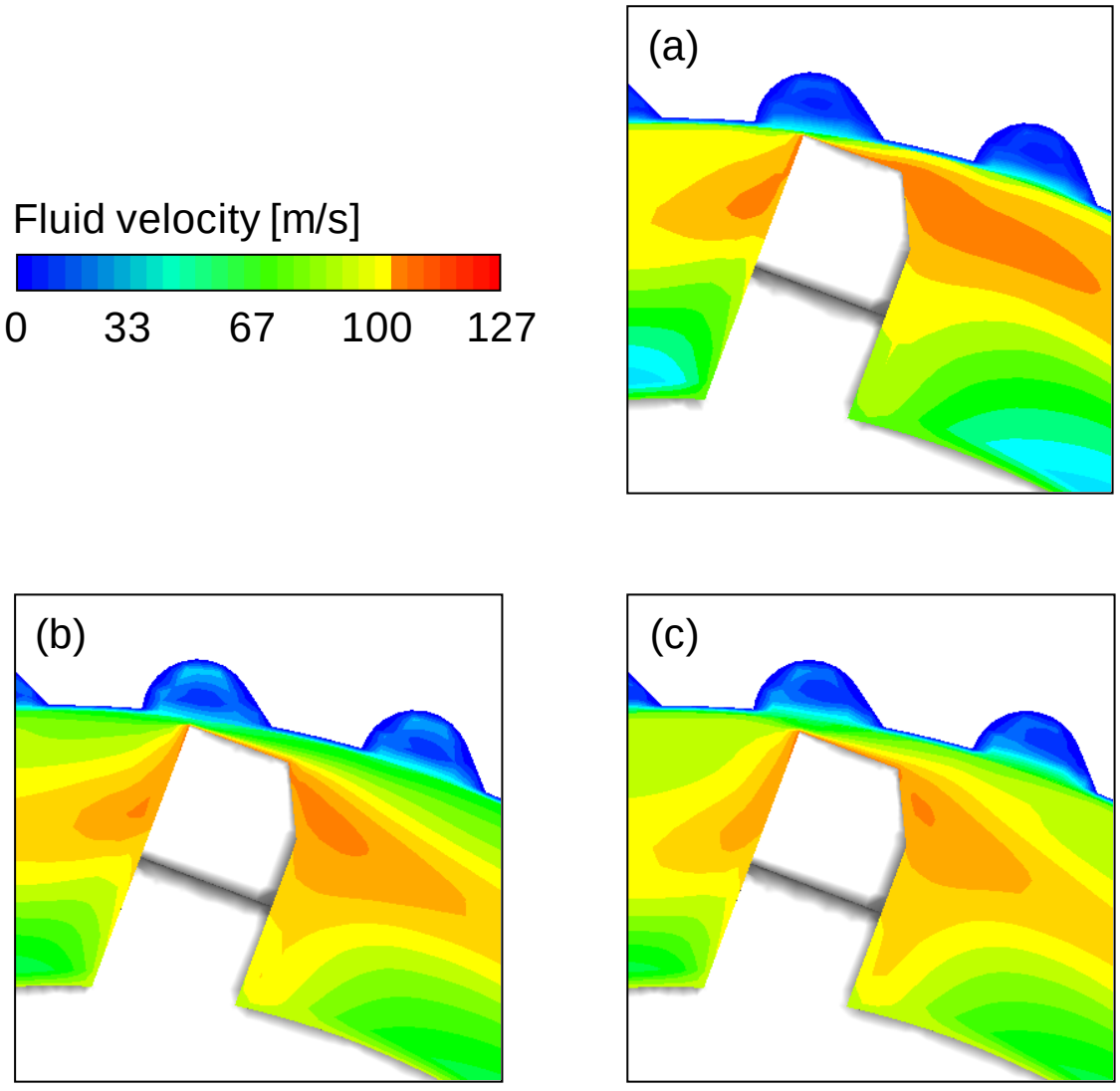

Fig. 2.2.8. Velocity distributions of fluid in vicinity of hammer tip in impact pulverizer under vairous clearances; (a) clearance = 0.5 mm, (b) clearance = 0.7 mm, (c) clearance = 1.0 mm.

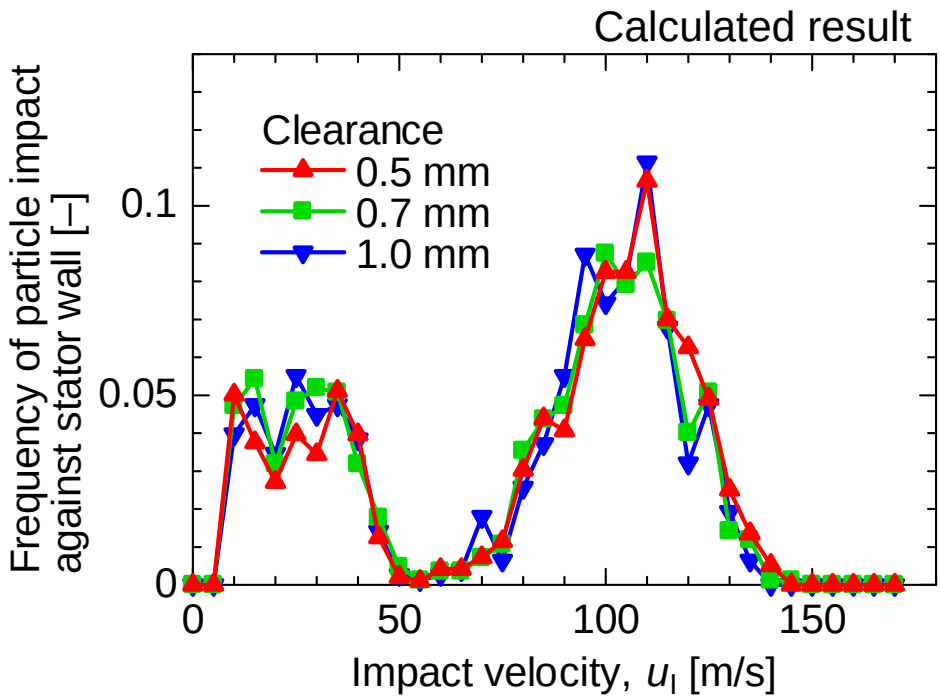

Fig. 2.2.9. Velocity distribution of particle impact against stator wall of grinding chamber under various clearances.

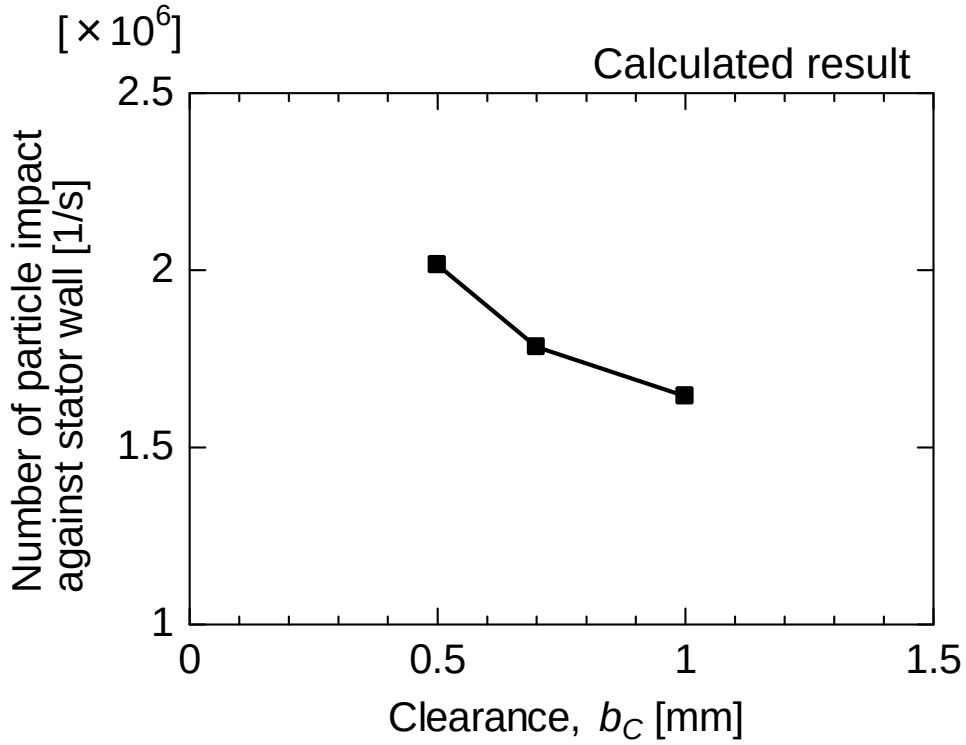

Fig. 2.2.10. Effect of clearance on number of particle impact against stator wall.

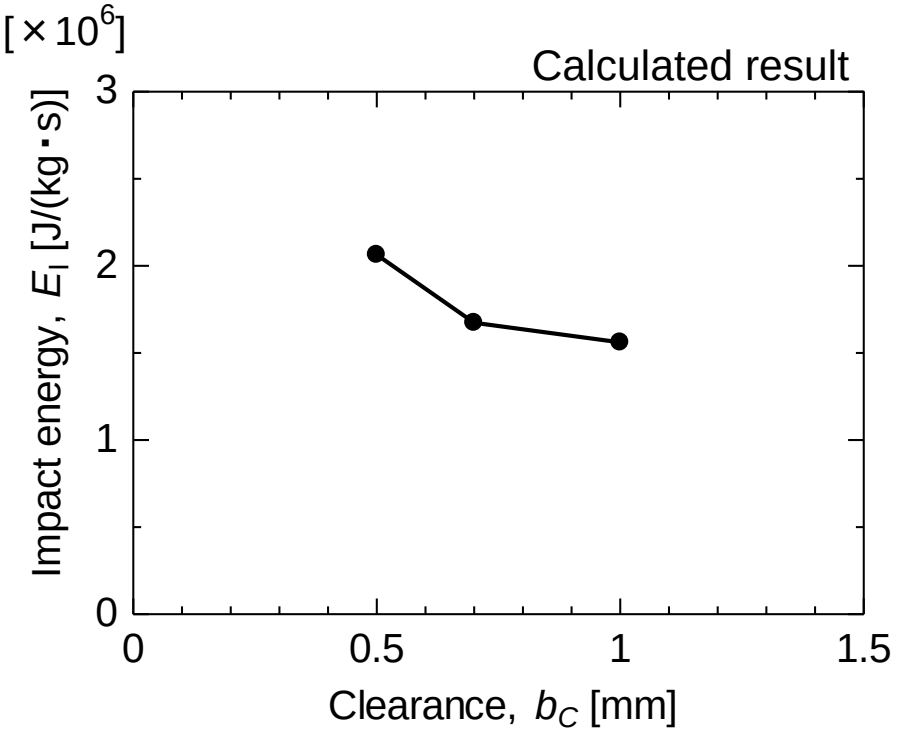

Fig. 2.2.11. Impact energy between particle and stator wall as a function of clearance.

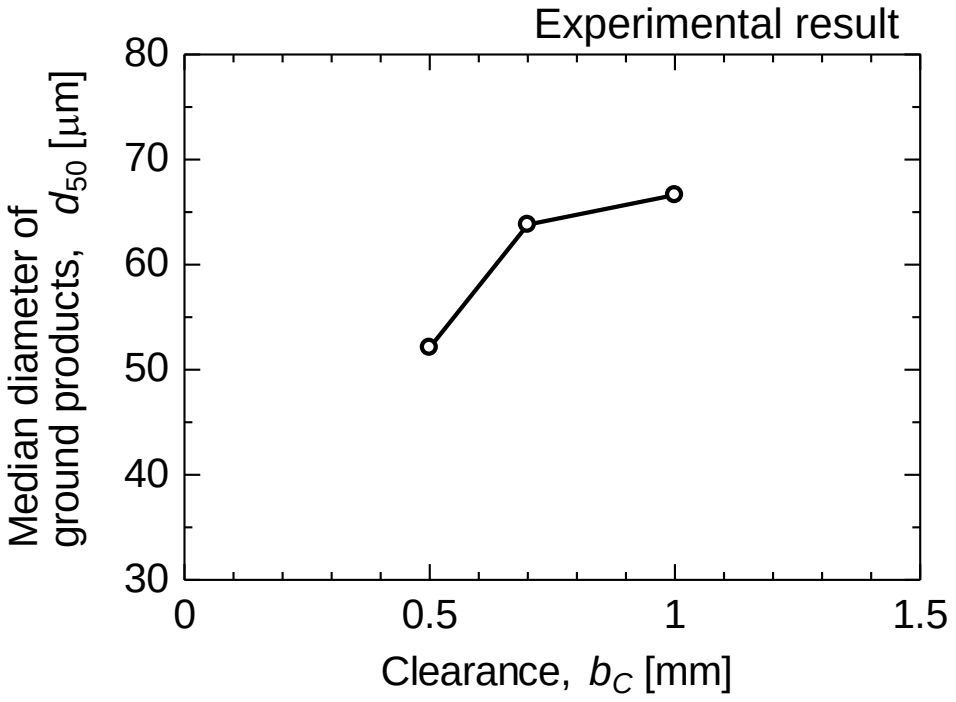

Fig. 2.2.12. Effect of clearance on median diameter of ground products.

Fig. 2.2.13 shows a correlation between the calculated impact energy and median diameter of ground products experimentally obtained under various geometries of the rotor. The median diameter decreased with an increased in the impact energy. Here, the results were fitted by the following equation based on Bond's law [2]:

$$E_{\mathrm{I}} = C_B\left(1/\sqrt{d_{50}} - 1/\sqrt{d_{f50}}\right) \tag{2.2.2}$$

where d_{f50} is median diameter of starting material powders. In this study, the d_{f50} was 254 μm. C_B is a coefficient. The coefficient is used as a fitting parameter. It was found that the correlation of the impact energy with the median diameter could be described by the Eq. (2.2.2). Only in the geometry of the rotor with 6 hammers, the median diameter obtained from the experiment was smaller than the one estimated from the Eq. (2.2.2). This was because the fluid velocity in grinding chamber using the rotor with 6 hammers was so small among other types of the rotor. Thus, the particle residence time in the grinding chamber using the rotor with 6 hammers was indicated larger residence time than the other types of the rotor. Therefore, the median diameter of ground products in the dry impact pulverizer can be predicted from the impact energy using the negative correlation based on the Bond's law.

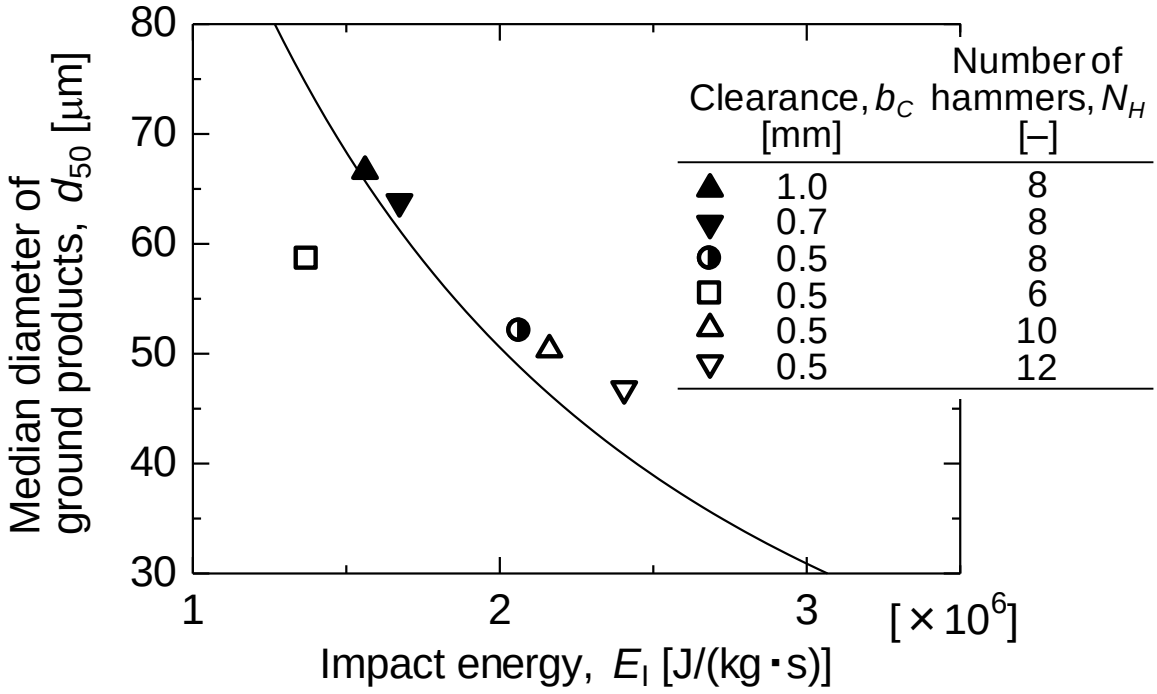

Fig. 2.2.13. Correlation between median diameter of ground products and impact energy under all conditions of rotor.

5. Conclusions

The effects of the equipment geometry of the dry impact pulverizer were numerically analyzed using a CFD-DPM coupling model. Especially, the number of hammers and clearance of the rotor were focused. The frequency and velocity of particle impact against the stator walls were analyzed under various geometries of the rotor. The fluid velocity in the grinding chamber and the number of the particle impact increased with an increase in the number of hammers. The number of the particle impact also increased with a decrease in the clearance. The impact energy showed same tendency with the experimental results. The excellent correlation based on Bond's law between the impact energy and median diameter of ground products has been obtained. The median diameter of ground products can be estimated from the impact energy using the correlation. This simulation method revealed the effects of the equipment geometry on the grinding performance. It is also expected that the simulation method can be a strong tool for the control and the optimization of equipment geometry in the dry impact pulverizer.

Nomenclature

b_C	: Clearance	[m]
C_B	: Coefficient of Eq. (2.2.2)	[J·m$^{0.5}$/(kg·s)]
d_{f50}	: Median diameter of starting materials	[m]
d_{50}	: Median diameter of final ground products	[m]
E_I	: Impact energy	[J/(kg·s)]
m_p	: Mass of particle	[kg]
n	: Number of particle impacts against stator wall	[–]
N_H	: Number of hammers	[–]
t_s	: Simulation time	[s]
u_I	: Velocity of particle impacts against stator wall	[m/s]
W_0	: Mass of all particles in grinding chamber	[kg]

References

1 Austin LG. A preliminary simulation model for fine grinding in high speed hammer. Powder Technol. 2004;143-144:240-252.

2 Bond FC. The third theory of comminution. Trans. AIME. Min. Eng. 1952;193:484-494.

3 Cleary PW, Sinnott MD, Morrison RD. DEM prediction of particle flows in grinding processes. Int. J. Numer. Methods Fluids. 2008;58:319-353.

4 Nichiura D, Wakita Y, Shimosaka A, Shirakawa Y, Hidaka J. Estimation of power during dispersion in stirred media mill by DEM–LES simulation. J. Chem. Eng. Japan. 2010;43:841-849.

5 Gudin D, Turczyn R, Mio H, Kano J, Saito F. Simulation of the movement of beads by the DEM with respect to the wet grinding process. AlChE J. 2006;52:3421-3426.

6 Jayasundara CT, Yang RY, Guo BY, Yu AB, Rubenstein J. Effect of slurry properties on particle motion in IsaMills. Miner. Eng. 2009;22:886-892.

Chapter III

Development of simulation method of particle breakage in dry impact pulverizer

1. Introduction

Particle size distribution of ground products in a grinding process is important because the particle size distribution influences very much on the quality and performance of the end products in many industries. Therefore, the particle grinding phenomenon such as particle breakage and temporal changes in the particle size distribution in the grinding process should be understood.

To understand the particle grinding phenomena in the grinding process, two main phenomena should be understood. The first phenomenon is how the particles behave in the grinding equipment and how much impact stress the particles receive. The second phenomenon is how the particles are broken and split into the smaller particles, namely fragments. The numerical simulation technique has been used for analyzing each grinding phenomena, i.e., the two phenomena have been analyzed separately. Thus, the particle grinding phenomenon in the grinding process could not be understood in detail.

In this chapter, a novel simulation method to simultaneously calculate particle motion and its breakage in a dry impact pulverizer was developed. First, a new particle breakage model consisting of particle strength, impact stress acting on the particles, and fragment size distribution after the particle breakage was proposed. A uniaxial compression test and impact breakage test were conducted in order to decide parameters of the proposed particle breakage model. The motion of particles in the dry impact pulverizer was calculated using the DPM-CFD coupling model. Then, the proposed particle breakage model was coupled with the DPM-CFD coupling model. The temporal changes in particle size distribution in the grinding chamber were analyzed. The validity of the proposed method was investigated. The size limitation of ground products in the dry impact pulverizer was also discussed. The calculated results were compared with the experimental ones under various operating conditions such as particle size of starting materials and rotating speed of the rotor.

2. Particle breakage model

2.1. Overview of the particle breakage model

In this study, the particle breakage in a grinding process was described by three components; the particle strength, the impact stress acting on the particle, and the fragment size distribution after the particle breakage.

Fig. 3.1.1 shows a schematic of a proposed particle breakage model. When a particle impacts against a wall at an impact velocity u_p, the particle receives an impact stress σ_I. If the impact stress σ_I is higher than the particle strength σ_S ($\sigma_I > \sigma_S$), the particle is broken. The particle then splits into multiple smaller fragments having different sizes of d_i (i = 1, 2, 3, ···). The breakage process will be repeated in the grinding chamber. The proposed three components are explained in detail below.

2.2. Particle strength

The particle strength is defined by Griffith's theory [3]. Schematic diagram of the Griffith's theory shows Fig. 3.1.2. The particle strength σ_S is calculated by the following equation:

$$\sigma_S = \left(\frac{2\gamma E}{\pi C} \right)^{0.5} \tag{3.1.1}$$

where γ and C express a surface energy per unit area and half-length of a crack which is an onset of a particle breakage, respectively. The particle strength has a distribution even if the size and properties are the same, because the crack length is not uniform and has its distribution. In a preliminary investigation, it was found that the particle strengths measured experimentally can be well expressed by Griffith's theory under an assumption that distribution of the crack length obeys a log-normal distribution. Therefore, the crack length C can be described by the following log-normal distribution:

$$f(C) = \frac{1}{\sqrt{2\pi} C \ln S_c} exp\left[-\frac{1}{2} \left(\frac{\ln C - \ln \mu_c}{\ln S_c} \right)^2 \right] \tag{3.1.2}$$

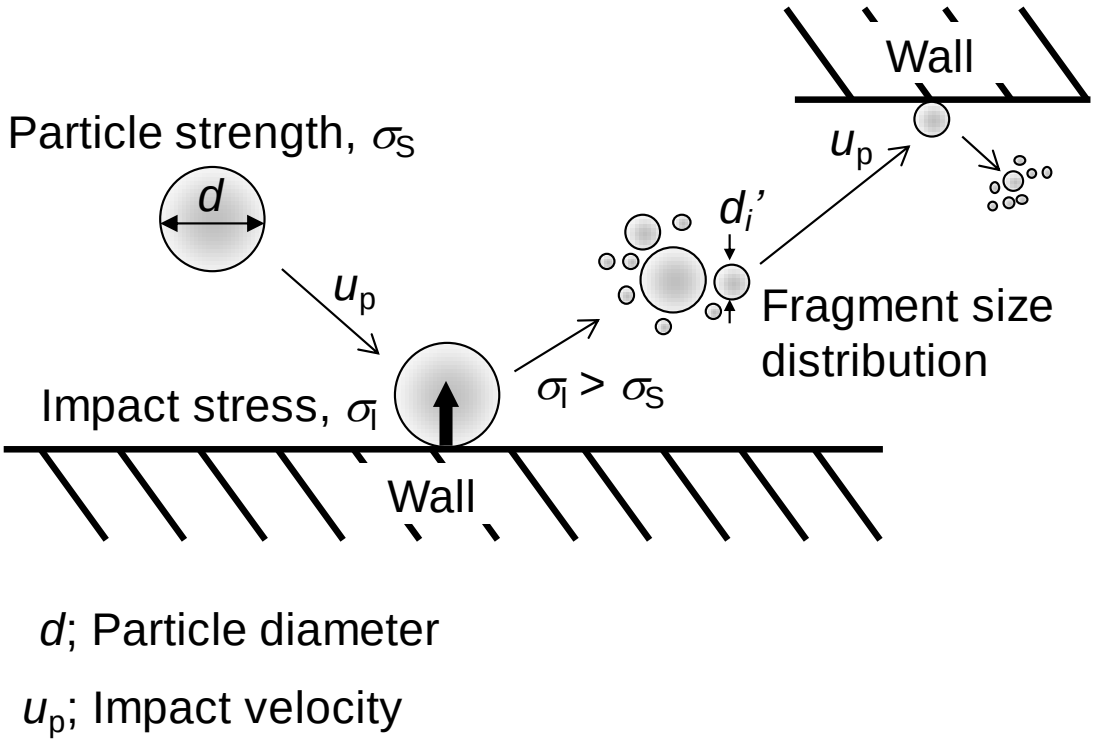

d; Particle diameter

u_p; Impact velocity

Fig. 3.1.1. Schematic of particle breakage model.

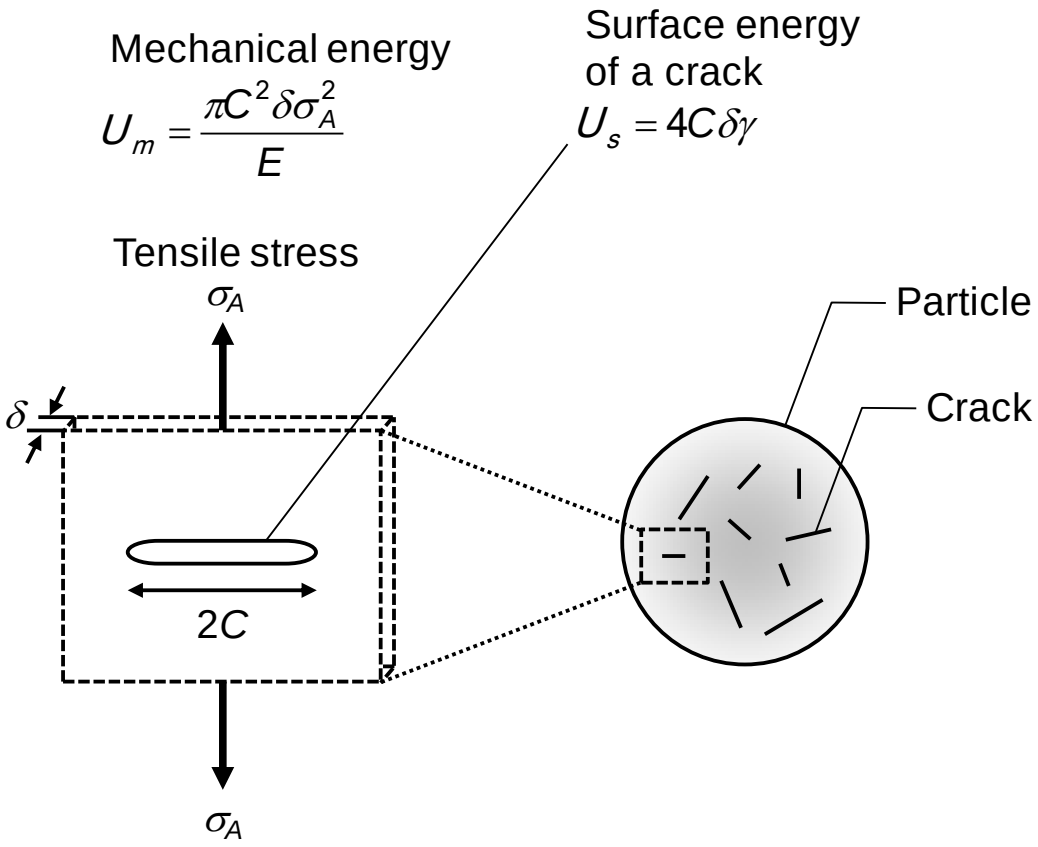

$$U = -U_m + U_s = -\frac{\pi C^2 \delta \sigma_A^2}{E} + 4C\delta\gamma$$

$$\frac{dU}{dC} = 0 \longrightarrow \text{Particle strength}$$

$$\sigma_s = \left(\frac{2\gamma E}{\pi C}\right)^{0.5}$$

Fig. 3.1.2 Schematic of Griffith theory.

where μ_c and S_c indicate mean and standard deviation of the crack length, respectively. Therefore, once the two parameters μ_c and S_c in Eq. (3.1.2) are determined, the particle strength can be calculated by using Eqs. (3.1.1) and (3.1.2).

2.3. Impact stress

When an elastic spherical particle impacts against a wall at the impact velocity u_p, maximum impact load F_I acting on the particle can be calculated by the following equation [5] derived from Hertz's theory:

$$F_I = \left(\frac{5\rho_p\pi}{3}\right)^{0.6}\left(\frac{4}{3k}\right)^{0.4}\left(\frac{d}{2}\right)^2 u_p^{1.2} \tag{3.1.3}$$

where ρ_p and d describe particle density and particle diameter, respectively. k is the material mechanical property which is defined by the following equation:

$$k = \frac{1-\nu_1^2}{E_1} + \frac{1-\nu_2^2}{E_2} \tag{3.1.4}$$

where E and ν are the Young's modulus and Poisson's ratio, respectively. The subscripts of 1 and 2 mean the wall and particle, respectively. By dividing Eq. (3.1.3) by the particle projected area, the impact stress acting on the particle can be described as follows:

$$\sigma_I = \left(\frac{5\rho_p}{3}\right)^{0.6}\left(\frac{4}{3\pi k}\right)^{0.4} u_p^{1.2} \tag{3.1.5}$$

2.4. Fragment size distribution after particle breakage

The fragment size distribution after the particle breakage can be described by a breakage function [7, 10]. In this study, a power-low function, which is a well-known breakage function [8, 12], was used:

$$B = \left(\frac{d_i}{d_0} \right)^a \tag{3.1.6}$$

where d_i and d_0 are the particle size of a fragment and mother particle before the breakage, respectively. a is a parameter which determines width of the fragment size distribution. B means volume ratio of fragments which are smaller than d_i in the all fragments.

3. Numerical simulation

3.1. Numerical simulation of fluid and particle motion

A dry impact pulverizer shown in Fig. 2.1.1 of the previous chapter was used. Fluid flow and particle motion in the dry impact pulverizer were numerically analyzed using the DPM-CFD coupling model (see II-1. 3.).

3.2. Implementation of particle breakage model into DPM-CFD coupling model

Fig. 3.1.3 shows a flow chart of the proposed simulation method. First, the fluid flow and particle motion in the impact pulverizer were calculated using the DPM-CFD coupling model. When a particle impacts against a wall of the grinding chamber, the impact stress acting on the particle (σ_I) was calculated from Eq. (3.1.5) using the particle impact velocity (u_p). The particle strength (σ_S) was then determined. In order to calculate the particle strength (σ_S), two parameters μ_c and S_c in Eq. (3.1.2) were initially calculated from diameter of the impacted particle (d). A crack length C of the impacted particle was then calculated based on the Eq. (3.1.2) with the calculated μ_c and S_c. In the numerical simulation scheme, the crack length C was determined from generated random numbers obeying the log-normal distribution of the Eq. (3.1.2). A Box-Muller transform method [1] was used to generate the random numbers. This transform method can calculate random numbers obeying normal distribution functions from uniform random numbers. The uniform random numbers were calculated using a Mersenne Twister algorithm [6]. By substituting the crack length C into Eq. (3.1.1), the particle strength (σ_S) was finally determined. The mechanical properties of the wall and particle in Eqs. (3.1.4) and (3.1.5) are shown in Table 3.1.1. If the impact stress is smaller than the particle strength ($\sigma_I \leq \sigma_S$), the particle is not broken and rebounds from the wall as the elastic collision. The restitution coefficient was 0.95 [2]. On the other hand, if the impact stress is larger than the particle strength ($\sigma_I > \sigma_S$), the particle is broken and splits into fragments. The fragment sizes are calculated based on the breakage function shown in Eq. (3.1.6). The parameter a in Eq. (3.1.6) was calculated as a function of the particle impact velocity. The correlation between the parameter a and the particle impact velocity was obtained from the experimental results of an impact breakage test. In order

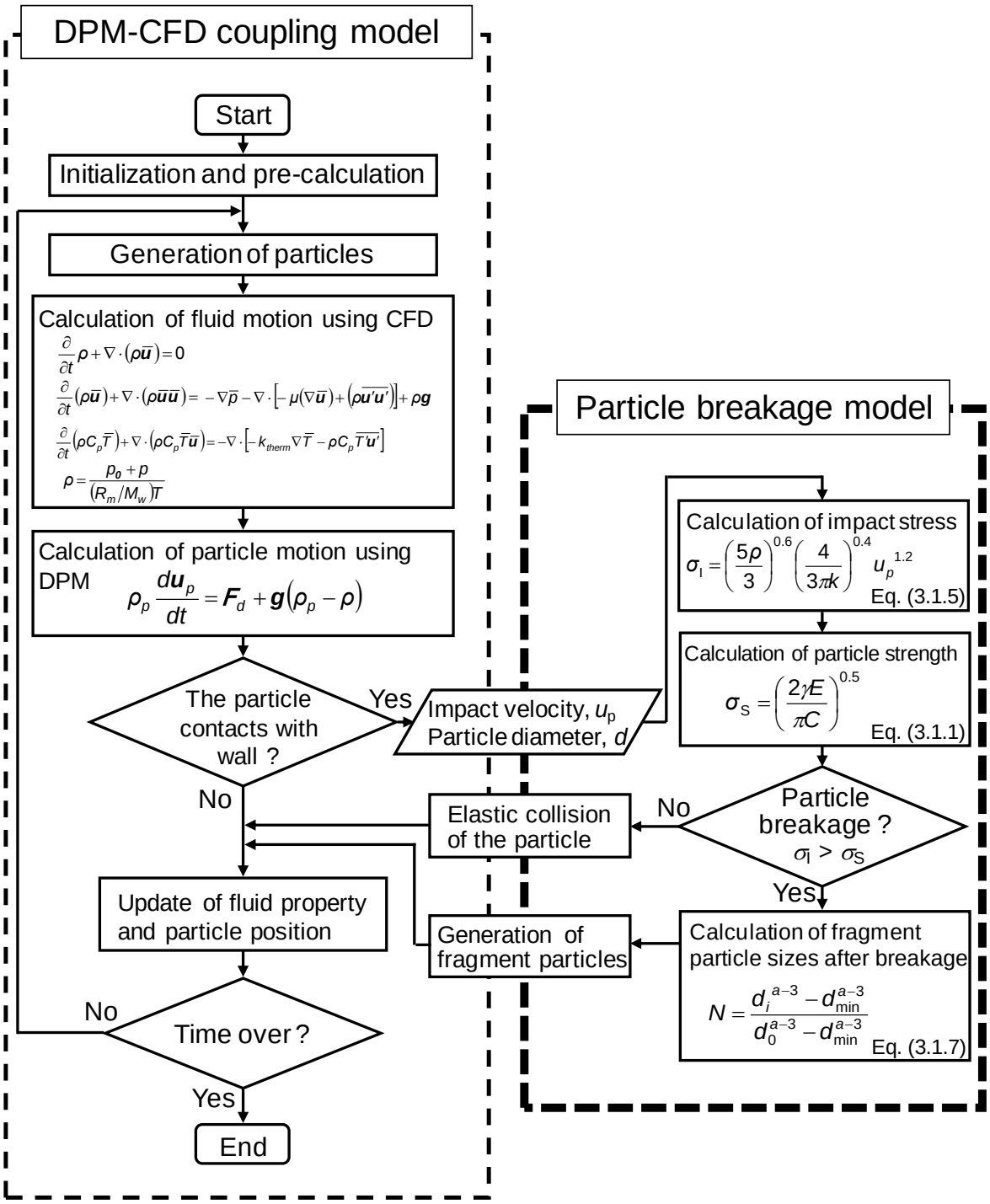

Fig. 3.1.3. Flow chart of proposed simulation method.

Table 3.1.1 Material properties

Property	Particle (glass beads)	Wall (SUS-304)
Young's modulus, E [GPa]	71	200
Poisson's ratio, ν [–]	0.25	0.25
Density, ρ [kg/m^3]	2500	
Surface energy, γ [J/m^2]	4.1[11]	

Table 3.1.2 Calculation conditions

Fluid viscosity	1.789×10^{-5}	[Pa·s]
Inlet pressure	101.3	[kPa]
Outlet pressure	101.3	[kPa]
Rotating speed of rotor	133, 200, 267	[rps]
Time step	8.33	[μs]
Particle diameter of starting materials	210, 500, 690	[μm]
Particle density	2500	[kg/m^3]
Restitution coefficient	0.95	[–]

to calculate the fragment sizes, the breakage function should be converted from a volume basis to a number basis. The number based breakage function N converted from Eq. (3.1.6) is expressed as follows [4]:

$$N = \frac{d_i^{a-3} - d_{\min}^{a-3}}{d_0^{a-3} - d_{\min}^{a-3}} \tag{3.1.7}$$

where d_0 and $d_{\min}$ are the diameter of a particle before the breakage and the minimum diameter of fragments, respectively. In this study, $d_{\min}$ was defined as the d_i at $B = 0.01$ in Eq. (3.1.6) in order to achieve both better accuracy of calculated fragment size and lower computing cost, although a particle smaller than $d_{\min}$ might be generated in an actual particle breakage. The sizes of the individual fragments $d_i (i = 1, 2, 3, \cdots)$ were calculated one-by-one from Eq. (3.1.7). The maximum total number of the fragments after the single particle breakage was set as 30. This maximum number of the fragments was also preliminary optimized in order to achieve both better accuracy of calculated fragment size and lower computing cost. The individual fragments were generated until whether the total volume of the fragments reached to the 98 vol% of the impacted original particle, or the total number of the fragments reached to 29. Only one fragment was then finally generated, and its size was determined to conserve the mass balance before and after the particle breakage. According to this simulation procedure, the particle motion and its breakage in the grinding process can be simulated simultaneously.

3.3. Calculation conditions

The fluid flow and particle motion in the impact pulverizer were calculated by means of a commercial software (Fluent v12.0, ANSYS Inc.). The proposed particle breakage model was implemented into the software using a UDF (User Define Function). The calculation conditions are listed in Table 3.1.2.

After a converged (quasi-steady) fluid flow was simulated without particles, a single particle was fed into the center of the grinding chamber every 8.33 μs. As a standard model particle used in the calculation, glass beads that have a diameter of 500 μm were used. The material properties of the particle and wall are listed in Table 3.1.1. The standard rotating speed of the rotor in the grinding chamber was 267 rps. All computations were performed using a work station (VT64 WorkStation9500, Intel Xeon X5690 3.46 GHz, Visual Technology). It took about 36 h to calculate the converged fluid flow without the particles and 10 days to simulate the fluid motion, particle motion, and its breakage for 15 ms when one core was used.

4. Experimental

4.1. Model particle

Lime soda glass beads (Toshin Rikou Co., Ltd.) with spherical shape and a typical brittle property were used as a model particulate material. The material properties are shown in Table 3.1.1.

4.2. Uniaxial compression test

In order to obtain the parameters S_c and μ_c in the crack length distribution shown in Eq. (3.1.2), single particle strengths were measured by a particle strength tester (Grano 3.01, Okada Seiko Co., Ltd.). Fig. 3.1.4 shows a schematic of the tester. A single particle is broken by compression with the indenter. The tester can measure the compression load and the displacement of the indenter when a particle is broken. The moving velocity of the indenter was set as 100 μm/s. The particle strength was calculated by dividing the particle breakage compression load F_B by the projected area of the particle when the particle was broken:

$$\sigma_S = \frac{F_B}{\pi d^2/4} \tag{3.1.8}$$

The original particles were sieved into size ranges of 106-125, 180-212, 425-500, and 650-710 μm. The particle strengths of 100 particles within each size range were measured.

4.3. Impact breakage test

Impact breakage test was conducted to obtain the parameter a in Eq. (3.1.6). In this test, fragment size distribution after the particle breakage was measured. Fig. 3.1.5 shows a schematic of the experimental apparatus. The apparatus consists of a high-speed rotor (ϕ = 119 mm) covered with a box, pneumatic conveying unit to transport original particles to the impact point, and a bag filter to collect particles after the impact against a hammer. The original particles were transported to the impact point,

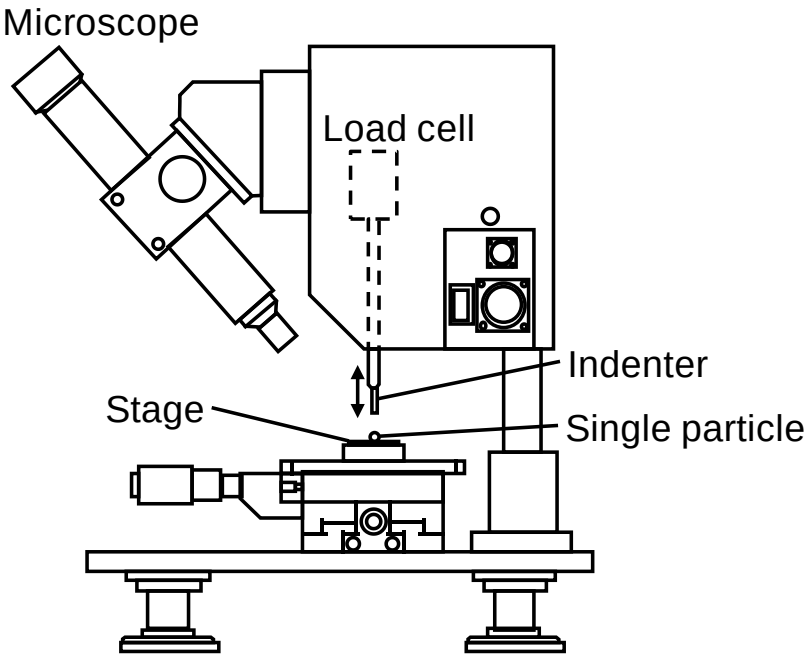

Fig. 3.1.4. Schematic of particle strength tester.

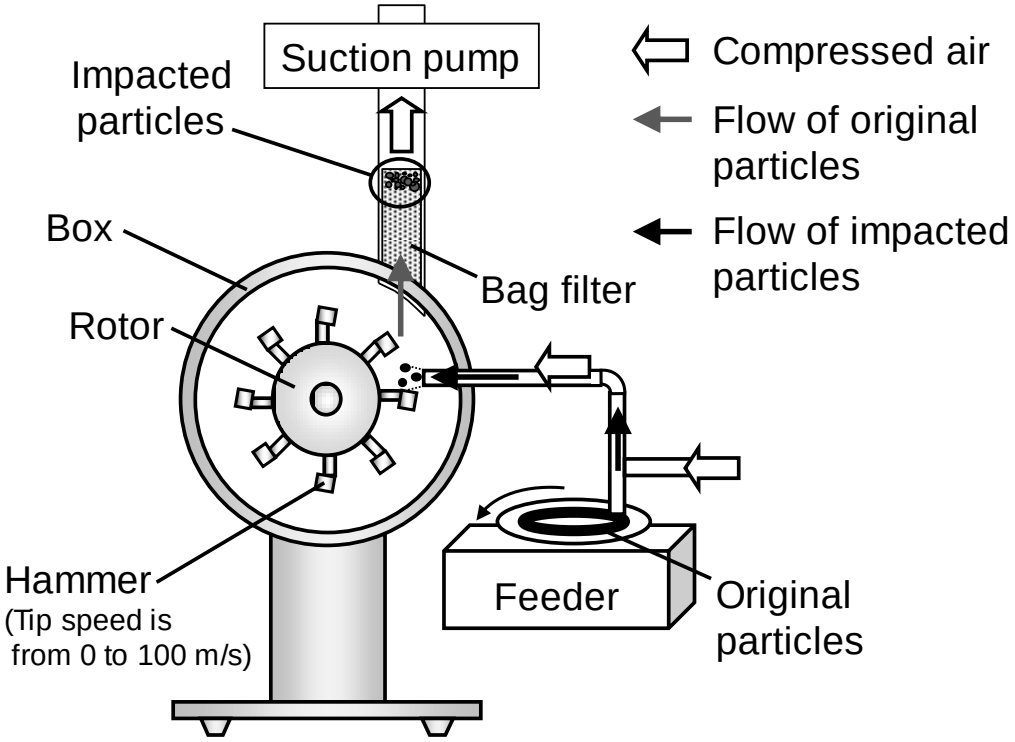

Fig. 3.1.5. Schematic of particle impact breakage tester.

and impacted against the hammer only once. The impact velocity can be changed up to 100 m/s by adjusting the rotating speed of the rotor. When the particles impacted against the hammer wall, the direction of the particle motion is changed, and the particles are collected to the bag filter. Thus, this experimental apparatus can collect only the impacted particles including both broken and unbroken particles. The original particles used in this test were the glass beads shown in Table 3.1.1 and sieved into a size range of 425-500 μm. The size distribution of the collected particles was measured by a sieve analysis.

4.4. Grinding by dry impact pulverizer

In order to compare the calculated result of the particle size distribution of a ground product with the experimental one, a grinding experiment was conducted using the dry impact pulverizer shown in the previous chapter. Feed rate of the glass beads was 30 g/min. Size and geometry of the impact pulverizer and diameter and density of the particle used in the experiment were the same with those in the numerical simulation. The particle size distribution of the final ground product was measured by a sieve analysis.

5. Results and Discussion

5.1. Effect of particle size on particle strength distribution

Fig. 3.1.6 shows a cumulative number frequency of particle strength under various particle diameters. Even when the diameter and the material properties of the original particles were the same, the particle strength was not uniformly distributed. This was because that length of a crack which was an onset of a particle breakage had a distribution. With a decrease in the particle diameter, the particle strength was increased. Curves in Fig. 3.1.6 show the fitting results by the Griffith's theory under the proposed assumption that the crack length has a log-normal distribution, as shown in Eqs. (3.1.1) and (3.1.2). It was found that the two equations well described the experimental results of the particle strength under various particle diameters. Fig. 3.1.7 shows crack length distributions under various particle diameters, calculated by Eq. (3.1.2). With a decrease in the particle diameter, the calculated crack length was decreased. This result well explained the reason why the smaller particles showed higher strength, as shown in Fig. 3.1.6. Width of the crack length distribution was almost the constant regardless of the particle diameter. Fig. 3.1.8 shows correlations of the parameters S_c and μ_c in Eq. (3.1.2) with the particle diameter d. It was found that the mean of the crack length (μ_c) strongly depended on the particle diameter, while the standard deviation of the crack length S_c was almost constant. From these correlations, empirical equations of the parameters S_c and μ_c as a function of particle diameter d were proposed:

$$\mu_c = e^{-2.68+1.51\ln d} \tag{3.1.9}$$

$$S_c = 1.59 \tag{3.1.10}$$

By using Eqs. (3.1.9) and (3.1.10), the particle strength at any particle diameter can be calculated.

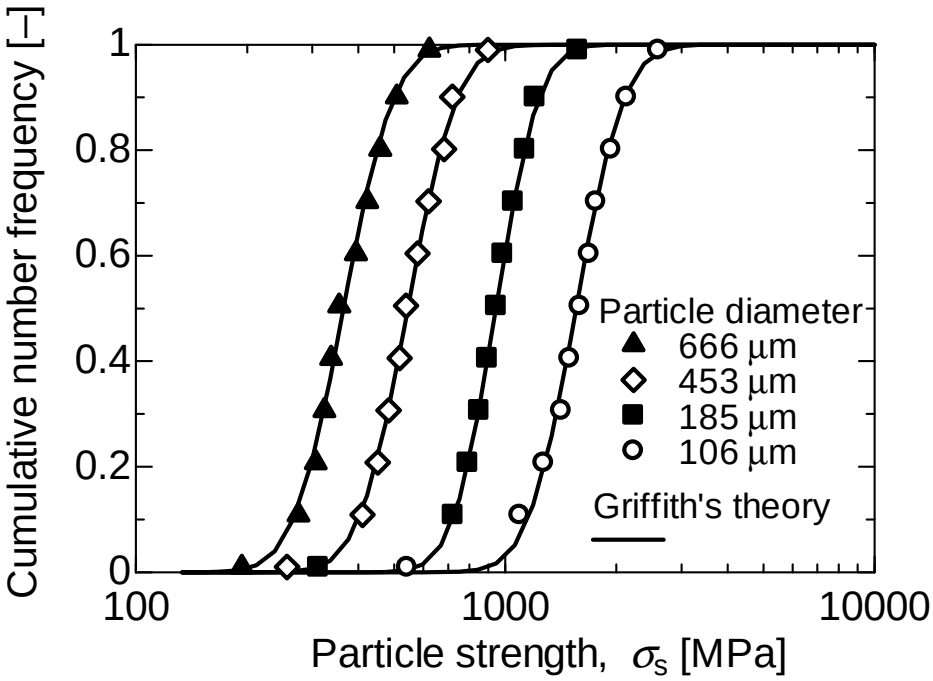

Fig. 3.1.6. Particle strength distribution under various particle sizes.

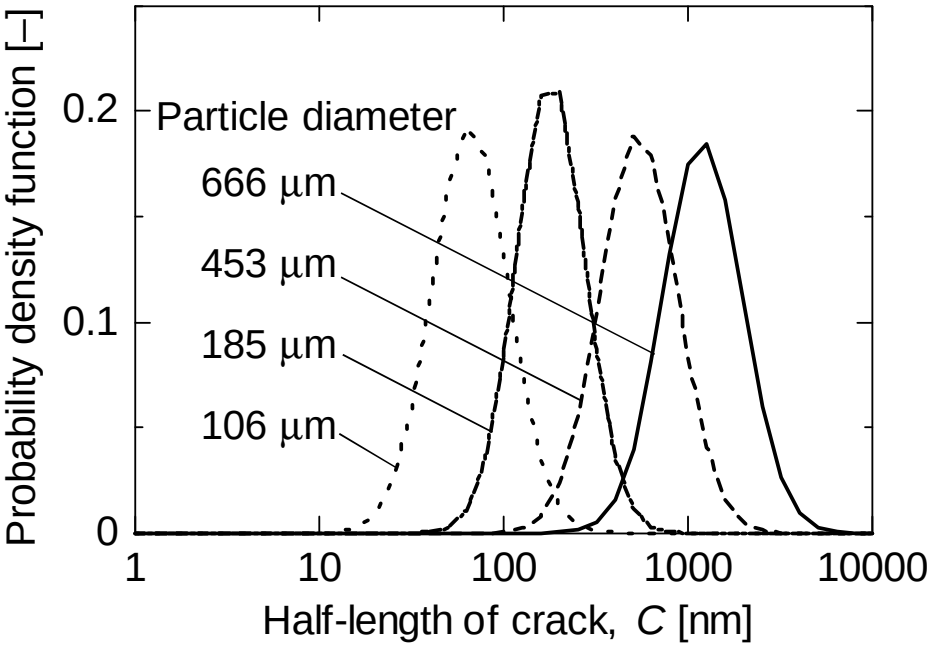

Fig. 3.1.7. Calculated crack length distributions under various particle sizes.

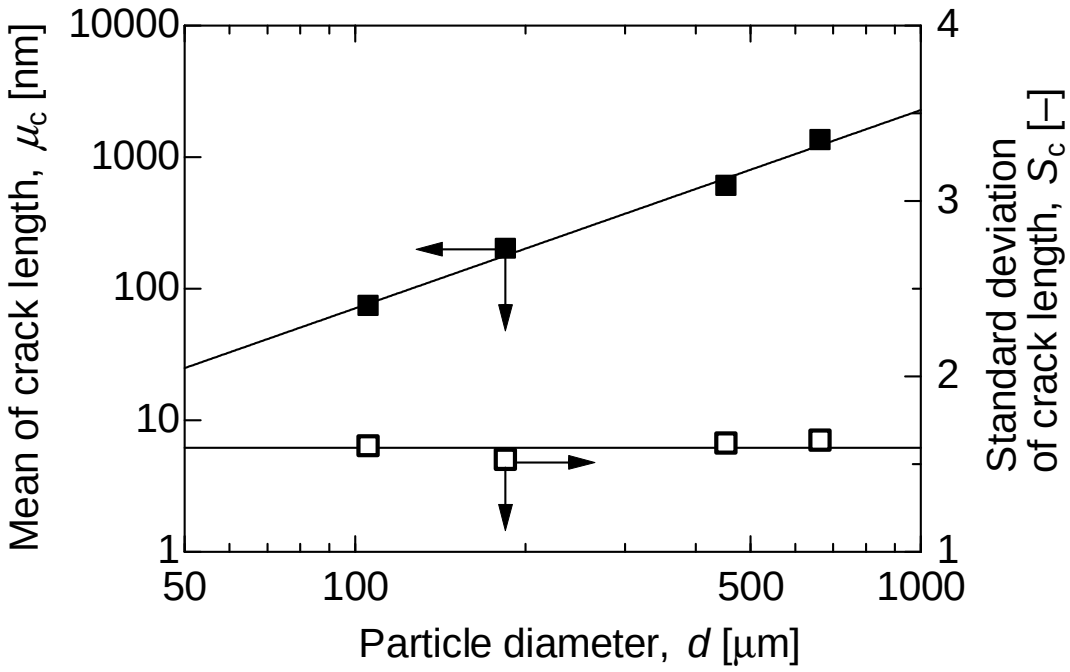

Fig. 3.1.8. Correlation between parameters of crack length distribution and particle diameter.

5.2. Effect of impact velocity on fragment size distribution

Fig. 3.1.9 shows mass-based fragment size distributions under various impact velocities. At the lowest impact velocity (25 m/s), more than 90% of the fragment particles were coarse fragments larger than 400 μm. This result indicated that at this lowest impact velocity the particles were mainly broken by the attrition. However, with an increase in the impact velocity, frequency of the coarse fragment particles was decreased. This result showed the particles were mainly broken by the volume grinding at the higher impact velocity. This was because that the crack could widely propagate and reach to inside of the particle [9] at the higher impact velocity. Therefore, it was found that the fragment size distribution strongly depended on the impact velocity and should be modeled as a function of the impact velocity. The curves in Fig. 3.1.9 indicate the fitting results by the breakage function shown in Eq. (3.1.6). The fitting results well described the experimental results at the higher impact velocities, although the fitting results were slightly different to the experimental results at the lower impact velocities. This was because that the breakage function used in this study described size distribution of fine fragments more accurately than the coarser fragments [12]. Nevertheless, the breakage function well described the experimental results in the range of the impact velocities within 25 and 100 m/s. Thus, the breakage function shown in Eq. (3.1.6) was found to be used to calculate the fragment size distribution after the particle breakage.

Fig. 3.1.10 shows a correlation of the parameter a in Eq. (3.1.6) with the impact velocity of the particle u_p. With an increase in the impact velocity, the parameter a was decreased. This meant that width of the fragment size distribution became wider with an increase in the impact velocity. The parameter a strongly depended on the impact velocity u_p. An empirical equation of the correlation between the a and u_p was obtained:

$$a = 2684\, u_p^{-1.625} \tag{3.1.11}$$

By using this equation, a breakage function could be determined as a function of the impact velocity.

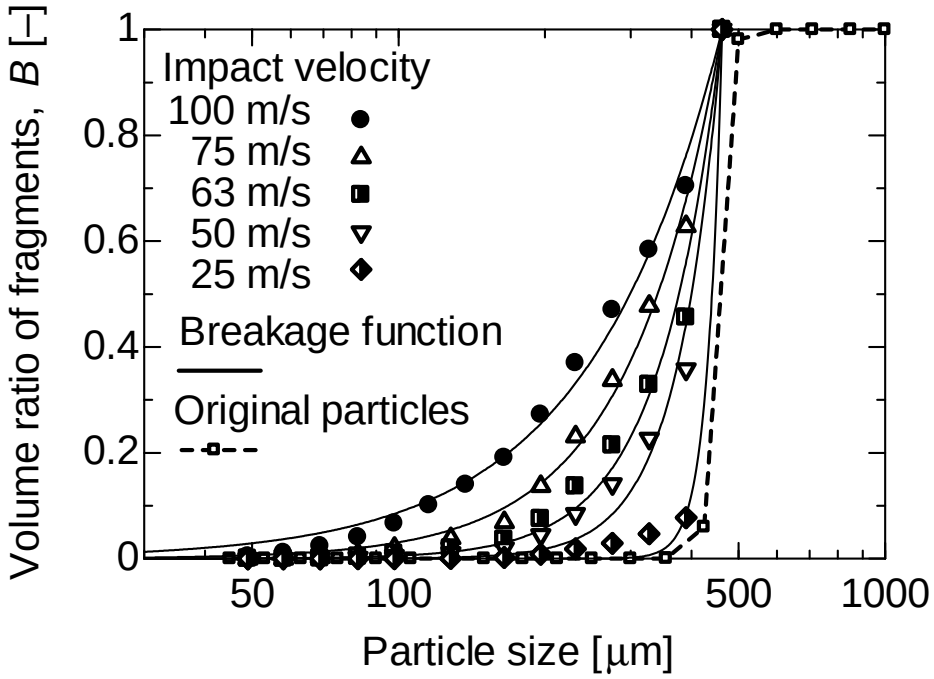

Fig. 3.1.9. Fragment size distribution under various impact velocities.

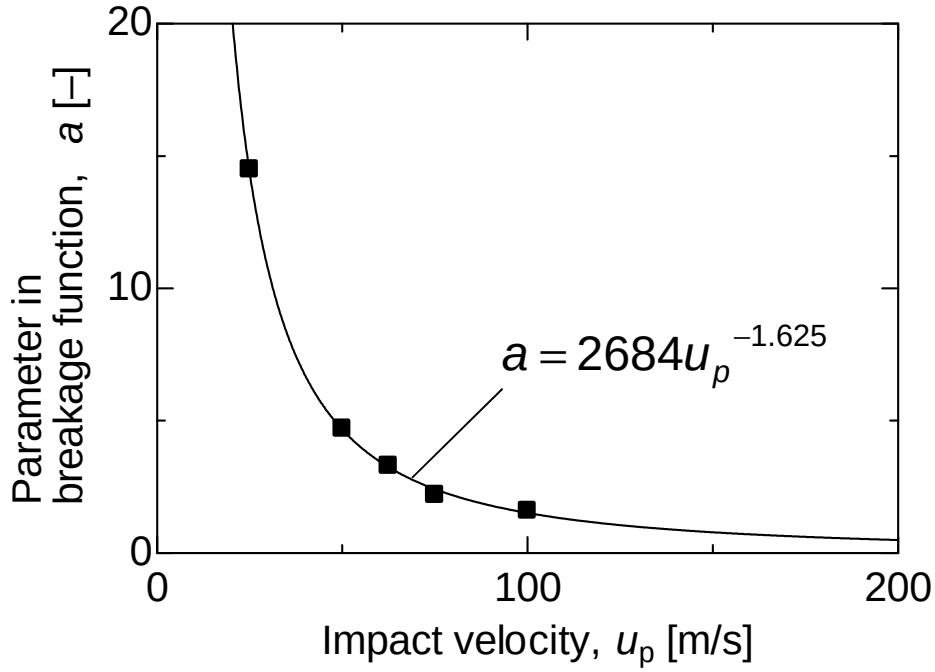

Fig. 3.1.10. Correlation between parameter *a* in breakage function and impact velocity.

5.3. Simulation results of particle breakage in an impact pulverizer

The proposed particle breakage model, which can calculate the particle strength, the impact stress acting on the particle, and the fragment size distribution after the particle breakage, were implemented into the DPM-CFD coupling model to simulate the motion and the breakage of whole particles in the impact pulverizer. Fig. 3.1.11 shows snapshots of particles in the grinding chamber at different grinding times. t = 0 ms means the starting time of the particle breakage. The particles are colored according to its particle size, and the size of the particle is enlarged by 2 times in order to clearly visualize the particles. The particles were initially transported from center to circumference of the grinding chamber. With an increase in the grinding time, the particles were broken and many fragments were generated, resulting in a drastic increase in number of the particles. The total number of the particles reached to about 3,340,000 at t = 15.0 ms, which was more than 1700 times as much as total number of the starting material particles (500 μm) which were fed into the grinding chamber.

Fig. 3.1.12 shows temporal change in the number-based particle size distribution in the grinding chamber. Fig. 3.1.13 shows the number-based particle median diameter as a function of the grinding time. At the early stage of the grinding operation, the grinding rate was very high. Even for a short grinding time (t = 1.7 ms), the particle size distribution quickly shifted to the smaller particle size and the particle median diameter decreased to less than one-fiftieth of the original particle size. At the early stage of the grinding, the strength of the most of the particles was much smaller than the impact stress. Thus, the most of the particles impacting against the stator wall could be broken. After t = 6 ms, however, the particle size distribution was almost unchanged. This was because that the particle strength increased with a decrease in the particle size. In addition, the impact stress was decreased with a decrease in the particle size. This leads to difficulties of the particle breakage. The calculated median diameter showed similar propensity with an actual grinding phenomena, namely, a grinding limit.

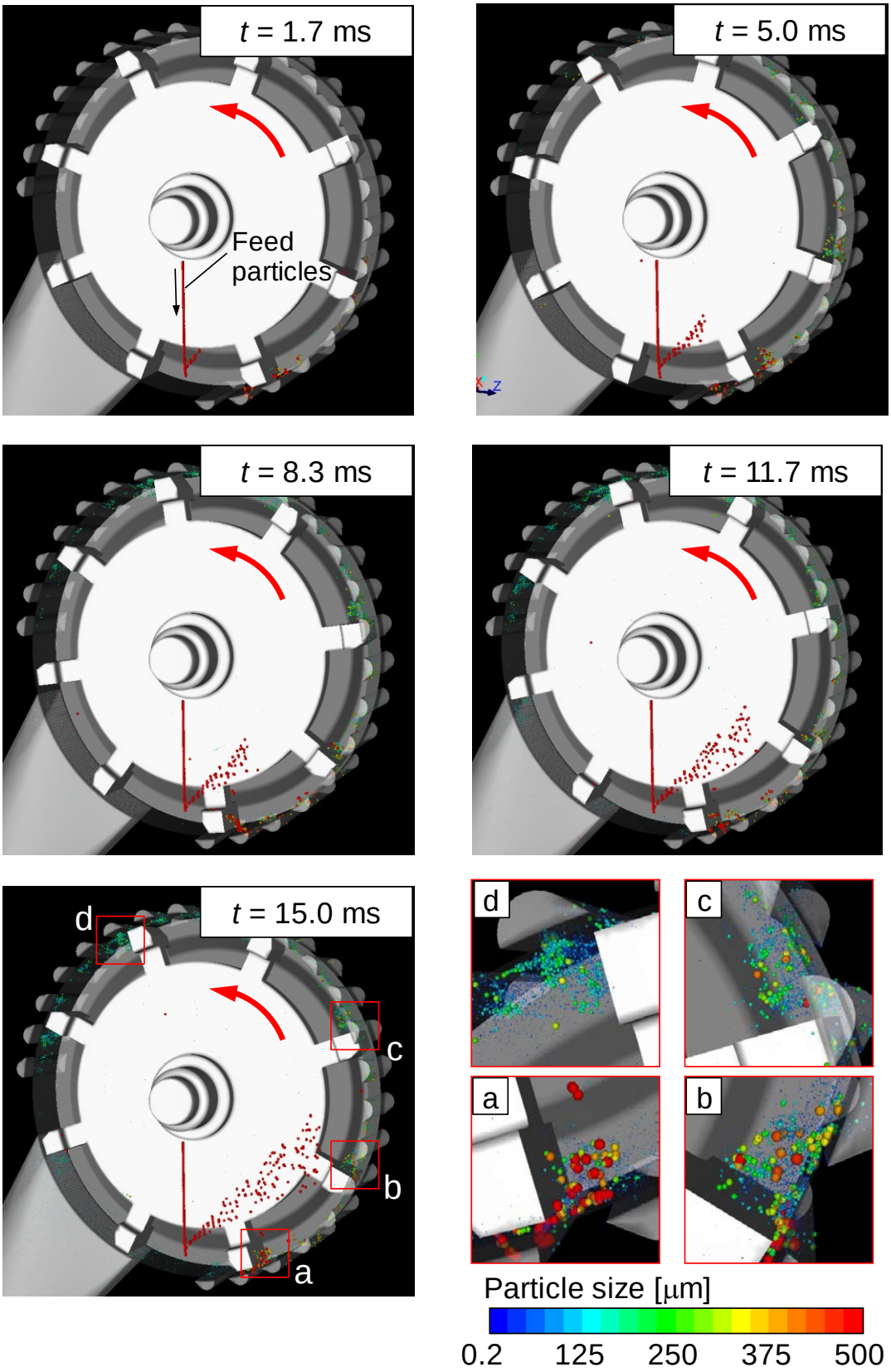

Fig. 3.1.11. Simulation results of particle distribution in grinding chamber.

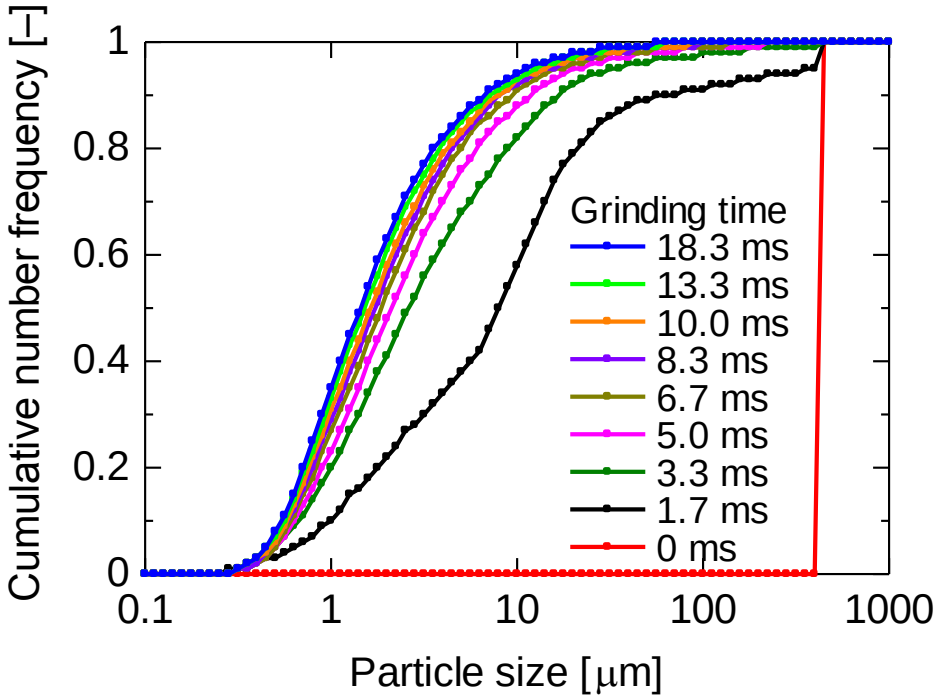

Fig. 3.1.12. Temporal change in number-based cumulative particle size distribution in grinding chamber.

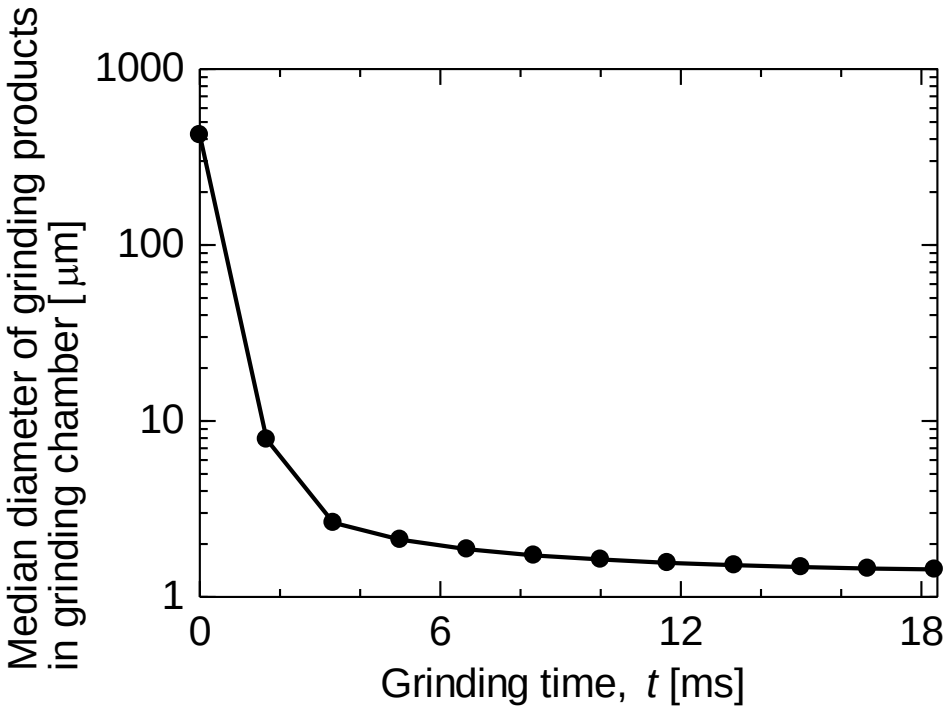

Fig. 3.1.13. Temporal change in median diameter of particles in grinding chamber.

5.4. Analysis of particle breakage in grinding chamber

Fig. 3.1.14 shows snapshots of the particles just before the particle breakage. The particles are colored according to its particle size, and the size of the particle is enlarged by 6.5 times in order to clearly visualize. At t = 1.7 ms, most of the starting material particles (500 μm) were broken at the bottom-right of the grinding chamber. Then, at t = 5.0 ms, particles smaller than the starting material particles were broken at the top-right. These smaller particles were the fragments generated at t = 1.7 ms. At t = 8.3 ms, the particles smaller than 100 μm were broken at the top-left. These particles were the generated fragments at t = 5.0 ms. After t = 11.7 ms, distribution of the particles just before the particle breakage showed almost steady state. The particle size before the breakage was decreased with a counterclockwise direction beginning at the bottom-right of the grinding chamber. Most of the starting material particles were firstly broken at the bottom-right and pulverized to the fragments smaller than 100 μm while the particles revolved along the stator for one-revolution. This simulation result revealed that where the particle is broken in the grinding chamber and how much size the particles have just before the breakage.

Fig. 3.1.15 shows number-based size distributions of the particles just before the particle breakage. The size of the particles was decreased with an increase in the grinding time because smaller fragments were more generated. However, the size did not show smaller than 40 μm. This size limitation of broken particles was determined from balance between the attainable maximum impact stress acting on the particle and the particle strength. The attainable maximum impact stress was determined from the type of the grinding equipment and the operation conditions. Therefore, the particles smaller than about 40 μm were not broken, because the attainable maximum impact stress derived from intrinsic performance of the impact pulverizer could not exceed the strength of the particles smaller than 40 μm particle. Accordingly, the size limitation of the particles which can be broken was well expressed in the proposed simulation method.

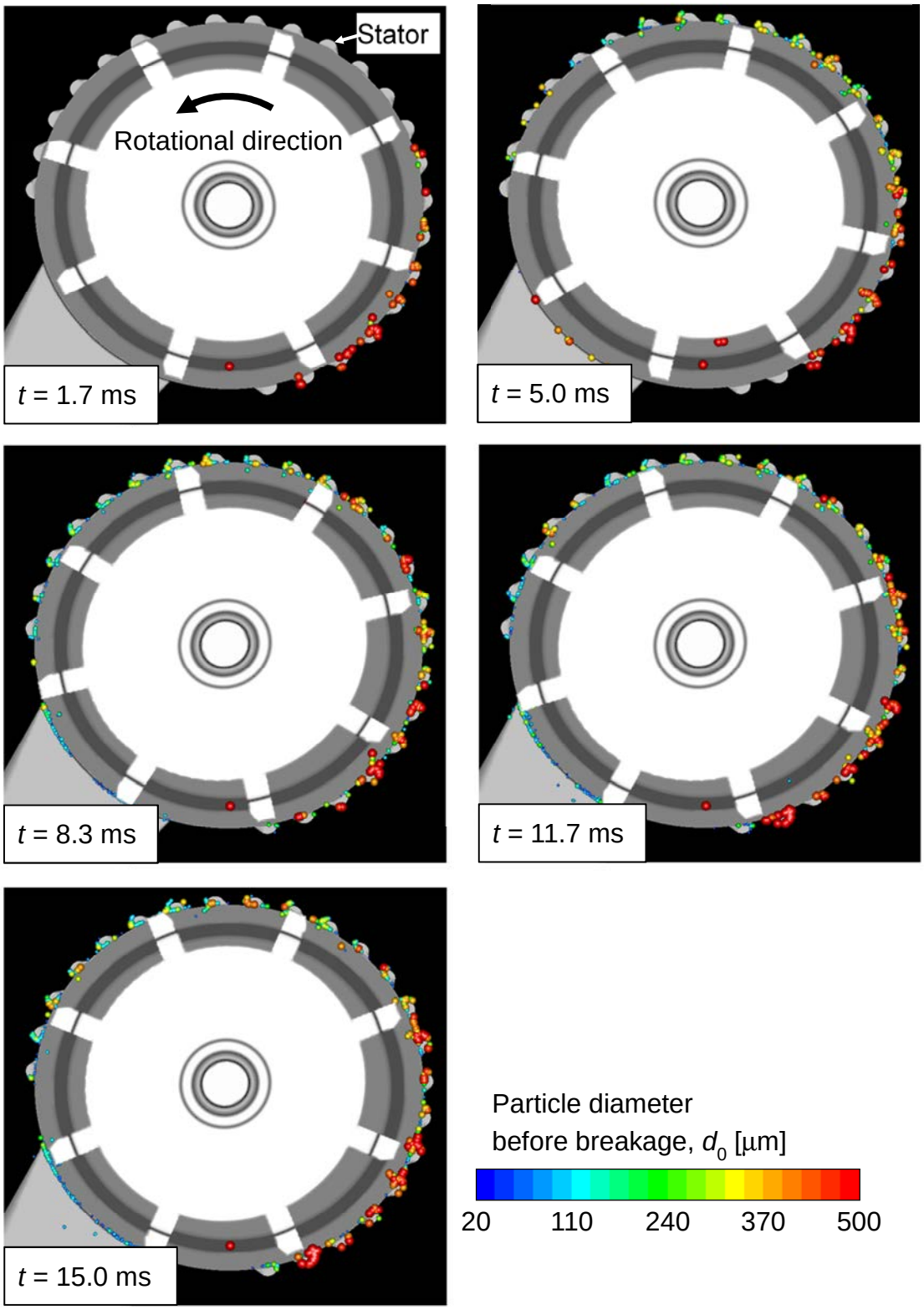

Fig. 3.1.14. Snap shots of particles before breakage in grinding chamber.

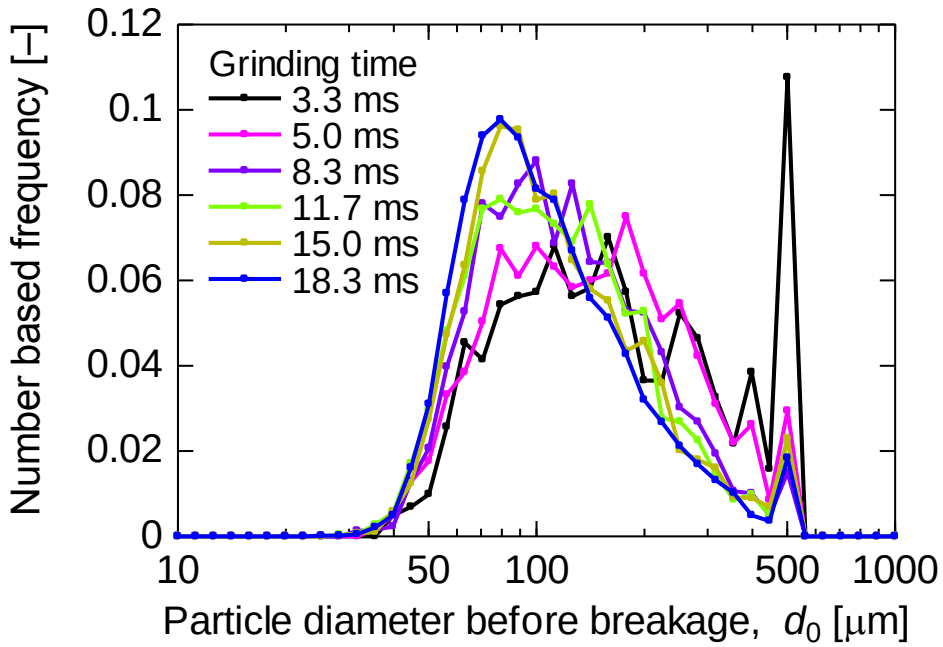

Fig. 3.1.15. Number based size distribution of particles before breakage in grinding chamber.

5.5. Comparison of simulation results with experimental results

The particles in the grinding chamber are discharged thorough the classification screen and collected in the collection pot as the final ground product. Fig. 3.1.16 indicates a temporal change in calculated size distribution of the particles in the collection pot. In the early stage of the grinding, the particle size distribution of the final ground product was changed because amount of the recovered particles was tiny. However, with a further increase in the grinding time, the particle size distribution reached to constant regardless of the grinding time. Thus, the calculated results at t = 18.3 ms were compared with the experimental ones.

Fig. 3.1.17 shows particle size distributions of the starting material and final ground product to compare the numerical simulation result with the experimental result. In this figure, the red plots with the dashed line indicate particle size distribution of the starting material used in the experiment. The blue plots with the dashed line show particle size distribution of the final ground product collected in the collection pot obtained in the experiment. The red solid line indicates an input value of the particle size distribution of the starting material for the numerical simulation. The blue solid line shows the calculated result of particle size distribution of the final ground product. In the ground products, the calculated mass fraction at the size range larger than 100 μm was lower than the experimental one, while the calculated mass fraction at the size range smaller than 50 μm was higher than the experimental mass fraction. This was due to a characteristic of the breakage function (Eq. 3.1.7), in which the smaller fragments were more likely to be generated rather than the larger fragments, when the maximum number of the fragments was small. In this study, the maximum number of the fragments was set as 30. This condition was preliminary optimized in order to achieve both better accuracy of calculated fragment size and lower computing cost. Nevertheless, the calculated particle size distribution of the final ground product showed acceptable agreement with the experimental one. In summary, the prediction of the particle size distribution of the final ground product in a grinding process is possible using the proposed simulation method.

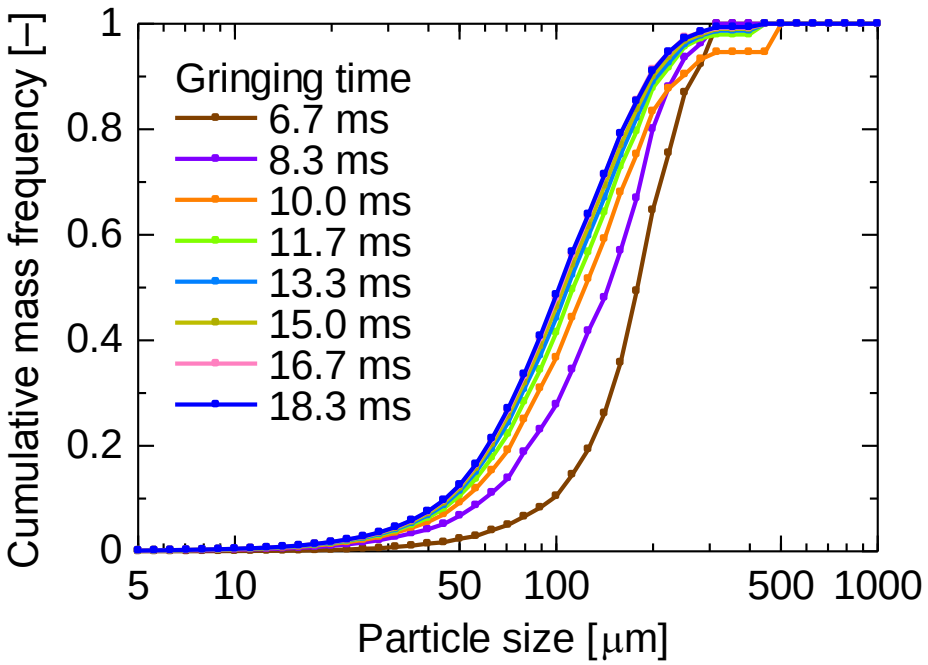

Fig. 3.1.16. Temporal change in calculated particle size distribution of final ground product.

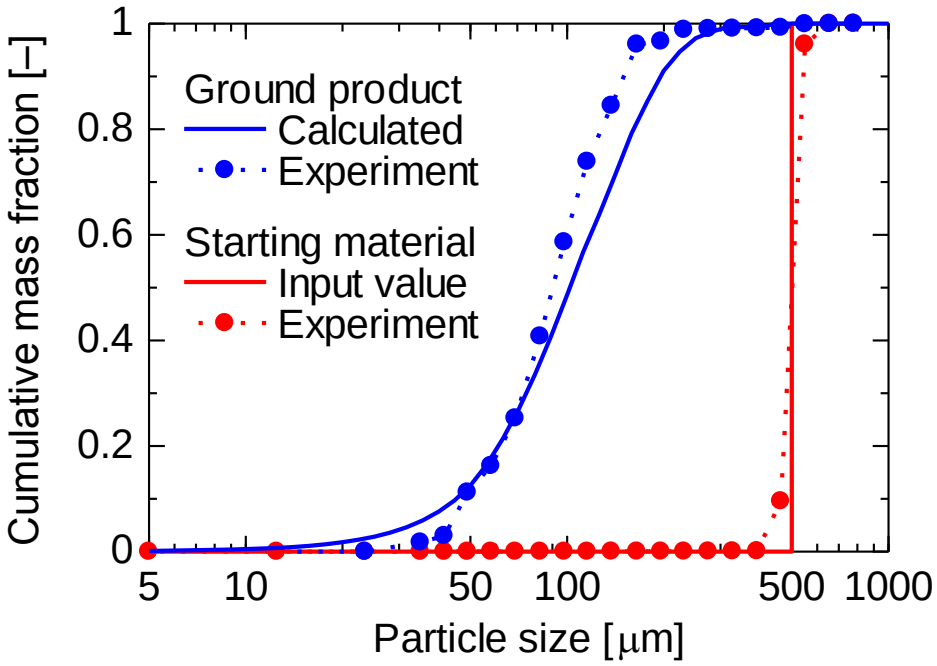

Fig. 3.1.17. Comparison of calculated particle size distribution of ground products with experimental one.

5.6. Effect of particle size of starting material on size of final ground products

Fig. 3.1.18 indicates temporal changes in median diameter of particles in grinding chamber under various particle diameters of starting materials, D_f. In all the particle diameters of starting materials, the median diameter decreased and became almost constant from t = 6 ms. The constant value of the median diameter was approximately 2 μm regardless of particle diameter of starting materials. This was because that particles were broken and splits into fragments, and most of them had a diameter of about 2 μm due to high-speed impact velocity more than 100 m/s.

Fig. 3.1.19 shows comparisons between experimental results of particle size distribution of the final ground products and the calculated ones under various particle diameters of the starting materials. Only at D_f = 690 μm, the calculated particle size distribution were less than the experimental one. This was because that maximum number of the fragments was not enough for modeling of breakage of large size particle. This problem will be solved by an increase in the number of fragments after the particle breakage. At D_f = 210, 500 μm, however, the calculated particle size distribution showed good agreement with the experimental ones.

5.7. Effect of rotating speed of rotor on size of final ground products

Fig. 3.1.20 indicates temporal changes in median diameter of particles in grinding chamber under various rotating speed of the rotor, R. The median diameter drastically decreased from t = 0 to 6 ms and became constant. The constant value of the median diameter increased with a decrease in the rotating speed. The minimum size of the fragments after the particle breakage increased due to a decrease in the impact stress acting on the particle when the rotating speed was low. Therefore, the constant value of the median diameter increased with a decrease in the rotating speed.

Fig. 3.1.21 shows comparisons between experimental results of particle size distribution of final ground products and calculated ones under various rotating speeds. The calculated particle size distributions were in good agreement with the experimental ones. Therefore, it is confirmed that the proposed simulation method could simulate particle motion and its breakage under various operating conditions such as particle diameter of the starting materials and rotating speed of the rotor.

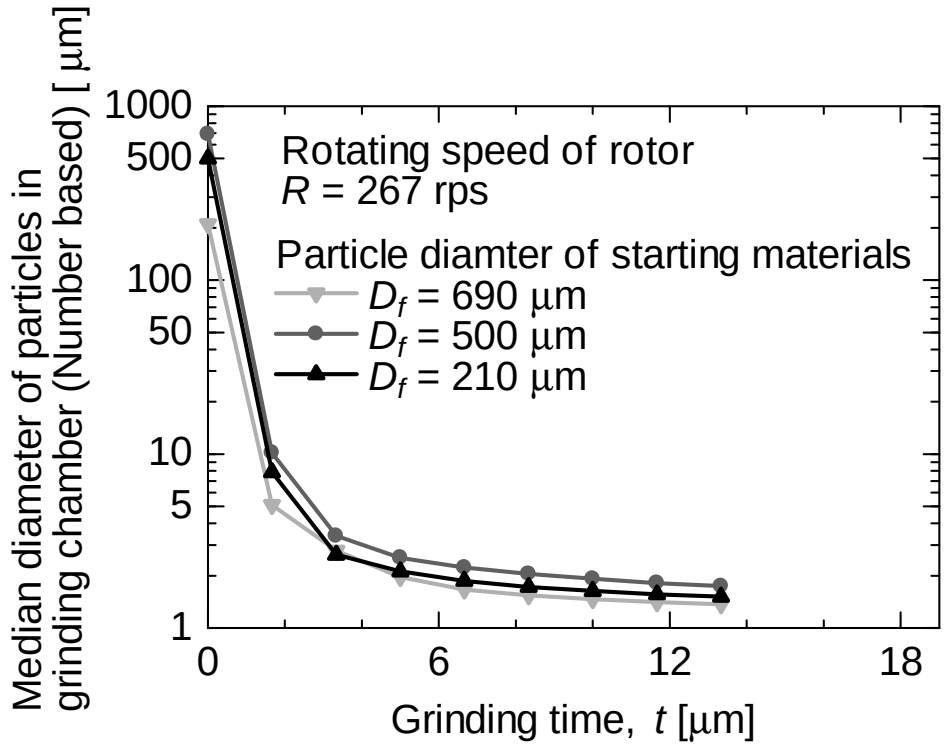

Fig. 3.1.18. Median diamater of particles in grinding chamber under various particle sizes of starting materials.

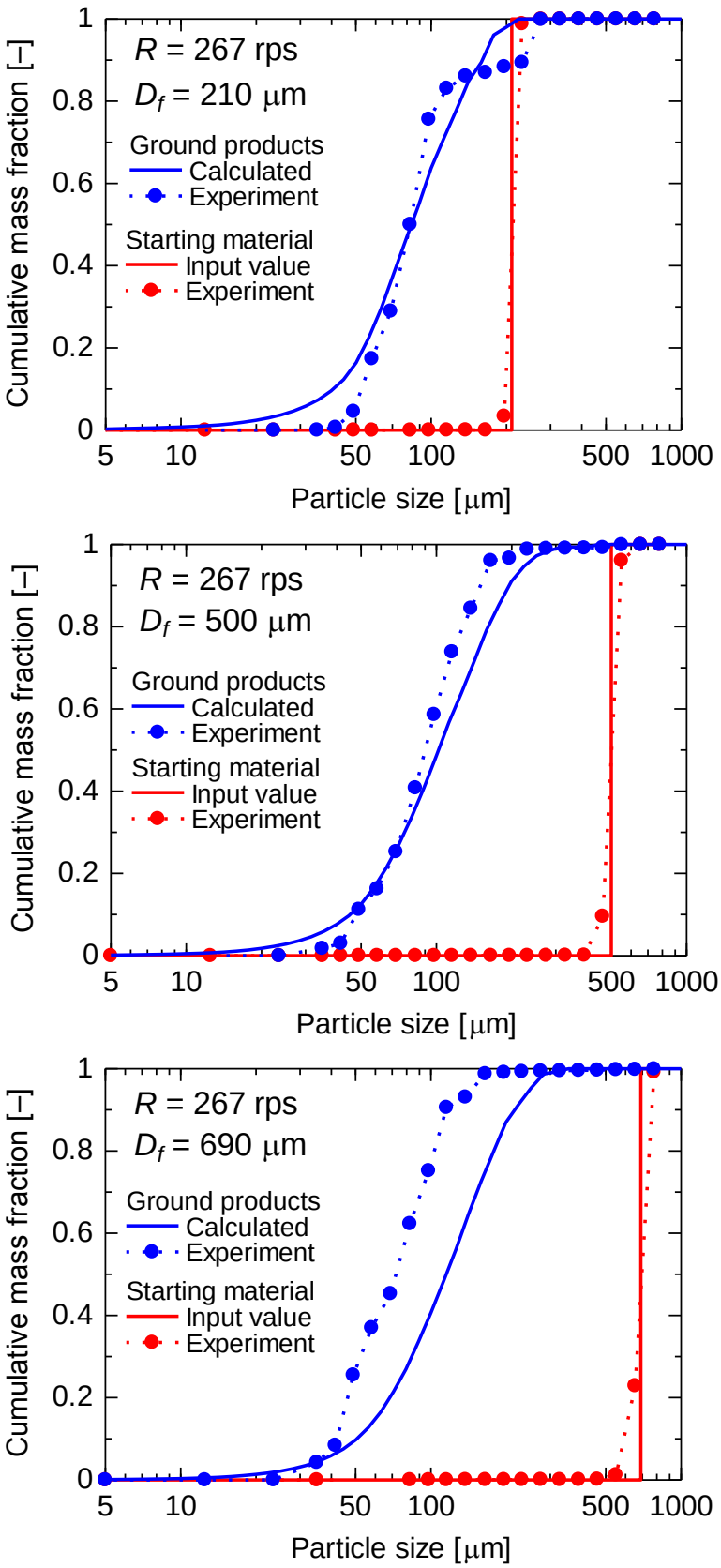

Fig. 3.1.19. Comparison of calculated particle size distribution of ground products with experimental one under various particle sizes of starting materials.

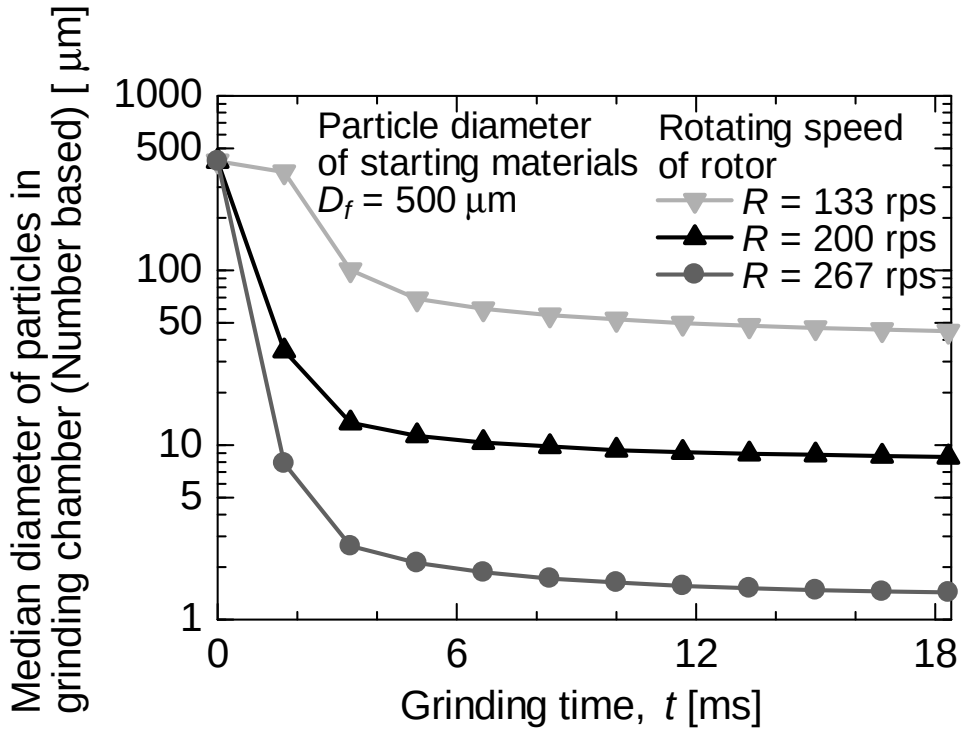

Fig. 3.1.20. Median diamater of particles in grinding chamber under various rotating speeds of rotor.

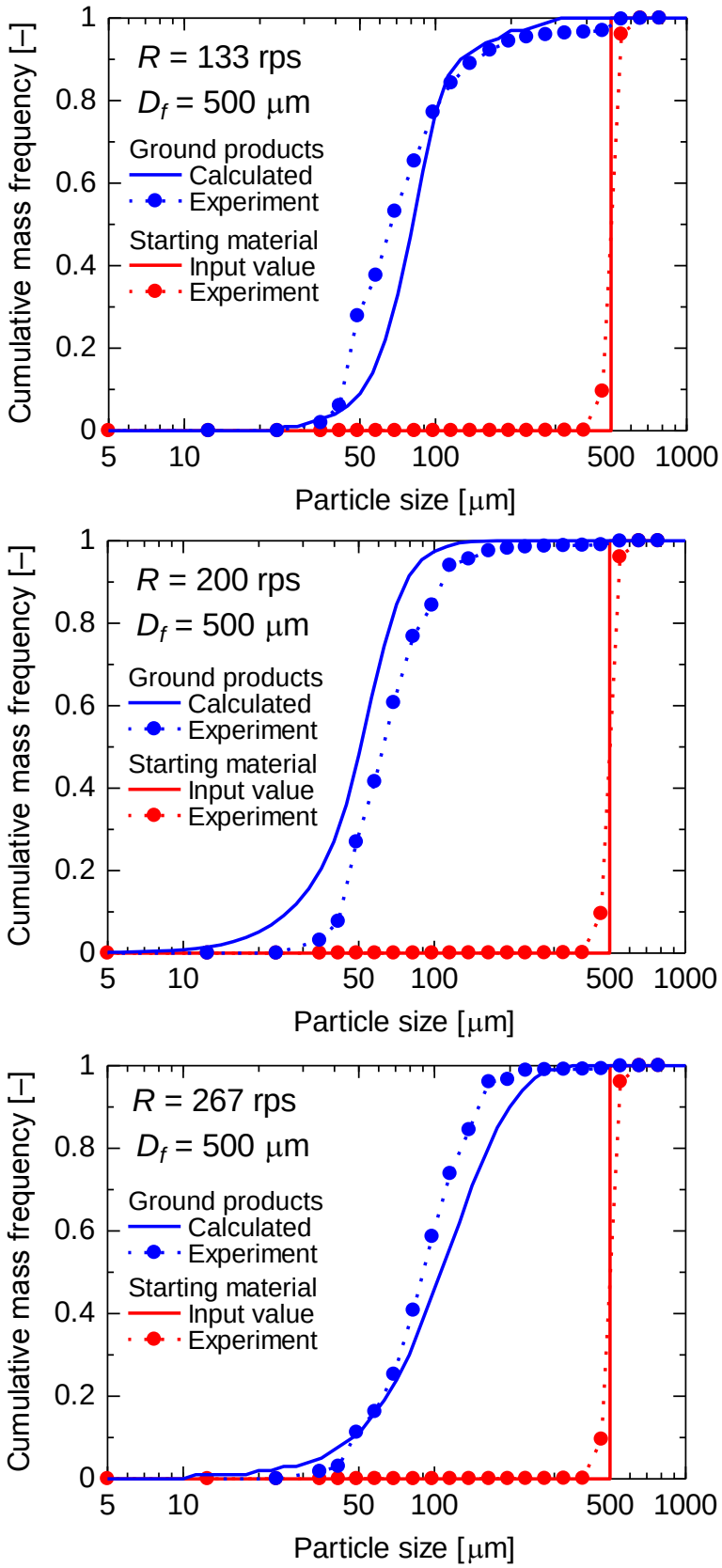

Fig. 3.1.21. Comparison of calculated particle size distribution of ground products with experimental one under various rotating speeds of rotor.

6. Conclusions

A novel simulation method to simultaneously calculate the particle motion and its breakage in a dry impact pulverizer was developed. The particle strength which was obtained from a uniaxial compression test could be well described by Griffith's theory under the assumption that the crack length obeys a log-normal distribution. The size distribution of the fragments which was obtained from an impact breakage test was described by a power-low function. The parameter of the power-low function could be expressed as a function of the impact velocity. The calculated results of particle motion and its breakage phenomenon using the proposed simulation method showed similar results to that in actual grinding behavior such as a particle size reduction, increase in number of the particles, and size limitation of the particles which can be broken. The simulation results also exhibited clearly where and how the particles were broken in the grinding chamber. When only large particles were used as starting materials, the calculated particle size distribution of the final ground product was less than experimental result. However, under other various operating conditions, the calculated particle size distributions showed good agreement with experimental ones. The proposed simulation method enables us to fully understand the grinding phenomenon in many kinds of grinding process and also predict a particle size distribution of the final ground product.

Nomenclature

a	: Parameter in Eq. (3.1.6)	[–]
B	: Volume ratio of fragments smaller than d_i (Breakage function)	[–]
C	: Half-length of crack	[m]
d	: Particle diameter	[m]
d_i	: Particle diameter of fragments (i= 1, 2, 3, ···)	[m]
d_0	: Particle diameter of mother particle before breakage	[m]
$d_{\min}$	: Particle diameter of minimum fragments	[m]
D_f	: Particle diameter of starting materials	[m]
E	: Young's modulus	[Pa]

F_{I}	: Maximum impact load	[N]
F_{B}	: Compression load at particle breakage	[N]
$f(C)$	: Crack length distribution	[–]
k	: Parameter defined by Eq. (3.1.4)	[1/Pa]
N	: Number ratio of fragments smaller than d_i	[–]
R	: Rotating speed of rotor	[rps]
S_{c}	: Standard deviation of crack length	[–]
t	: Grinding time	[s]
U_m	: Mechanical energy	[J]
U_s	: Surface energy of a crack	[J]
u_{p}	: Velocity of particle impact	[m/s]

Greek letters

γ	: Surface energy	[J/m^2]
μ_{c}	: Mean of crack length	[m]
ν	: Poisson's ratio	[–]
ρ_{p}	: Particle density	[kg/m^3]
σ_A	: Tensile stress	[Pa]
σ_{I}	: Maximum impact stress	[Pa]
σ_{S}	: Tensile strength of particle	[Pa]

Subscripts

c	: Crack length
I	: Impact
p	: Particle
S	: Strength

References

1 Box GEP, Muller ME. A note on the generation of random normal deviates. Ann. Math. Statist. 1958;29:610-611.

2 Goldsmith W, Lyman PT. The penetration of hard-steel spheres into plane metal surfaces. ASME J. Appl. Mech. 1960;27:17-25.

3 Griffith AA. The theory of rupture. In: 1st International Congress of Applied Mechanics; 1924; Delft, Nederland. p. 55-63.

4 Kalman H, Rodnianski V, Haim M. A new method to implement comminution functions into DEM simulation of a size reduction system due to particle-wall collisions. Granular Matter. 2009;11:253-266.

5 Knight CG, Swain MV, Chaudhri MM. Impact of small steel spheres on glass surfaces. J. Mater. Sci. 1977;12:1573-1586.

6 Matsumoto M, Nishimura T. Mersenne twister: a 623-dimensionally equidistributed uniform pseudo-random number generator. ACM Trans. Model. Comput. Simul. 1998;8:3-30.

7 Meier M, John E, Wieckhusen D, Wirth W, Peukert W. Generally applicable breakage functions derived from single particle comminution data. Powder Technol. 2009;194:33-41.

8 Nikolov S. A performance model for impact crushers. Miner. Eng. 2002;15:715-721.

9 Potapov AV, Campbell CS. Parametric dependence of particle breakage mechanisms. Powder Technol. 2001;120:164-174.

10 Sahoo R. Review: An investigation of single particle breakage tests for coal handling system of the gladstone port. Powder Technol. 2006;161:158-167.

11 Wiederhorn SM. Fracture surface energy of glass. J. Am. Ceram. Soc. 1969;52:99-105.

12 Wu SZ, Chau KT, Yu TX. Crushing and fragmentation of brittle spheres under double impact test. Powder Technol. 2004;143-144:41-55.

Chapter IV

Development of a novel particle size control system for dry impact pulverizer

1. Introduction

In a dry grinding process, it is required to maintain particle size of the ground products at a desired value of usage. However, particle size of the ground products varies even if the starting materials are ground under the same grinding conditions. This is because that characteristics of the dry grinding processes vary depending on the external environment of the grinding operation and physical properties of powders such as particle size, moisture content, and electro static charge. Therefore, it is necessary to fully understand particle behavior and particle breakage mechanism in the dry grinding process for making a dynamic model of the dry grinding process in order to control the particle size of the ground products in the dry grinding process.

In the previous chapters, numerical simulation clarified that how particles behaved and were broken in a dry impact pulverizer. A key factor involved in the grinding phenomena was understood from the calculated results. In this chapter, by using the knowledge of the calculated results, modeling of the dry grinding process for automatically controlling particle size of the ground products was conducted.

So far, in order to control the particle size in the grinding processes, automatic control methods e.g., PID (Proportional Integral Derivative) control have been employed [2]. However, the conventional control methods should change parameters in its control model depending on the starting materials. On the other hand, a fuzzy control method is a useful scheme because the fuzzy control logic [5] is based on a linguistic algorithm. The fuzzy control can be easily adapted to variations of the starting materials without significant modification of the linguistic algorithm [3, 4]. Thus, the fuzzy control is expected to be applicable to control particle size in the dry grinding processes.

In this chapter, a practical system for controlling particle size of the ground products in a dry impact pulverizer has been developed. This system consists of a dry impact pulverizer, an on-line particle size measurement unit, and a fuzzy controller using a fuzzy logic based on a linguistic algorithm employing IF-THEN rules. First of all, validity of the on-line measurement of particle size of the ground products was confirmed. Then, performance of the system was experimentally investigated under various conditions such as desired particle sizes, starting materials, and disturbances. Accuracy of the particle size control was also investigated.

2. Experimental

2.1. Experimental apparatus

Fig. 4.1.1 shows a schematic diagram of the developed system for controlling particle size of the ground products in the dry impact pulverizer. The dry impact pulverizer shown in Fig. 2.1.1 was also used. A starting material was continuously fed into the center of the chamber and ground by the interaction of a high-speed rotating rotor and stator. The ground particles passed through the classification screen and were collected as the final ground products in a collection pot. A part of the ground particles was sampled out to measure the particle size distribution at on-line by an aspirator using a compressed air through a sampling tube connected between the classification screen and collection pot. The particles were transported into a laser diffraction particle size analyzer (LA-950, Horiba Ltd.) by a pneumatic conveyor. It takes a few seconds to transport the sampled particles from the sampling point to the measuring point. However, more than 10 seconds are needed until the ground particle size is stabilized when rotating speed of the rotor was changed. The particle size distribution of products was continuously measured and sent to a fuzzy controller. The fuzzy controller determined the value of the manipulated variable (rotating speed of the rotor) which was automatically adjusted to an appropriate value. In the experiments, lactose hydrates (Pharmatose 80M, DMV International, d_{50} = 254 μm and Pharmatose 50M, DMV International, d_{50} = 312 μm) which are widely used as a pharmaceutical excipients and a ℓ-valine (Ajinomoto Co., Ltd., d_{50} = 206 μm) which is an active pharmaceutical ingredient of amino acid formulation were employed as model starting materials.

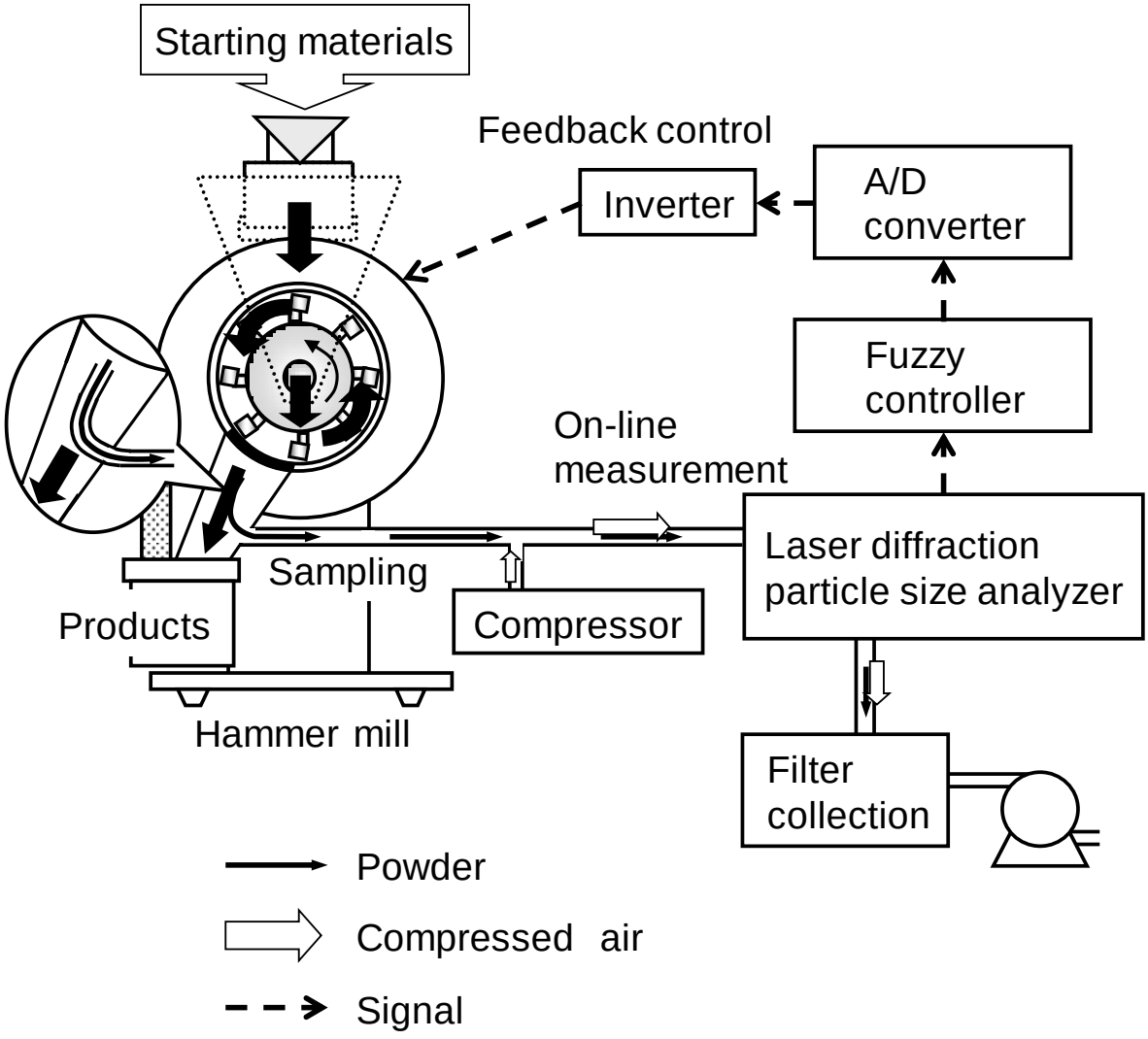

Fig. 4.1.1. Schematic of feedback control system.

2.2. Validation of on-line measurement

Fig. 4.1.2 indicates a median diameter of the ground products as a function of a rotating speed of the rotor under various materials measured by both on-line and off-line measurements. In this figure, off-line values were obtained by measuring the median diameter of products in collection pot using a laser diffraction particle size analyzer after the grinding operation. In all of the materials, on-line data showed close agreement with the off-line data regardless of the starting materials. It was found that the developed on-line measurement unit could measure the median diameter accurately from fine to large.

The median diameter decreased with an increase in rotating speed of the rotor. This tendency between the median diameter and the rotating speed was almost the same as the calculated results in chapter III, section 5.7. It was because that the particles in the grinding chamber impacted against a wall at a high speed. This consideration was validated from the calculated results in chapter II-1, section 5.5. The median diameter decreased drastically with an increase in the rotating speed at the range of relatively low rotating speed, and slightly decreased at the range of relatively high rotating speed. The relationship between the median diameter and the rotating speed varied according to the starting materials (see Fig. 4.1.2). It was found that the dynamic characteristics of the dry impact pulverizer varied depending on the starting materials. This means that a case-by-case optimization is required if a conventional control method such as PID control is used. Thus, a fuzzy control, which requires no tuning parameters unlike the conventional control methods, is adapted in this study.

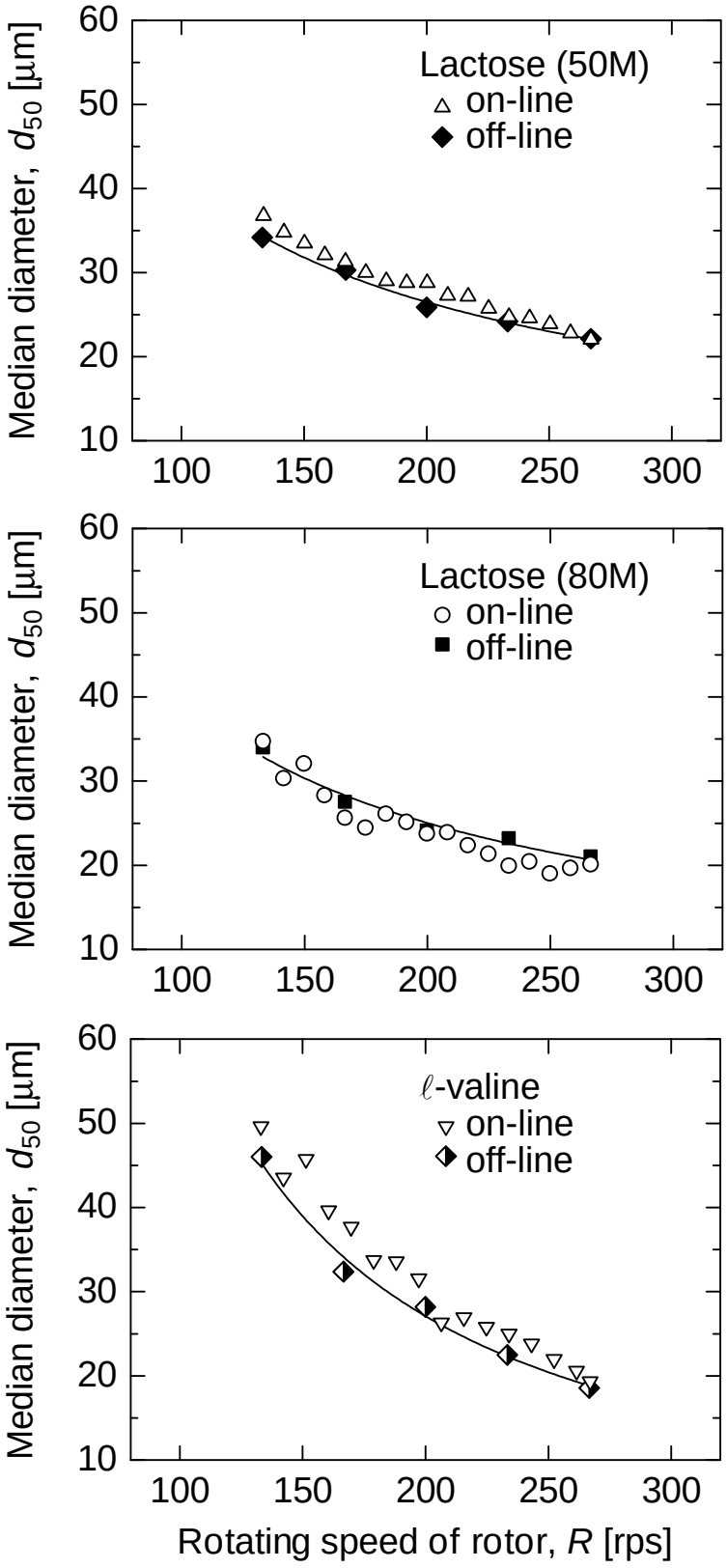

Fig. 4.1.2. Median diameter of ground products measured by on-line and off-line measurements under various starting materials.

3. Design of fuzzy controller

Fig. 4.1.3 shows a block diagram of a developed feedback control system for controlling median diameter of the ground products. It is necessary for the control to consider not only the deviation, Δd_{50} between a desired $d_{50\mathrm{d}}$ and measured d_{50} median diameter of the ground products but also the current rotating speed of the rotor, R. This is because a change rate of the median diameter depends on the rotating speed (see Fig. 4.1.2). Therefore, the control system was decided to be composed of a two-inputs and one-output controller. The two-inputs were a normalized deviation, $\overline{\Delta d_{50}}$ and normalized rotating speed of the rotor, $\overline{R}$. They were defined as follows:

$$\overline{\Delta d_{50}} = \frac{d_{50} - d_{50\mathrm{d}}}{d_{50\mathrm{d}}} \quad \text{normalized to} \quad -1 \rightarrow +1 \tag{4.1.1}$$

$$\overline{R} = \frac{R}{R_{\max}} \quad \text{normalized to} \quad 0 \rightarrow +1 \tag{4.1.2}$$

where R is a current rotating speed of the rotor and $R_{\max}$ is a maximum rotating speed of the rotor ($R_{\max}$ = 267 rps). If the absolute value of the $\overline{\Delta d_{50}}$ was larger than 1, it was identified as 1. The one-output was the normalized variation of the rotating speed $\overline{\Delta R}$, which was normalized by 50 rps. The $\overline{\Delta R}$ was derived from a fuzzy reasoning. The fuzzy reasoning is described below.

Fig. 4.1.4 indicates membership functions used in the fuzzy reasoning. Membership functions are generally used to convert the process variables to ambiguous expressions. Triangular representation was used for the input variables of $\overline{\Delta d_{50}}$ and $\overline{\Delta R}$. In this study, the following seven fuzzy variables were used: NL (Negative Large), NM (Negative Medium), NS (Negative Small), ZR (Zero), PS (Positive Small), PM (Positive Medium), PL (Positive Large). The shape of member ship function of $\overline{\Delta d_{50}}$ was decided to define control range as ± 5% of the desired set-point value. In the control method using the membership function, the control range and control speed of the median diameter can be modified easily by changing the membership function and the normalization.

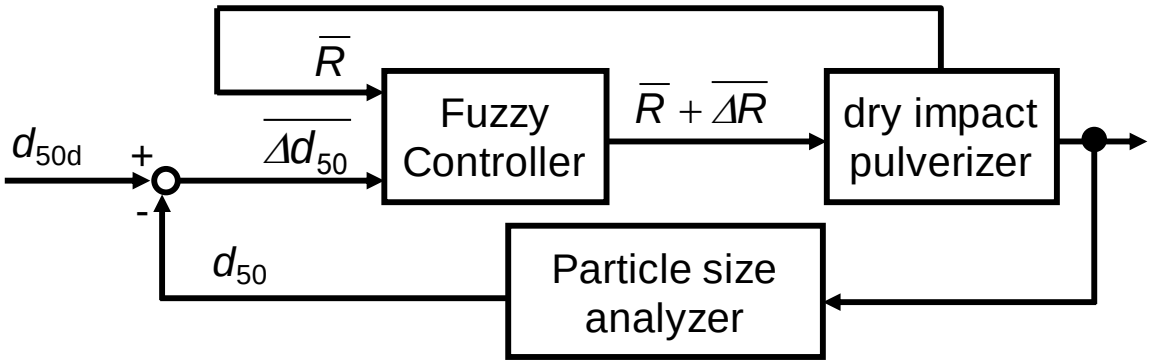

Fig. 4.1.3 Block diagram of feedback control system.

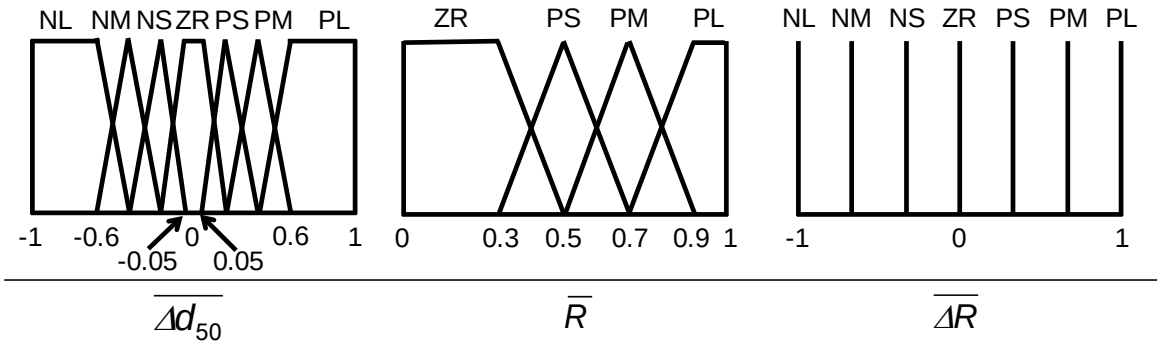

Fig. 4.1.4 Membership function for fuzzy control.

Table 4.1.1 shows production rules for controlling the median diameter. 25 rules were used for the fuzzy reasoning. Those rules were designed by the experiences, experimental results (see Fig. 4.1.2), and numerical results. For example, at the low rotating speed the rotating speed should be changed mildly when the deviation between the desired and current median diameter was large. Another example, at the high rotating speed the rotating speed should be change largely even if the deviation between the desired and current median diameter was small. The rotating speed maintained the same value when the $\overline{\Delta d_{50}}$ was zero in the membership function. Controlled variable was calculated using the membership function and production rules. The fuzzy reasoning was conducted by a min-max method [1]. The results of the fuzzy reasoning was defuzzified and then the $\overline{\Delta R}$ was obtained. The developed system has a delay time such as changing time of the rotating speed of the rotor and transporting time of the ground particles from the grinding chamber to the measurement point through the sampling unit. The system also takes at least 10 s to measure particle size distribution in the laser diffraction particle size analyzer. Therefore, in order to control the system stably, the interval of the particle size measurement and output of the control variable was set as 14 s.

Table 4.1.1 Production rules for fuzzy control

No.	$\overline{\Delta d_{50}}$	$\overline{R}$	$\overline{\Delta R}$
1	ZR		ZR
2	PS	ZR	NS
3		PS	NS
4		PM	NS
5		PL	NM
6	PM	ZR	NS
7		PS	NM
8		PM	NM
9		PL	NL
10	PL	ZR	NM
11		PS	NM
12		PM	NL
13		PL	NL
14	NS	ZR	PS
15		PS	PS
16		PM	PS
17		PL	PM
18	NM	ZR	PS
19		PS	PM
20		PM	PM
21		PL	PL
22	NL	ZR	PM
23		PS	PM
24		PM	PL
25		PL	PL

ZR ; Zero
NS ; Negative Small PS ; Positive Small
NM ; Negative Medium PM ; Positive Medium
NL ; Negative Large PL ; Positive Large

4. Results and discussion

4.1. Particle size control of ground products

Fig. 4.1.5 shows temporal change in median diameter of ground lactose under the fuzzy control. The figure also shows temporal changes in controlled rotating speed of the rotor. The different desired set-point values (d_{50d} = 23, 25, 27, 30, 33, 42 μm) were used. For all cases, at the beginning of the control (t = 0 s), the median diameter was changed and then maintained at the desired set-point value. The rotating speed was automatically changed considering the current rotating speed and the deviation between desired and current median diameter. Afterward, the median diameter was maintained within ±5% of each desired set-point value. Regardless of the desired set-point value, the system could control the median diameter within a short time.

Fig. 4.1.6 shows temporal change in median diameter of ground ℓ-valine. The different desired set-point values (d_{50d} = 32, 35, 40 μm) were used. Even if the ℓ-valine was used, the developed system could control the median diameter of ground products very well without changing either the IF-THEN rules or the membership functions.

Fig. 4.1.7 illustrates accuracy of the control. In this figure, the on-line measurement indicates the average of controlled median diameter measured by on-line unit. The off-line measurement shows the median diameter of ground products in the collection pot after the controlled grinding operation. The results indicated that the median diameters obtained from both the on-line and off-line measurements were regulated within ±10% of the desired set-point value. Therefore, it was found that the developed system and technique could control the median diameter of ground products accurately.

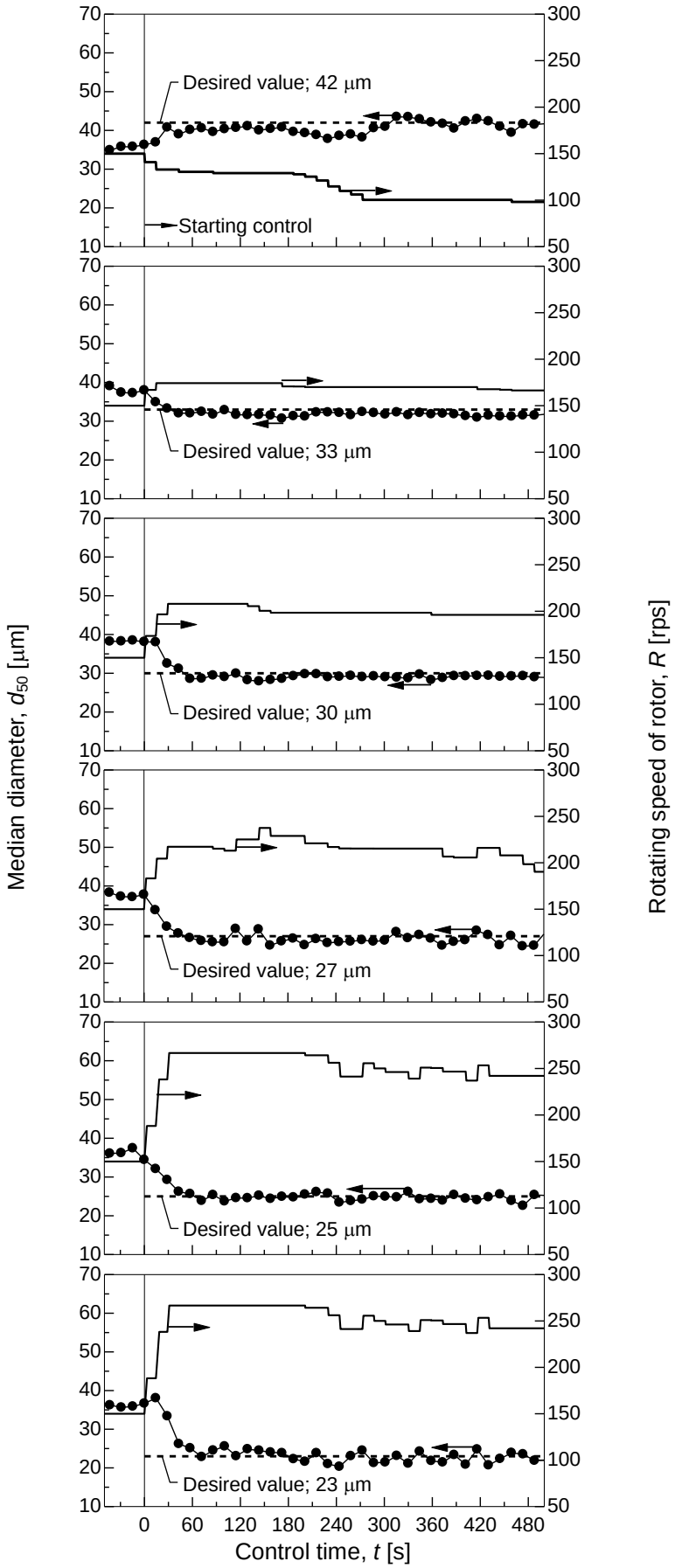

Fig. 4.1.5. Control results of median diamter under various desired values (Powder sample; Lactose).

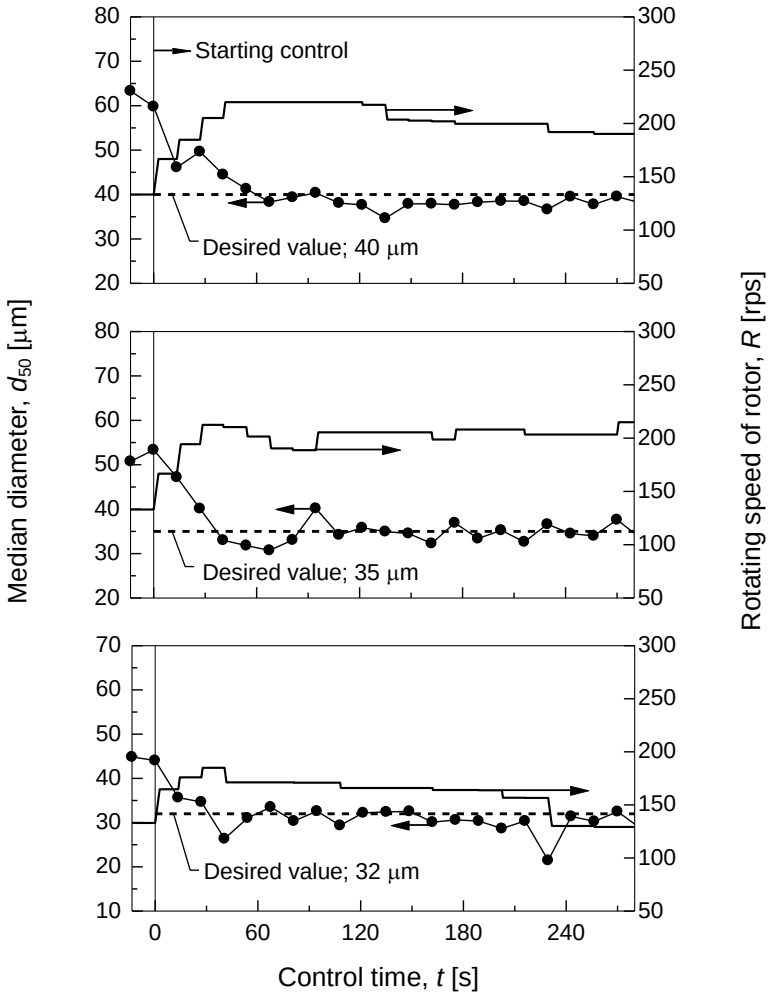

Fig. 4.1.6. Control results of median diamter under various desired values (Powder sample; ℓ-valine).

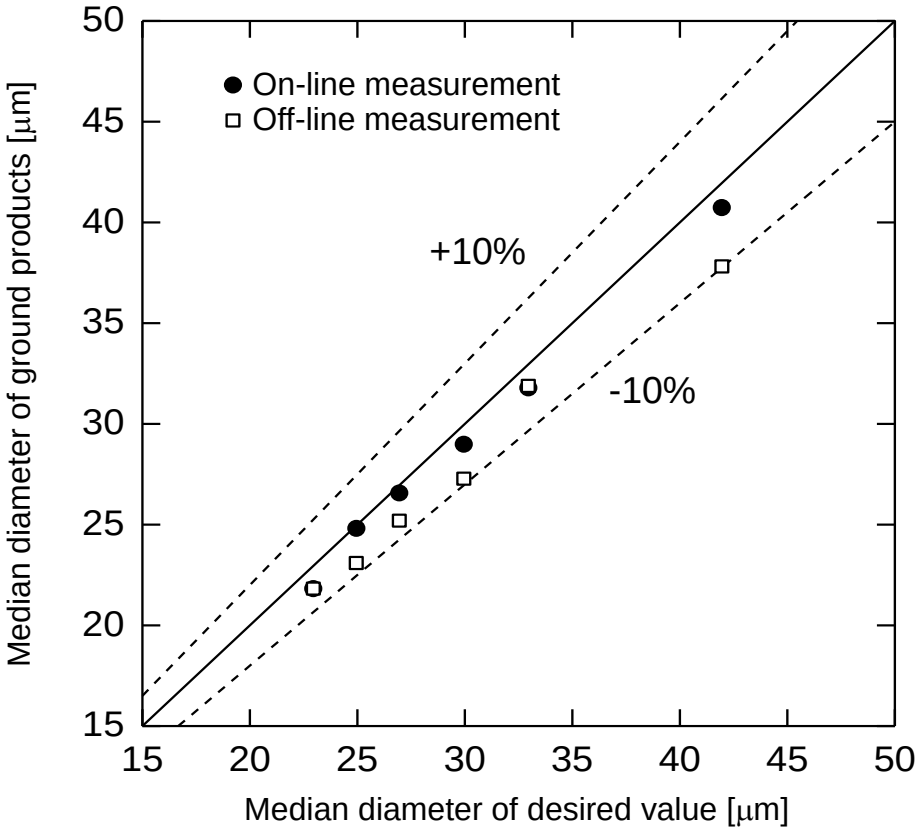

Fig. 4.1.7. Control accuracy under various desired values (Powder sample; Lactose).

4.2. Particle size control under external disturbance

Fig. 4.1.8 indicates control results with an external disturbance. As the external disturbance, the feed rate of lactose powder was changed from 28 to 80 g/min (a) and from 28 to 60 g/min (b) under the same desired set-point value (30 μm). When the feed rate increased at $t = 0$ s, the median diameter was increased at $t = 14$ s. This was because the number of collision per mass of powder decreased due to the increase in the mass of powders in grinding chamber. When the larger amount of the feed rate changed at $t = 0$ s, the larger median diameter was obtained at $t = 14$ s. This was because the particles received less chance to be ground when the feed rate was large. The developed system automatically detected the deviation from ±5% of the desired set-point value at $t = 14$ s. The system then increased the rotating speed at that time. By the control of the rotating speed, the median diameter was decreased and maintained at the desired set-point value appropriately. Those experimental results imply that the developed system can stably control the median diameter even under the external disturbance.

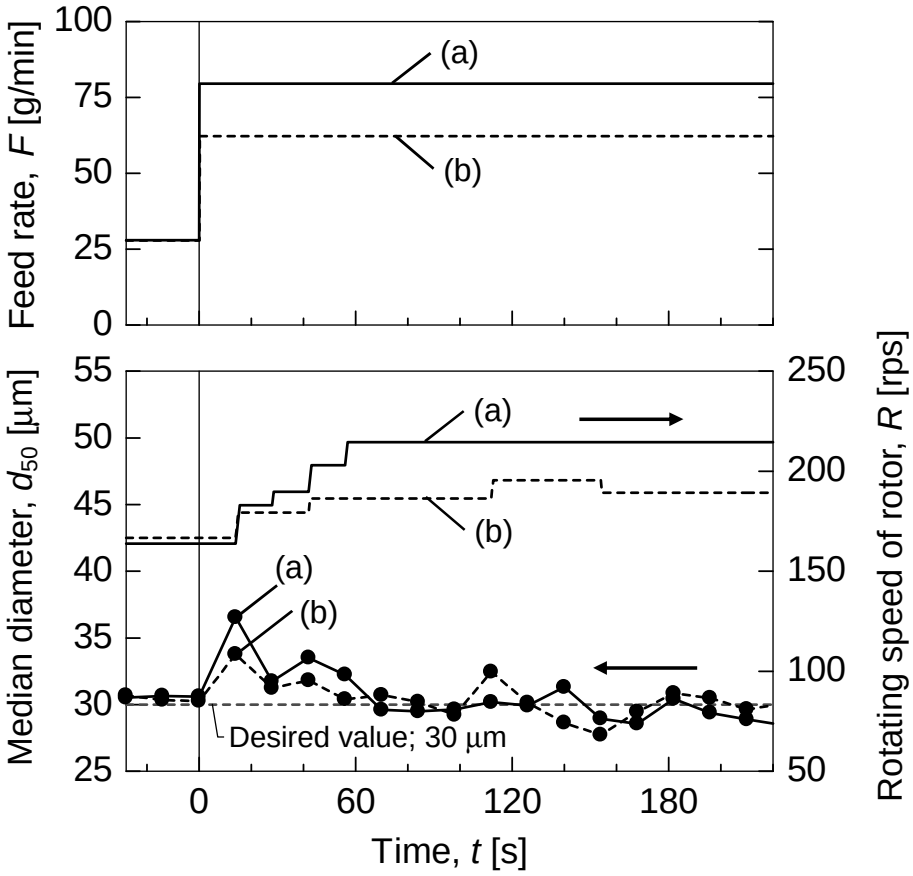

Fig. 4.1.8. Control results of median diameter under change in feed rate;
(a) F = 28 → 80 g/min, (b) F = 28 → 60 g/min
(Powder sample; Lactose).

5. Conclusion

A novel practical system for controlling the particle size of ground products in a dry impact pulverizer was developed. The system accurately measured the particle size of ground products with an on-line laser diffraction particle size analyzer. Also, fuzzy controller consisting of membership functions and linguistic IF-THEN rules was developed with consideration of the complex dynamics and characteristics of the dry impact pulverizer. The developed system could accurately control the median diameter within ±10% of the desired set-point values even if the different starting materials were used. In addition, the system automatically detected change in the median diameter when it is subjected to the external disturbance, such as the feed rate changes. Therefore, it was found that the developed feedback control system with the fuzzy logic was a useful method for controlling the median diameter of ground products in the dry impact pulverizer.

Nomenclature

d_{50}	: Median diameter	[m]
$d_{50\mathrm{d}}$	: Desired median diameter	[m]
Δd_{50}	: Deviation between desired and current median diameter	[m]
$\overline{\Delta d_{50}}$	: Normalized deviation between desired and current median diameter	[–]
F	: Feed rate of starting materials	[kg/s]
R	: Rotating speed of rotor	[rps]
$\overline{R}$	: Normalized rotating speed of rotor	[–]
$R_{\max}$	: Maximum rotating speed of rotor	[rps]
ΔR	: Variation between desired and current rotating speed of rotor	[rps]
$\overline{\Delta R}$	: Normalized variation between desired and current rotating speed of rotor	[–]
t	: Control time	[s]

References

1 Mamdani EH, Assilian S. An experiment in linguistic synthesis with a fuzzy logic controller. Int. J. Man Mach. Stud. 1975;7:1-13.

2 Pomerleau A, Hodouin D, Desbiens A, Gagnon E. A survey of grinding circuit control methods: from decentralized PID controllers to multi-variable predictive controllers. Powder Tehcnol. 2000;108:103-115.

3 Watano S, Numa T, Koizumu I, Osako Y. Feedback control in high shear granulation of pharmaceutical powders. Eur. J. Pharm. Biopharm. 2001;52:337-345.

4 Watano S, Numa T, Miyanami K, Osako Y. A Fuzzy control system of high shear granulation using image processing. Powder Technol. 2001;115:124-130.

5 Zadeh LA. Fuzzy Sets. Inf. Control. 1965;8:338-353.

Chapter V

Overall Conclusions

This thesis has been devoted to a numerical modeling of particle breakage and a control of particle size in a dry impact pulverizer. The main objectives of this thesis were as follow:

(1) understanding and analyzing fluid flow and particle motion in the dry impact pulverizer by using numerical simulation
(2) development of a novel method which can simultaneously simulate single particle breakage and overall grinding phenomena in the dry impact pulverizer
(3) elucidation of fundamental particle breakage mechanism and overall grinding mechanism in the dry impact pulverizer
(4) development of a practical system for automatic control of ground product size in the dry impact pulverizer

The main results and obtained findings are summarized in below:

In Chapter II, fluid and particle motion in a dry impact pulverizer was numerically analyzed.

The fluid and particle motions in the dry impact pulverizer were calculated by a discrete phase model and computational fluid dynamics coupling model (DPM-CFD coupling model). Validity of the simulation model was confirmed by measuring fluid pressure in the grinding chamber and actual particle motion recorded by means of a high-speed video camera. It was found that particles received kinematic energy from the fluid flow which was accelerated by the rotating rotor in the grinding chamber. The particles then mainly impacted against a stator wall of the grinding chamber. The velocity and frequency of the impacted particles decreased with a decrease in its particle size. The velocity and frequency were increase with an increase in the rotating speed of the rotor.

The impact energy was calculated from the velocity and frequency of impacted particles against entire wall of the grinding chamber. The impact energy well explained experimental results of median diameter of the ground products under various geometries of the rotor. The number of hammer installed at the rotor and clearance

between tip of the hammer and stator wall of the grinding chamber was changed. The excellent correlation between the calculated results of the impact energy and the experimental results of the median diameter has been obtained. The effect of the geometries and the operating conditions on the grinding performance can be predicted in advance from the calculated results of the numerical simulation.

In Chapter III, a novel simulation method of particle motion and its breakage in a dry impact pulverizer was developed.

In this proposed method, in order to propose a particle breakage model, the single particle breakage was divided into three processes, i.e., particle strength, impact stress acting on the particle, and fragment size distribution after the particle breakage. The particle strength described by Griffith's theory with an assumption that length of cracks in a particle obeyed a log-normal distribution was actually measured by a uniaxial compression test. The particle strength was calculated from the Griffith's theory as a function of the particle size. The size distribution of fragments measured by an impact breakage test was well expressed as a power-low function. The size distribution of the fragments was calculated from the power-low function as a function of particle size and particle impact velocity. By the proposed simulation method, the particle breakage phenomena in the dry impact pulverizer such as a decrease in its size and increase in number after the particle breakage were successfully calculated. Validity of the proposed simulation model was confirmed by the comparison between the experimental and calculated results. The calculated results of particle size distribution of the final ground product showed good agreement with the experimental result. The calculated results exhibited clearly where and how the particles were broken in the grinding chamber. By this method, particle size distribution of the final ground products in the dry impact pulverizer can be predicted.

In Chapter IV, a novel feedback control system based on a fuzzy logic for controlling particle size of the final ground products in a dry impact pulverizer was developed.

Particle size distribution of the final ground products was measured by a developed on-line measurement system. The particle size continuously measured by the on-line

system was in good agreement with the one measured manually after the grinding operation. The dynamic characteristics of the dry impact pulverizer were clarified from the correlation between the median diameter and rotating speed of the rotor. Based on the fuzzy logic, two-input and one-output controller was established for controlling median diameter of the final ground products. The linguistic algorism employing IF-THEN rules were developed with considering the dynamic characteristic of the dry impact pulverizer. The developed system could accurately control the median diameter within ±10% of the desired set-point values even if the different starting materials were used. In addition, the system automatically detected change in the median diameter, when it is subjected to the external disturbance, such as feed rate change. The system can be very useful for many industries, in which most of the operations have still relied upon the expert experience.

The author hopes that this thesis can contribute to the better understanding of the grinding mechanism, optimal designing, and the innovative progress of grinding process.

List of papers related to this thesis

No.	Article Title	Authors	Journal	Related to this thesis
1	Theoretical Analysis of Grinding Mechanism and Feedback Control of Grinding Process in Impact Pulveriser	H. Takeuchi, T. Iwasaki, N. Asai, S. Watano.	Proc. of 6th World Congress on Particle Technology, Paper# 597, Total 4 pages (Nürnberg, Germany, 2010).	Chapter 2
2	Numerical Modeling of Fluid and Particle Behaviors in Impact Pulverizer	H. Takeuchi, H. Nakamura, T. Iwasaki, S. Watano.	Powder Technol., Vol. 217, pp. 148-156 (2012).	Chapter 2
3	Computer Simulation of Particle Behavior and Equipment Design in Impact Pulverizer	H. Takeuchi, H. Nakamura, S. Watano.	J. Soc. Powder Technol, Japan (In Japanese) Vol. 49, No. 3, pp. 191-200 (2012).	Chapter 2
4	Direct Numerical Simulation of Particle Breakage in Dry Grinding Process	H. Takeuchi, H. Nakamura, S. Watano.	Proc. of 5th Asian Particle Technology Symposium, Paper# 169, pp. 146-147 (Singapore, 2012).	Chapter 3
5	Numerical Simulation of Particle Breakage in Dry Impact Pulverizer	H. Takeuchi, H. Nakamura, S. Watano.	AIChE J., in press.	Chapter 3
6	Feedback Control of Particle Size by a Novel Fuzzy Control System in Dry Grinding Process	H. Takeuchi, T. Iwasaki, S. Watano , N. Asai, Y. Togawa, T. Yamaguch.	Proc. of 4th Asian Particle Technology Symposium, Paper# 72, Total 6 pages (Delhi, India, 2009).	Chapter 4
7	Development of a Novel Particle Size Control System for Hammer Milling	H. Takeuchi, H. Nakamura, T. Iwasaki, N. Asai, S. Watano.	Adv. Powder Technol., Vol. 21, pp. 681-685 (2010).	Chapter 4